

**NOVEL MATHEMATICAL METHODS FOR ANALYSIS OF BRAIN
WHITE MATTER FIBERS USING DIFFUSION MRI**

by
Devran Uğurlu

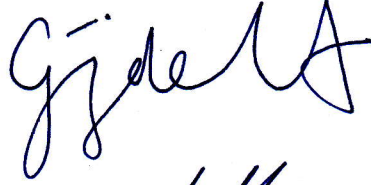
**Submitted to the Graduate School of Engineering and Natural Sciences
in partial fulfillment of the requirements for the degree of
Doctor of Philosophy
in Computer Science and Engineering**

**Sabancı University
Spring 2017-2018**

NOVEL MATHEMATICAL METHODS FOR ANALYSIS OF BRAIN
WHITE MATTER FIBERS USING DIFFUSION MRI

APPROVED BY:

Prof. Dr. Gözde ÜNAL
(Thesis Supervisor)



Assoc. Prof. Dr. Hüsnü YENİGÜN



Prof. Dr. Canan ATILGAN



Prof. Dr. Çiğdem Eroğlu ERDEM



Assoc. Prof. Dr. Burak ACAR



DATE OF APPROVAL: 16/07/2018

©Devran Uğurlu 2018

All Rights Reserved

to my family

Acknowledgments

First and foremost I would like to express my gratitude to my advisor Prof. Dr. Gozde Unal. She was a good mentor who gave very valuable advice and guidance and knew how to motivate me to aim for greater accomplishments.

I would like to thank Zeynep Fırat and Prof. Dr. Uğur Türe for their invaluable clinical support. They provided pathological diffusion MRI data, gave me lectures on neuroanatomy and fiber tract extraction, and greatly assisted in the clinical motivation and discussion of this thesis.

I am grateful to my committee members Assoc. Prof. Dr. Hüsnü Yenigün, Prof. Dr. Canan Atılgan, Prof. Dr. Çiğdem Eroğlu Erdem and Assoc. Prof. Dr. Burak Acar for taking the time to read and comment on my thesis.

I thank all my friends and colleagues, particularly, Süheyla Çetin Karayumak, Rıza Alp Güler and Andaç Hamamcı for their friendship and assistance.

I also would like to thank TÜBİTAK for providing the necessary financial support for my graduate education through the research project No. 112E320 (Beyinsapı Beyaz Cevher Yolaklarının Ameliyat Öncesi ve Sonrası Değişimlerinin Difüzyon Tensör Görüntüleme ile Analizinde Yeni Matematiksel Bilgisayar Yöntemleri).

NOVEL MATHEMATICAL METHODS IN THE ANALYSIS OF WHITE MATTER
FIBERS IN THE BRAIN USING DIFFUSION MRI IMAGES

Devran Uğurlu

CS, PhD. Thesis, 2018

Thesis Supervisor: Gözde ÜNAL

Keywords: diffusion MRI (DMRI), white matter, fiber clustering, fiber classification, neighborhood resolved fiber orientation distribution(NRFOD),

Abstract

White matter fibers connect and transfer information among various gray matter regions of the brain. Diffusion Magnetic Resonance Imaging (DMRI) allows in-vivo estimation of fiber orientations. From the estimated orientations, a 3D curve representation of the trajectory of fibers can be reconstructed in a process known as tractography. Automatic classification of these “tracts” into classes of anatomically known fiber bundles is a very important problem in neuroimage computing.

In this thesis, three automatic fiber classification methods are proposed. The first two are based on combining neuroanatomical priors with density-based clustering. The first method includes brainstem heuristics but the second is more general and can be applied to any fiber pathway in the brain. Further, the second method introduces a novel fiber representation, Neighborhood Resolved Fiber Orientation Distribution(NRFOD), that represents a tract as a set of histograms that encode the distribution of fiber orientations in its neighborhood. The third method utilizes the NRFOD representation to directly map a tract to a probability estimate for each bundle class in a supervised classification framework. A practical training and validation set creation methodology is proposed.

Additionally, the thesis includes statistical significance tests to investigate whether the

structural change between pre-operative and post-operative fiber bundles after a tumor resection operation are related to the change in patient's cognitive performance scores. To this end, a fiber bundle to fiber bundle registration method and various quantitative measures of the structural change are proposed. We present results over DMRI data with clinical evaluations of 30 patients with brainstem tumors.

BEYİNDEKİ BEYAZ CEVHER LİFLERİNİN DİFÜZYON MRG GÖRÜNTÜLERİ KULLANILARAK ANALİZİNDE YENİ MATEMATİKSEL YÖNTEMLER

Devran Uğurlu

CS, Doktora Tezi, 2018

Tez Danışmanı: Gözde ÜNAL

Anahtar Kelimeler: difüzyon MRG (DMRG), beyaz cevher lifleri, lif kümeleme, lif sınıflandırma, komşu lif yönleri dağılımı(KFYD)

Özet

Beyindeki beyaz cevher lifleri, çeşitli gri cevher bölgelerinin birbiriyle iletişimini sağlar. Difüzyon Manyetik Rezonans Görüntüleme (DMRG), hayatta olan deneklerin beyaz cevher liflerinin oryantasyonlarının kestirilmesini mümkün kılar. Kestirilen oryantasyonlar kullanılarak, liflerin yörüngelerinin 3B eğri temsilleri oluşturulabilir. Bu işlem trakrografi olarak bilinmektedir. Yolak olarak da adlandırılan bu 3B eğri temsillerinin bilinen anatomik lif kümelerine otomatik olarak sınıflandırılması, sinirgörüntü işlemede çok önemli bir problemdir.

Bu tezde, üç yeni otomatik yolak sınıflandırma yöntemi önerilmiştir. İlk iki metot, sinir anatomik önbilginin, yoğunluk tabanlı danışmansız kümeleme metoduyla birleştirilmesine dayanmaktadır. İlk metot, beyinsapına özel buluşsal yöntemler içermekle beraber, ikinci metot daha genel bir metot olup, beyindeki her lif kümesi için uygulanabilir. Ayrıca, ikinci metotta yeni bir lif temsili önerilmiştir. Komşu lif yönleri dağılımı (KLYD) adını verdiğimiz bu temsil, her yolağı, komşuluğundaki lif oryantasyon dağılımını kodlayan histogramlarla temsil etmektedir. Üçüncü metot, KLYD temsili kullanılarak, danışmanlı öğrenme yaklaşımı çerçevesinde, her yolağı, doğrudan, ilgilenilen lif küme sınıflarına ait olma olasılık kestirimlerine haritalar. Pratik bir eğitim ve doğrulama kümesi oluşturma

metodolojisi de önerilmiştir.

Bunlara ek olarak, tümör çıkarılma ameliyatı öncesi ve sonrası lif yapıları arasındaki deęişim ile hastanın klinik bilişsel bulguları arasında istatistiksel olarak anlamlı bir ilişki olup olmadığı araştırılmıştır. Bu bağlamda, bir yolak kümesinden yolak kümesine çakıştırma metodu ve lifler arasındaki deęişimi sayısallaştırmaya yönelik çeşitli ölçütler önerilmiştir. Beyinsapında tümör bulunan 30 hastanın DMRG görüntüleri ve klinik deęerlendirme puanları üzerinde elde edilen sonuçlar sunulmuştur.

Table of Contents

Acknowledgments	vi
Abstract	vii
Özet	ix
1 Introduction	1
1.1 Motivation of the Thesis	1
1.2 Contributions of the Thesis	2
1.3 List of Abbreviations	5
2 Background	6
2.1 Neuroanatomy	6
2.1.1 Anatomical Directions and Planes	7
2.1.2 Major Subdivisions of the Central Nervous System	9
2.1.3 Major Fiber Tracts in the Brainstem	13
2.2 Magnetic Resonance Imaging (MRI)	14
2.2.1 Relaxation	18
2.2.2 Signal Acquisition with Basic Pulse Sequences	20
2.2.3 Spatial Encoding and k-space	24
2.2.4 Diffusion Magnetic Resonance Imaging (DMRI)	28
2.3 Image Registration	36
2.4 Tractography	37
2.5 Literature Review of Fiber Clustering and Classification	39
3 Automatic Labeling of Brainstem Fiber Pathways Using Anatomically-Constrained Density-Based Clustering	44
3.1 Materials and Methods	44
3.1.1 Dataset	44
3.1.2 Pre-processing and tractography	45
3.1.3 Clustering algorithm overview	46
3.1.4 Fiber Bundle Mask Creation	49
3.1.5 Dissimilarity measure between fibers	49
3.1.6 Geometry-based clustering algorithm	51
3.1.7 Cluster Selection from OPTICS output	55

3.1.8	Extraction of MCP	55
3.1.9	Extraction of SCP and ICP	56
3.1.10	Extraction of CST and ML	57
3.2	Results	60
3.2.1	Implementation Details	60
3.2.2	Comparison of the Proposed Method to Manual ROI Method . . .	61
3.3	Discussion and Conclusion	65
4	Neighborhood Resolved Fiber Orientation Distributions (NRFOD) in Automatic Labeling of White Matter Fiber Pathways	68
4.1	Materials and Methods	68
4.1.1	Dataset	69
4.1.2	Reconstruction of Orientation Distribution Functions	69
4.1.3	Manual ROI Selection on Standard Space	70
4.1.4	Tractography	71
4.1.5	Neighborhood Resolved Fiber Orientation Distribution (NRFOD) of a Fiber and the Fiber-to-fiber Distance Measure (NRFODD) . .	72
4.1.6	Density-based Clustering with OPTICS	76
4.1.7	Reference Bundle Creation and Cluster Selection from OPTICS Output	77
4.2	Results	78
4.2.1	Selection of NRFOD Parameters	78
4.2.2	Sensitivity of NRFODD to Registration Errors Compared to MDF .	80
4.2.3	Comparison of the Proposed Method to the Manual ROI Method .	84
4.2.4	Comparison of the Proposed Method to Other Automatic Methods	86
4.2.5	Sensitivity of the Proposed Method to the Reference Bundles	90
4.3	Discussion	91
4.3.1	Limitations	94
4.4	Conclusion	95
4.A	The determination of the probability of following a direction in tractography	96
5	Supervised Classification of White Matter Fibers Based on Neighborhood Fiber Orientation Distributions Using an Ensemble of Neural Networks	98
5.1	Materials and Methods	98
5.1.1	Dataset, Reconstruction of ODFs and Tractography	98
5.1.2	Manual ROI Selection on Standard Space to Constrain Input Tract Sets	99
5.1.3	Construction of the Training and Validation Sets	100
5.1.4	Network Architectures and Training	102
5.1.5	Testing	103
5.2	Results and Discussion	103
5.3	Conclusion	108

6	Analysis of Structural Changes on Major White Matter Fiber Pathways Passing Through The Brainstem Between Pre-Operative and Post-Operative Diffusion MRI Images For Patients With Brainstem Lesions	109
6.1	Measures that are not Based on a Deformation Field	110
6.1.1	Translation of Center of Mass (NDM1)	110
6.1.2	Change in Principal Direction (NDM2)	110
6.1.3	Local Mean Orientation Maps (NDM4, NDM5)	111
6.1.4	Measures Based on Symmetry Axis (NDM6, NDM7)	112
6.1.5	Dice Score (NDM8)	113
6.1.6	Screened Poisson Hyperfields (NDM10)	114
6.2	Fiber Bundle Registration	115
6.2.1	Formulation of the Deformable Registration Problem	115
6.2.2	Solution of the Deformation Model	119
6.3	Measures based on the Deformation Field	119
6.4	Results and Discussion	121
6.4.1	Clinical Dataset	121
6.4.2	The Values of Measures	121
6.4.3	Statistical Tests	124
6.4.4	Discussion	126
7	Conclusion and Future Directions	129
	Bibliography	132

List of Figures

2.1	<i>Examples of some nervous system cells (not to scale). Figure reproduced from [1] with permission.</i>	7
2.2	<i>The main planes for viewing the brain. Figure reproduced from [1] with permission.</i>	9
2.3	<i>A sagittal view of the major subdivisions of the human brain. The medulla, pons and midbrain together are called the brainstem. Figure reproduced from [1] with permission.</i>	10
2.4	<i>Functions of the 12 cranial nerves and their entry and exit locations. Figure reproduced from [1] with permission.</i>	12
2.5	<i>An illustration of the cerebral cortex. Figure reproduced from [1] with permission.</i>	13
2.6	<i>An illustration of the magnetic moment ($\vec{\mu}$) of a proton precessing around the constant magnetic field \vec{B}_0.</i>	15
2.7	<i>An illustration of the net magnetization vector being flipped from the z-direction into the transverse plane using an RF pulse. The primed reference frame is a rotating frame that rotates with frequency ω_0 around the z-axis.</i>	18
2.8	<i>Illustration of T2 relaxation. Individual magnetic moments are illustrated in the up row and the net magnetization is illustrated in the bottom row. Left is the equilibrium state, middle is the state right after a 90° pulse and right shows how the magnetization decays due to individual moments having different phase on their precession around the z-axis. Figure reproduced from [2] with permission.</i>	20

2.9	(a) The FID signal in laboratory frame. (b) The FID signal in rotating frame. (c) The demodulated FID signal when the demodulation is not exactly at the Larmor frequency. (d) The total demodulated FID signal from several ensembles each with slightly different Larmor frequencies. Figure reproduced from [2] with permission.	21
2.10	The sequence diagram and corresponding MRI signal in a spin-echo experiment. Figure reproduced from [2] with permission.	22
2.11	Illustration of the dephasing and rephasing of spins on the rotating frame in a spin-echo experiment. Figure reproduced from [2] with permission. . .	23
2.12	The sequence diagram for an inversion recovery experiment. ADC stands for analog-to-digital converter and converts the analog MRI signal to digital. Figure reproduced from [2] with permission.	24
2.13	Illustration of a 1D MRI experiment where a hypothetical 1D “cylinder” with random spin distribution is imaged. (a) The thermal equilibrium condition. With no gradient or rf pulse, there is no signal. (b) A 90° RF pulse is applied but no gradient. The signal gradually decays due to relaxation. (c) After a 90° RF pulse, a gradient is applied. Since the gradient will also dephase the spin in addition to relaxation, the signal decays more rapidly. Note that only positive k values can be sampled here. (d) A gradient echo sequence. First, a negative gradient is applied and after some time $(t_2 - t_1)$, the gradient is reversed. As a result, the dephasing due to the gradient will cancel out after $(t_2 - t_1)$ time and we get an “echo”. Note that if the signal is sampled during time t_3 to t_4 , both negative and positive values of k are sampled. Figure reproduced from [2] with permission.	27

2.14	<i>Illustration of how water diffusion can lead to signal loss after a dephasing and a subsequent rephasing gradient. Each circle should be considered a spin-isochromat, not individual spins and the vectors show the magnetic moment direction on the rotating frame. Note that only diffusion along the gradient axis will lead to signal loss (yellow boxes). Diffusion along the y-axis does not lead to phase incoherence (green box). Figure reproduced from [3] with permission.</i>	29
2.15	<i>Illustration on a hypothetical example of why high b-values are required to detect multiple fiber populations. (A) and (B) show two different fiber populations by themselves and the signal attenuation in 3 different gradient directions. (C) shows the situation when both of these fibers are present. The signal attenuation is now the sum of the attenuations caused by each fiber and as it is seen, it is not possible to distinguish the separate fiber populations from the signal for low b-values. Figure reproduced from [3] with permission.</i>	36
2.16	<i>Visualization of 10000 fiber tracts extracted by seeding the brainstem. Tracts are colored according to local orientation where superior-inferior direction is blue, left-right is red and anterior-posterior is green. Left: Result of a deterministic method. Right: Result of a probabilistic method.</i>	39
3.1	<i>Flowchart overview of the proposed brainstem fiber clustering framework. .</i>	48
3.2	<i>(a,b,c) An illustration of the three steps involved in matching points between two fibers in the definition of the fiber dissimilarity measure. (d) Representation of the same two fibers as sets of c vectors each (c = 6 here). (e,f) A toy example illustrating the advantage of the orientation term. Both tract pairs here would give small dissimilarity values with the mean closest point distance and the end point distance. With the addition of the orientation term, similarity of the fibers in (e) is higher than that of the fibers in (f). This is in agreement with human perception of fiber dissimilarity.</i>	51

3.3	(a)-Left: Input fibers colored according to local diffusion direction. (a)-Right: OPTICS output: ordered reachability distances (y) versus fiber indices (x). (b)-Left: Fibers colored according to clustering done with horizontal line cut method with $y = 10$. (b)-Right: OPTICS output with colored areas corresponding to clusters in (b), indicated with the same color. (c)-Left: Fibers colored according to clustering done with horizontal line cut method with $y = 2$. (c)-Right: OPTICS output with colored areas corresponding to clusters in (c), indicated with the same color.	54
3.4	(a): MCP obtained with the proposed method. (b): MCP obtained with the mROI method. Green: Seed region. Red: ROI. It is seen that when the MCP is fragmented because of signal loss on D-MRI data, the proposed method gives better results than an mROI approach (using typical ROIs shown) for extracting MCP.	56
3.5	Illustration of steps involved in extraction of the SCP and the ICP.	57
3.6	(a): Five points (p_1, \dots, p_5) manually chosen on an axial slice at the pons level on the standard space that define ROIs for CST and ML. Background image is JHU-ICBM-DTI-81 atlas colored according to labels. Red: MCP, Green: transverse pontine fibers (considered part of MCP) and ML and CST are annotated on the image (R: right, L: left). Other colors (SCP and ICP) are not relevant for CST, ML extraction. (b): An axial slice at the pons level from an individual brain with diffusion tensors visualized as ellipsoids illustrating how the rectangle ROIs defined in (a) would ideally look like on an individual brain.	58
3.7	Illustration of steps involved in extraction of the CST and the ML.	60
3.8	Visualization of clustering results for all 20 test subjects. A: Manual ROI method for subjects 1-5; B: Proposed method for subjects 1-5; C: Manual ROI method for subjects 6-10; D: Proposed method for subjects 6-10; E: Manual ROI method for subjects 11-15; F: Proposed method for subjects 11-15; G: Manual ROI method for subjects 16-20; H: Proposed method for subjects 16-20.	62

3.9	<i>Visualization of bundles created with the manual ROI method vs. the proposed method for best and worst Kappa scores achieved among the 20 test subjects.</i>	63
4.1	<i>Illustration of the proposed method on the left CST and ML bundles.</i>	69
4.2	<i>The ROIs defined on the standard MNI space to constrain initial fiber sets that will be passed to the density-based clustering algorithm. Yellow: Axial ROI on medulla for left, right projection fibers and ICP; Pink: ROI on left sensorimotor cortex for left projection fibers; Teal: ROI on right sensorimotor cortex for right projection fibers; White: Coronal ROI on cerebellum for ICP and SCP; Green: Coronal ROI on cerebellum on the left hemisphere for MCP; Dark Green: Coronal ROI on cerebellum on the right hemisphere for MCP; Blue: Coronal ROI near thalamus for ICP and SCP. Note that the ROIs are selected very large to account for individual variability and possible registration error.</i>	71
4.3	<i>An axial slice of a GQI image at the pons level. Each resolved orientation on a pixel is represented by a line color-coded according to the resolved orientation where red is left-right, green is anterior-posterior and blue is inferior-superior orientation.</i>	73
4.4	<i>Illustration of construction of the NRFOD representation of a fiber. At each point on the fiber, the neighborhood is probed with cylinders in M directions and a histogram of resolved fiber orientations in the cylinders are computed.</i>	74
4.5	<i>(a)-Left: Input fibers colored according to local diffusion direction. (a)-Right: OPTICS output: ordered reachability distances (y) versus fiber indices (x). (b)-(c)-Left: Fibers colored according to clustering done with horizontal line cut method with $y = 10$ and $y = 2$, respectively. (b)-(c)-Right: OPTICS output with colored areas corresponding to clusters on the left, indicated with the same color.</i>	77

4.6	<i>Mean BMD values between manually extracted bundles and bundles extracted by the proposed method for various parameter settings. $K = 50, r = h/2$ for all plots. Mean is taken across all 10 training subjects and all bundles of interest.</i>	80
4.7	<i>Heat maps of the distance matrices between tracts on the original space and the transformed spaces. There are 250 tracts from each bundle of interest in the following order: CST left, CST right, ICP left, ICP right, MCP, ML left, ML right, SCP left, SCP right.</i>	82
4.8	<i>Visualization of clustering results from the set of test subjects. A: Manual ROI method for subjects 1-5; B: Proposed method for subjects 1-5; C: Manual ROI method for subjects 6-10; D: Proposed method for subjects 6-10. Tracts are colored according to assigned bundle as follows: CST Left: orange; CST Right: dark green; ML Left: teal; ML Right: pink; ICP Left: white; ICP Right: yellow; SCP Left: green; SCP Right: blue; MCP: red.</i>	85
4.9	<i>Visualization of bundles created with the manual ROI method vs. the proposed method for best and worst BMD values achieved among the test subjects. Tracts are colored according to local direction.</i>	86
4.10	<i>Visualization of clustering results for the proposed method (middle left), the naïve maximal overlap method (middle right), tract querying method (bottom left) and spectral clustering with additional cluster selection (bottom right) on one of the subjects in the test set. Fiber sets used as input to the clustering algorithms are shown at the top and are colored according to local direction. Clustered tracts are colored according to assigned bundle as follows: CST Left: orange; CST Right: dark green; ML Left: teal; ML Right: pink; ICP Left: white; ICP Right: yellow; SCP Left: green; SCP Right: blue; MCP: red.</i>	89

4.11	<i>A comparison of the proposed method (left) to a naïve maximal overlap approach (right) using the reference bundles for right CST (red) and ML (yellow) fibers (top row) and right SCP (green) and ICP (purple) fibers (bottom row) on one of the subjects in the test set. The maximal overlap approach can confuse spatially close bundles like CST and ML and can have many spurious fibers when the initial fiber set cannot be well-constrained by automatic ROIs as in the case of the SCP and ICP.</i>	90
5.1	<i>Illustration of the proposed training set creation scheme. For every subject in the training set, Step 1: manually created streamlines for each fiber tract are converted to a volumetric mask. Depicted tract masks are colored as follows: Red: MCP, Blue: CST, Green: ML, Yellow: ICP, Pink: SCP. Step 2: A collection of streamlines are constructed by tractography using automatic ROIs. In step 3 and later, the process is illustrated for one streamline. This is repeated for every streamline created in step 2.</i>	100
5.2	<i>The architecture of the classifiers in the ensemble.</i>	103
5.3	<i>Visualization of bundles of interest extracted from the 5 test subjects. A: Manual method for subjects 1-3; B: Proposed method for subjects 1-3; C: Manual method for subjects 4-5; D: Proposed method for subjects 4-5. Tracts are colored according to their bundle label as follows: CST Left: blue; CST Right: purple; ML Left: pink; ML Right: teal; ICP Left: yellow; ICP Right: green; SCP Left: brown; SCP Right: white; MCP: red.</i>	106
5.4	<i>Visualization of input streamlines and results of the proposed method on one subject in the test set. In top-bottom, left-right order: The input set of streamlines created with the automatic ROIs; invalid streamlines; MCP; left CST; right CST; left ML; left SCP; right SCP; right ML; left ICP; right ICP.</i>	107

6.1	<i>V (red),U (green) volumes depicting the binary mask of pre-op and post-op ML right bundle of a subject and an axial slice of corresponding orientation fields I_{vec} and J_{vec}. FA values are used as background intensity and the orientation field is shown as colored lines on voxels on which they are defined. On voxels where the orientation field is undefined, black lines are used.</i>	116
6.2	<i>An axial slice from the I_{sca} and J_{sca} volumes.</i>	117
6.3	<i>Illustration of the deformation model. Red: pre-op bundle mask; Green: post-op bundle mask.</i>	118
6.4	<i>All measures for the left CST of subjects. DM 1-4 are the measures based on a deformation field and NDM1-10 are the measures that do not require estimation of a deformation field.</i>	122
6.5	<i>All measures for the right CST of subjects. DM 1-4 are the measures based on a deformation field and NDM1-10 are the measures that do not require estimation of a deformation field.</i>	122
6.6	<i>All measures for the left ML of subjects. DM 1-4 are the measures based on a deformation field and NDM1-10 are the measures that do not require estimation of a deformation field.</i>	123
6.7	<i>All measures for the right ML of subjects. DM 1-4 are the measures based on a deformation field and NDM1-10 are the measures that do not require estimation of a deformation field.</i>	123
6.8	<i>The sum of the measures of all bundles. DM 1-4 are the measures based on a deformation field and NDM1-10 are the measures that do not require estimation of a deformation field.</i>	124
6.9	<i>p-values for all significance tests. (a): Left CST; (b): Right CST; (c): Left ML; (d): Right ML; (e): Sum of all 4 bundles. p-values between [0.10 0.05] are highlighted in red and p-values less than 0.05 are highlighted in green.</i>	126

List of Tables

3.1	<i>Mean and standard deviation of Cohen's Kappa values between bundles reconstructed by the manual ROI method and the proposed method.</i>	64
3.2	<i>Visual scoring by two experts. Score is given based on how well the reconstructed bundle agrees with known neuroanatomy. 1: Very poor; 2: Poor; 3: Mediocre; 4: Good; 5: Very good. R1 refers to Rater 1; R2: Rater 2; M: Bundle reconstructed with the manual ROI method; A: Bundle reconstructed with the proposed automatic method.</i>	64
3.3	<i>p-values for Wilcoxon signed-rank test on the visual scores for difference of means between manual and automatic results for each bundle.</i>	64
4.1	<i>The error rate of the distances NRFODD and MDF under various registration errors (no error, translations from 2.5 to 10.0 mm and rotations from 0.05 to 0.20 radians). The error rate is defined as the number of times the nearest neighbor of a fiber comes from a different bundle (i.e. the number of rows for which the minimum is not achieved on the 250×250 diagonal blocks) divided by the total number of fibers on the distance matrices.</i>	82

4.2 *Quantitative comparison of the proposed method (P_NRFODD), the proposed method with MDF fiber-to-fiber distance (P_MDF), the naïve maximal overlap method (MaxOverlap) spectral clustering [4, 5] with added cluster selection: (S+CS); and Tract Querying (TQ): [6]. Bundles created by the manual ROI method are used as “ground truth” and the mean \pm standard deviation of BMD and Cohen’s Kappa values between the bundles created by the automatic methods and the “ground truth” are given for each fiber bundle of interest. The best results for both measures are highlighted in bold. Note that BMD is a dissimilarity measure and Cohen’s Kappa is a similarity measure, hence higher values represent better accuracy for Cohen’s Kappa and lower accuracy for BMD.* 83

4.3 *Visual scoring by two experts. Score is given based on how well the reconstructed bundle agrees with known neuroanatomy. 1: Very poor; 2: Poor; 3: Mediocre; 4: Good; 5: Very good. R1 refers to Rater 1; R2: Rater 2; Manual: Bundle reconstructed with the manual ROI method; Auto: Bundle reconstructed with the proposed automatic method.* 83

4.4 *The mean and standard deviation of BMD and Cohen’s Kappa values between results of the proposed method and manual bundles using different training and test sets. Training Set 1 includes subjects 1-10 and its test set includes subjects 11-30; Training Set 2 includes subjects 11-20 and its test set, subjects 1-10 and 21-30; Training Set 3 includes subjects 21-30 and its test set, subjects 1-20.* 91

5.1 *Quantitative comparison of the proposed method and Ugurlu’s method [7].*
Manually created bundles are used as “ground truth” and the mean \pm stan-
dard deviation of BMD and Cohen’s Kappa values over the test set between
the bundles created by the automatic methods and the manual bundles are
given for each positive bundle class. The best results for both measures are
highlighted in bold. Note that BMD is a dissimilarity measure and Cohen’s
Kappa is a similarity measure, i.e. higher values represent better accuracy
for Cohen’s Kappa and lower accuracy for BMD. 105

Chapter 1

Introduction

1.1 Motivation of the Thesis

White matter fibers connect and transfer information among gray matter regions of the brain which are involved in all kinds of sensory and cognitive processes in the brain. Thus, the study of white matter fibers is essential in understanding brain's structural connectivity networks and how brain functionality is affected by pathologies disrupting the network. One specific problem we tackle in this thesis involves quantification and analysis of the structural changes in the major white matter pathways in the brainstem of patients with a brainstem lesion prior to the resection surgery and after the surgery. Our main clinical motivation is to investigate whether the clinically observed changes in the patient's cognitive functions has a statistically significant relationship to the structural changes to the white matter tracts estimated from the pre-op and post-op imaging data. This clinical motivation also provided us the initial motivation for this thesis. Next, we expand on our initial work towards a more general framework of white matter analysis because we notice that the mathematical and computational tools required for the initial task could be generalized and be used in other clinical applications such as population studies or the analysis of other pathologies.

Brain white matter analysis consists of several steps. First step is the acquisition of images in the hospital using a Magnetic Resonance Imaging (MRI) machine. For imaging of white matter fibers, diffusion MRI (DMRI) is used. The second step is the recon-

struction of fiber orientations at each voxel using the DMRI data. The third step is the reconstruction of a digital representation of white matter fibers. This process is known as tractography. It is known however that without any anatomical constraints, tractography algorithms produce a very large number of fibers that do not correspond to any real pathway. Hence, the tractography either has to be anatomically constrained or the produced tracts have to be cleaned up by removing spurious fibers. In clinical practice, each major pathway of interest are separately extracted. The tractography algorithm is constrained using manually selected regions of interest (ROIs) by a neuroanatomy expert and if there are still spurious fibers, they are removed by the expert by either changing the ROIs accordingly or adding regions of avoidance (ROAs). This process is very time consuming, requires expertise in neuroanatomy and is prone to operator bias and error. Hence, the automation of this process is of tremendous importance in neuroimage computing and constitutes the main focus of this thesis.

After accurate digital representation of white matter fibers are achieved, meaningful clinical analysis can be performed. We carried out such an analysis in our TUBITAK Project No. 112E320 titled “Novel Computational Methods in the Analysis of Changes in White Matter Tracts in the Brainstem between Pre-Operative and Post-Operative Images Using Diffusion Tensor Imaging”.

1.2 Contributions of the Thesis

The main contributions of the thesis are three automatic fiber classification methods that are briefly described below:

1. The first fiber classification method was developed specifically for TUBITAK Project No. 112E320 and hence it is designed to work on Diffusion Tensor Imaging (DTI) images and includes some heuristics specific to brainstem fibers. It combines automatic anatomic constraints, a density-based unsupervised clustering algorithm, and a cluster selection methodology to classify the fiber clusters. In order to use unsupervised clustering, a novel fiber-to-fiber dissimilarity measure based on Euclidean distances between points and local fiber orientations is defined.

2. The second fiber classification method can be seen as a generalization of the first method in the sense that it is also based on the principal of combining automatic anatomic constraints, a density-based unsupervised clustering algorithm and a cluster selection methodology but is fundamentally different in several aspects. First, this method is designed for higher-order diffusion orientation models, that is, models that can resolve more than one orientation at each voxel. Second, a novel fiber representation called Neighborhood Resolved Fiber Orientation Distribution(NRFOD) is introduced that uses only the distribution of resolved fiber orientations in the neighborhood along a fiber. Since the representation does not include the spatial position of points on a fiber, it is translation-invariant which makes it more robust when calculating a dissimilarity measure between fibers defined in different spaces, e.g. images of different patients or the same patient taken at different times. This study is published in:

- Devran Ugurlu, Zeynep Firat, Ugur Ture, Gozde Unal, “Neighborhood resolved fiber orientation distributions (NRFOD) in automatic labeling of white matter fiber pathways”, Medical Image Analysis, Volume 46, Pages 130-145, 2018.

3. The third fiber classification method is a supervised classification method that outputs a set of class probabilities for each input fiber. The advantage of this method compared to the previous two is that it does not require the computation of fiber-to-fiber dissimilarity measures and is hence much faster if we disregard the training time and also scales better as the number of input fibers increases. The downside is the requirement for a good training set and a robust fiber representation that is consistent across different spaces. The previously proposed translation-invariant NRFOD representation is utilized to overcome the latter drawback and a method to create a training set with minimal effort is also proposed. This work will be presented in:

- Devran Ugurlu, Zeynep Firat, Ugur Ture, Gozde Unal, “Supervised Classification of White Matter Fibers Based on Neighborhood Fiber Orientation Distributions Using an Ensemble of Neural Networks”, MICCAI Workshop

CDMRI'18, Granada Spain, September 2018.

In addition to the three fiber classification methods, the thesis also includes a fiber bundle to fiber bundle registration method in order to quantify the structural change between pre-op and post-op bundles on a set of 30 patients with brainstem tumors. Statistical analysis is performed to investigate if the structural changes in the bundles have a statistically significant relationship to the change in patient's cognitive functions. A part of this work was presented in the proceedings of:

- Riza Alp Guler, Devran Ugurlu, Zeynep Firat, Ugur Ture, Gozde Unal, “Shape deformation measures for white matter fibers”, in 2016 24th Signal Processing and Communication Application Conference (SIU), pages 1277-1280, May 2016.

Organization of the thesis is as follows: Chapter 2 presents the necessary background in neuroanatomy, MRI, DMRI, image registration, fiber tractography; and a literature review of fiber clustering and classification methods. Chapters 3-5 present the three proposed automatic fiber classification methods. Chapter 6 describes our method of the analysis of structural changes on the corticospinal tract (CST) and the medial lemniscus (ML) from prior to a tumor resection operation and after. Statistical significance tests are performed between various measures of the structural change and neurological assessment of the patient. Chapter 7 concludes the thesis and includes comments on potential future directions.

1.3 List of Abbreviations

Here is the list of mostly used abbreviations in this thesis:

MRI Magnetic Resonance Imaging

DMRI Diffusion Magnetic Resonance Imaging

WM White Matter

DTI Diffusion Tensor Imaging

GQI Generalized Q-sampling Imaging

ODF Orientation Distribution Function

3D 3-Dimensional

2D 2-Dimensional

ROI Region of Interest

ROA Region of Avoidance

CST Corticospinal Tract

ML Medial Lemniscus

ICP Inferior Cerebellar Peduncle

SCP Superior Cerebellar Peduncle

MCP Middle Cerebellar Peduncle

NRFOD Neighborhood Resolved Fiber Orientation Distribution

NRFODD Neighborhood Resolved Fiber Orientation Distribution Distance

Chapter 2

Background

In this chapter, we present the necessary background information for this thesis, including the anatomy of the brain, MRI, diffusion MRI, image registration and fiber tractography. We also give a literature review of fiber clustering and classification methods.

2.1 Neuroanatomy

In this section, which is mainly based on [1], we give a brief introduction to neuroanatomy.

The human nervous system consists of the brain, spinal cord, nerves and ganglia. There are two types of cells in the nervous system: neurons and glia. Neurons carry information from one place to another using electrical or chemical signals. Glia perform various support tasks to help the nervous system function. Neurons have three main parts: a dendritic tree, a cell body and an axon (Figure 2.1). The dendritic tree receives input from other cells, the cell body contains the nucleus and produces proteins and enzymes necessary for the cell, and the axon transmits information to other neurons. The speed of information transfer along a neuron is determined by the degree of myelination. Myelin is a fatty sheath that insulates the axon, allowing electrical signals to jump along the axon and hence travel faster. Myelin is produced by a class of glia cells known as oligodendrocytes. Since myelin is fatty, it is white. Hence, concentrations of highly myelinated neurons are known as white matter and concentrations of unmyelinated neurons are known as gray

matter. Gray matter neurons tend to form a high number of connections to other gray matter neurons and can be thought of as computational cells whereas white matter neurons are specialized for transmitting information quickly over long distances. When a group of axons connect to the same place, they are known as a fiber tract. This grouping usually occurs for neurons that transmit information to long distances and as a result, fiber tracts tend to be white matter. If we make an analogy to conventional computers, gray matter regions are like processing units (e.g. CPU or GPU cores) and fiber tracts are like buses or network cables.

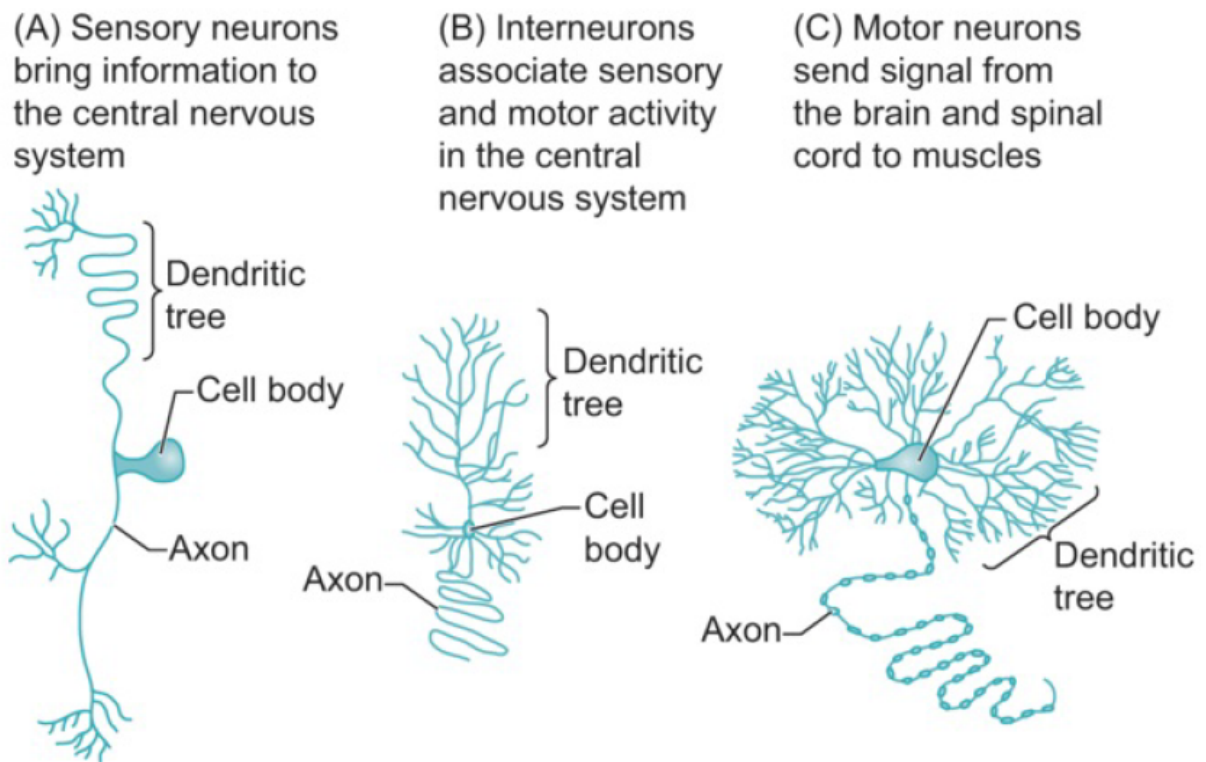


Figure 2.1: *Examples of some nervous system cells (not to scale). Figure reproduced from [1] with permission.*

2.1.1 Anatomical Directions and Planes

This subsection introduces the terminology for anatomical directions and planes. The front of the brain is called **anterior** or **rostral** and the back is called **posterior** or **caudal**. The top of the brain is referred to as **superior** or **dorsal** and the bottom as **inferior** or

ventral. Outside of the brain, dorsal and ventral can have different meanings but this is not important for this thesis. Left and right are still referred to as left and right. Areas near the center of the brain are called **medial** and areas towards the outside of the brain are called **lateral**. In order to get 2D images, the brain is usually sliced using one of three planes. These planes are the following: **Coronal** plane slices from ear to ear and separates the front from the back, **sagittal** plane slices from front to back, separating left and right sides and **axial** (also can be referred to as **transverse** or **horizontal**) plane slices horizontally to separate the top and bottom (Figure 2.2). Another term we will use is **contralateral** which means on the opposite side with respect to the left-right direction whereas **ipsilateral** means on the same side. For example, the right hand is contralateral to the left ear but ipsilateral to the right ear.

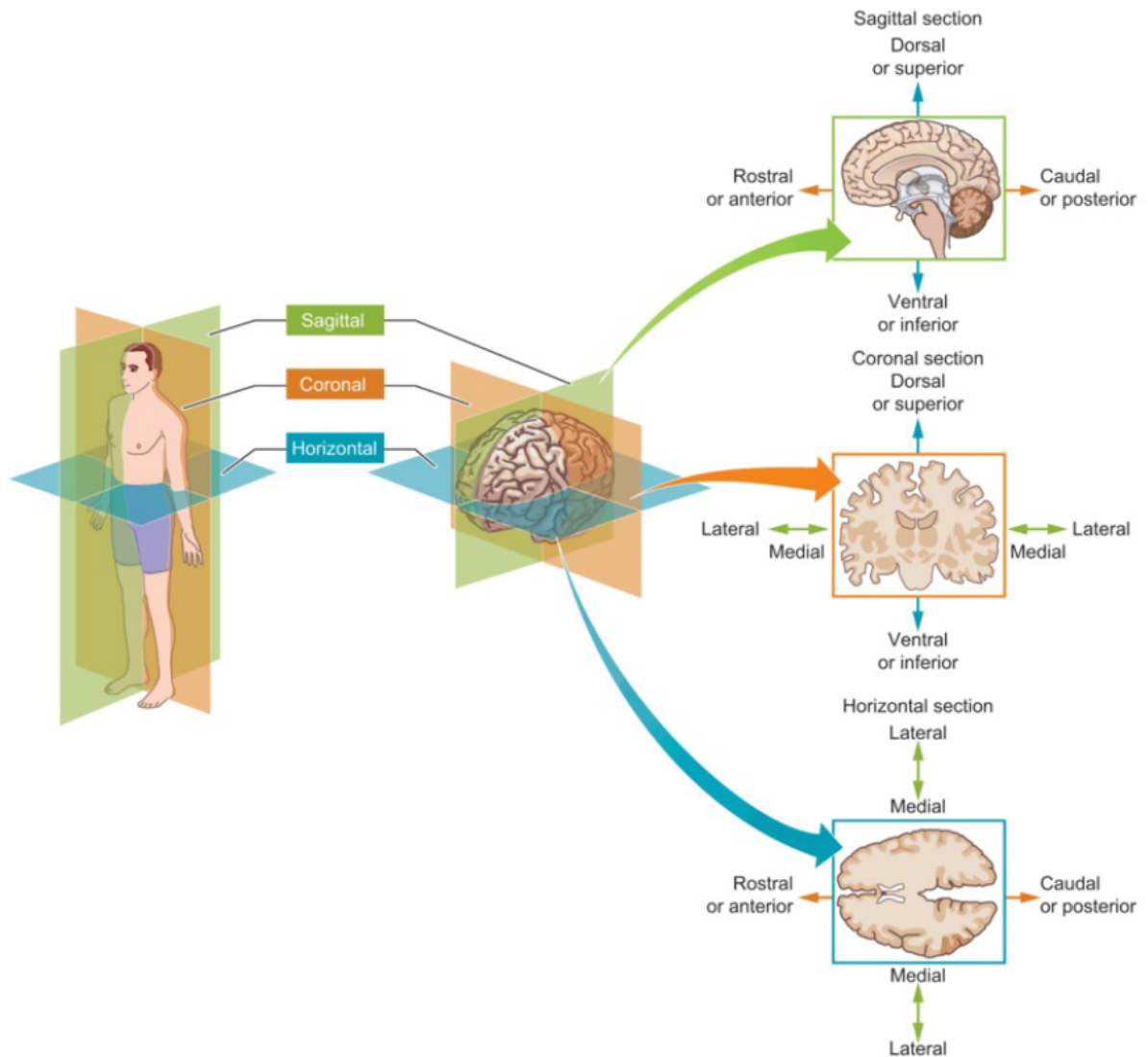


Figure 2.2: *The main planes for viewing the brain. Figure reproduced from [1] with permission.*

2.1.2 Major Subdivisions of the Central Nervous System

The central nervous system is comprised of the brain and the spinal cord. The other parts of the nervous system, such as the nerves sending information to or receiving information from muscles are known as the peripheral nervous system. The central nervous system can be subdivided into seven main parts: (1) the spinal cord, (2) the medulla, (3) the cerebellum, (4) the pons, (5) the midbrain, (6) the hypothalamus and thalamus (diencephalon), and (7) the cerebral cortex. A depiction is shown in Figure 2.3 and

brief descriptions for each subdivision are given below:

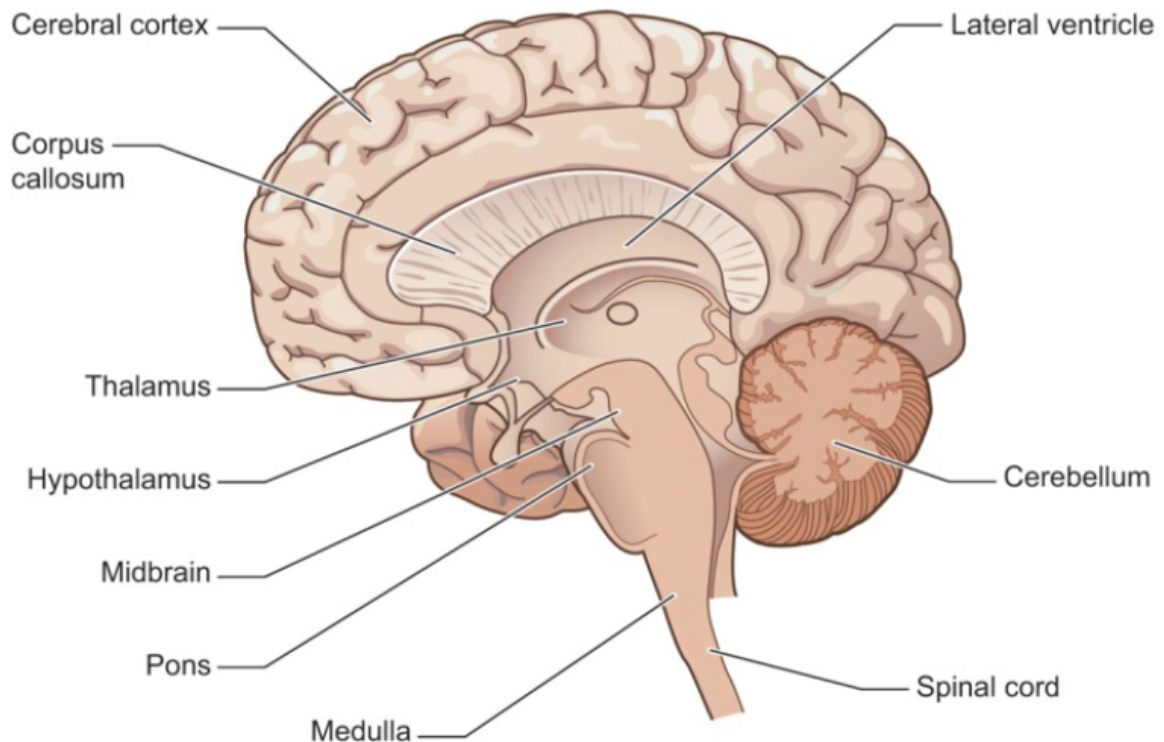


Figure 2.3: *A sagittal view of the major subdivisions of the human brain. The medulla, pons and midbrain together are called the brainstem. Figure reproduced from [1] with permission.*

Spinal Cord: The information sent to the brain by the sensory neurons and the motor commands from the brain to the muscles mostly pass through the spinal cord.

Medulla: Medulla is directly superior to the spinal cord and contains many of the cell bodies of the 12 cranial nerves. The functions and entry and exit locations of the cranial nerves are illustrated in Figure 2.4. Second, medulla is the region where most of the motor neurons cross to the contralateral side. This crossing is why motor function is contralateral, meaning the left side of the brain controls the motor function of the right side of the body and the right side of the brain controls the left side of the body. Third, the medulla controls many vital functions and reflexes, such as respiration and heart rate. Fourth, the medulla contains neurons of the reticular activating system which is important for overall arousal and attention and

the regulation of sleep-wake cycles.

Cerebellum: The cerebellum is posterior to the medulla and is important for the regulation of muscle tone and guidance of motor activity. Damage to the cerebellum does not cause paralysis but causes unbalanced and imprecise movement.

Pons: Pons is directly superior to the medulla and anterior to the cerebellum. It is the main bridge that connects the cerebellum to the rest of the brain. It also connects most of the cranial nerves to the brain. In addition, it is involved in the control of eye movements and balance.

Midbrain: Midbrain is superior to the pons. It contains the inferior colliculus, the superior colliculus and the nuclei of the cells that form some of the cranial nerves. The inferior colliculus plays a role in orienting us to auditory stimuli and the superior colliculus plays a role in orienting us to visual stimuli.

Hypothalamus: Hypothalamus is part of the diencephalon and its main function is to help maintain the body's equilibrium.

Thalamus: Thalamus is part of the diencephalon and superior to the midbrain. It is a large relay center that sends sensory information coming from the body to the appropriate parts of the cerebral cortex and similarly, sends the motor commands coming from the cortex to the appropriate parts of the body.

Cerebral Cortex: The cerebral cortex is the outer layer of the cerebrum and is mostly made up of highly concentrated gray matter. It can be thought of as the primary computation center of the brain and is responsible for most of the functions associated with being human like speech and decision making. The cortex has many bumps with valleys between them. The purpose of these bumps is to increase the surface area so that more cells can be packed into a small space. Each bump is called a gyrus (plural: gyri) and each valley is called a sulcus (plural: sulci). A particularly deep valley is called a fissure. The cortex has three major fissures called the central fissure, the Sylvian (lateral) fissure and the longitudinal fissure. The cortex is physically divided into a left and a right half and these are called cerebral hemispheres.

The three major fissures divide each hemisphere into four major parts and these are called the frontal lobe, the temporal lobe, the parietal lobe and the occipital lobe (Figure 2.5).

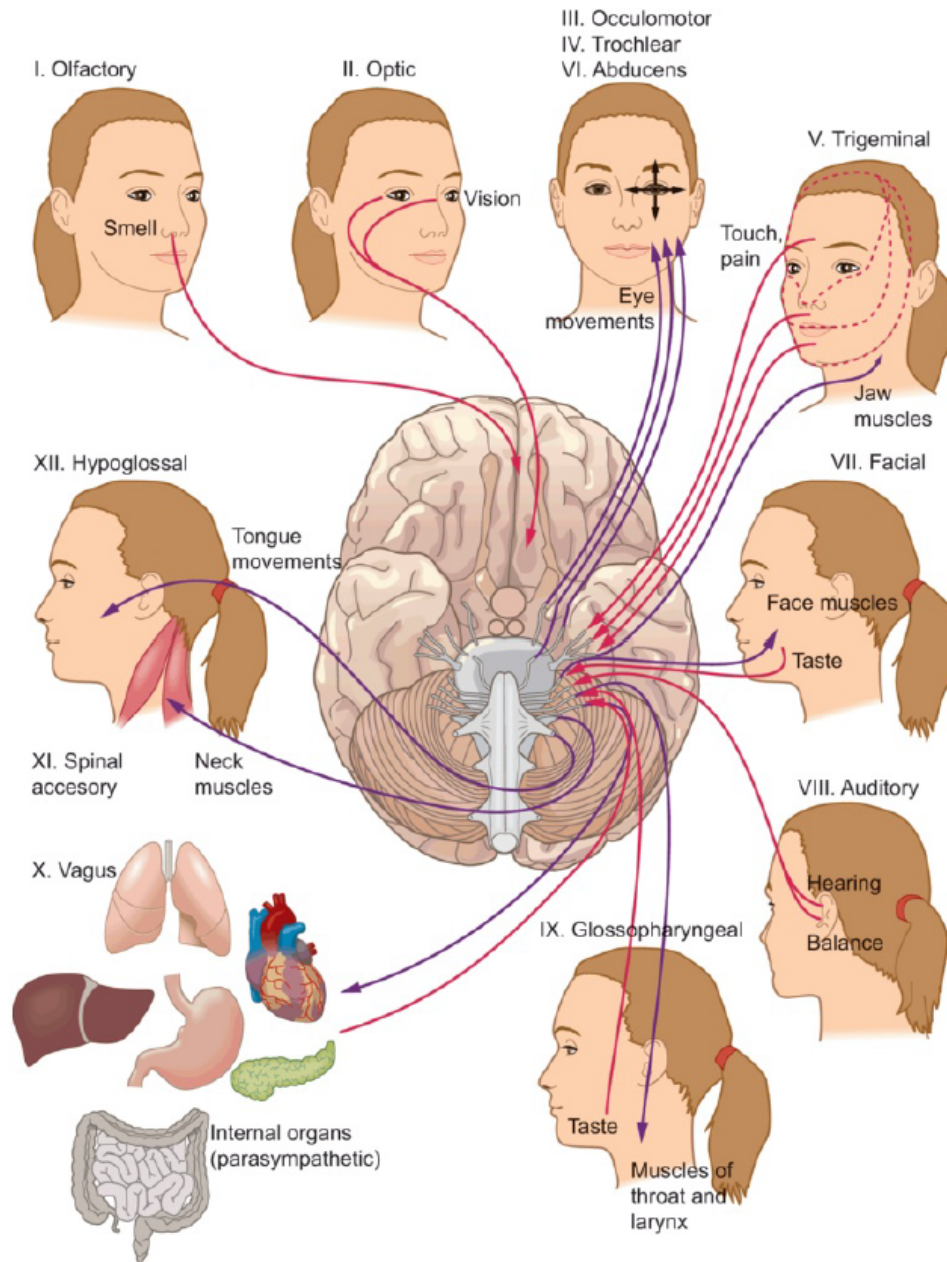


Figure 2.4: *Functions of the 12 cranial nerves and their entry and exit locations. Figure reproduced from [1] with permission.*

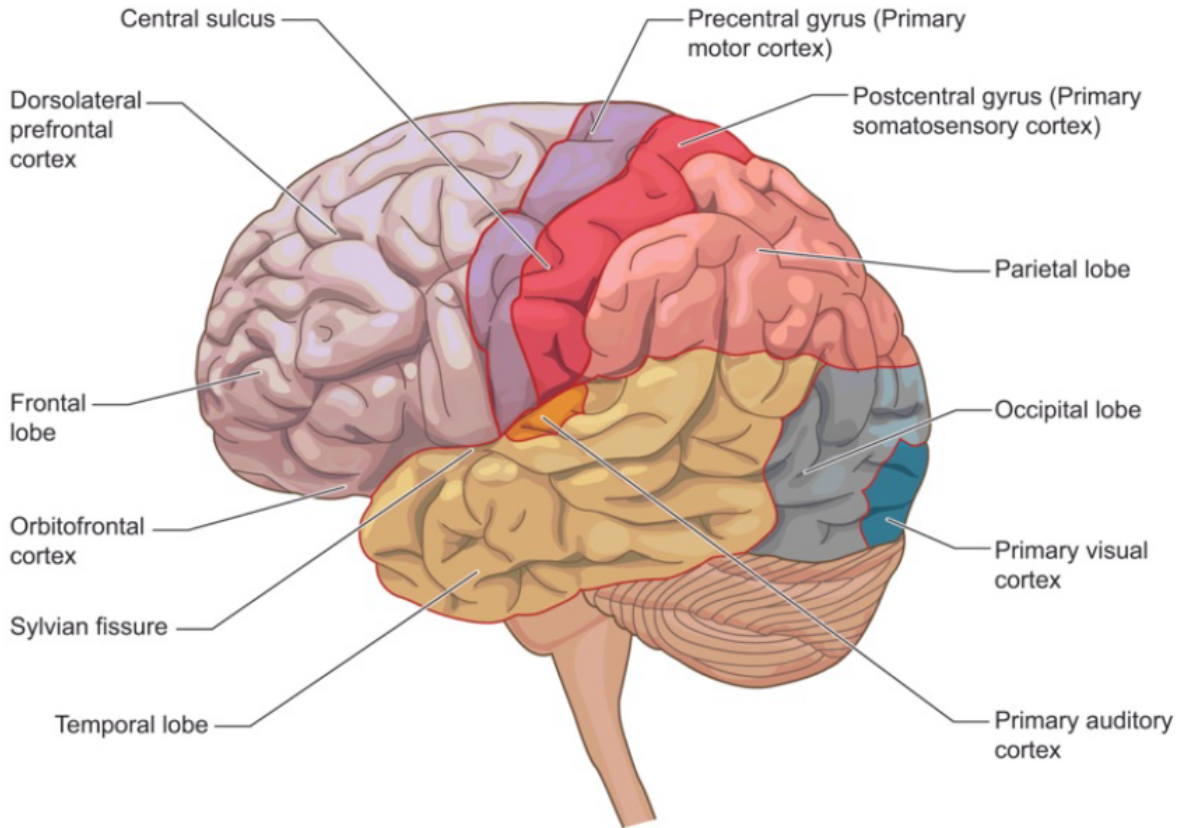


Figure 2.5: *An illustration of the cerebral cortex. Figure reproduced from [1] with permission.*

2.1.3 Major Fiber Tracts in the Brainstem

While many of the methods proposed in this thesis are applicable to any fiber tract in the brain, the validations were performed on the major fiber tracts in the brainstem because of the effort involved in the manual extraction of fiber tracts. Therefore, we will only describe the major fiber tracts in the brainstem in this section.

Recent literature describes five major white matter (WM) pathways of interest for the brainstem: (i) corticospinal tract (CST); (ii) medial lemniscus (ML); (iii) middle cerebellar peduncle (MCP); (iv) inferior cerebellar peduncle (ICP) and (v) superior cerebellar peduncle (SCP) [8, 9, 10].

The CST is a major efferent (transmitting away from the central nervous system) projection pathway originating mainly from the primary motor cortex, primary somatosensory

cortex and premotor and supplementary motor areas. It descends from the cortex to the spinal cord passing through the posterior limb of the internal capsule and then the brainstem [11] (p. 687).

The ML is a major afferent (transmitting to the central nervous system) sensory pathway and is mainly associated with tactile and proprioceptive functions. It ascends from the spinal cord into the medulla where it decussates to cross to the contralateral side and ascends medially through the brainstem and midbrain and terminates at the thalamus. It is posterior to the CST at pons level. In neuroanatomical literature, ML is usually said to project from the thalamus to mainly the primary somatosensory cortex [11] (pp. 587-589), [12, 13], however some recent studies mention its projections to the primary motor cortex as well [14, 15, 16].

The SCP is a major efferent pathway that emerges from the deep cerebellar nuclei and travels through the brainstem to the contralateral motor areas of the cerebral cortex via the thalamus [17, 18]. MCP, which has a “horse-shoe” appearance, is a major afferent pathway to the cerebellum, and carries fibers from the contralateral cerebral cortex across the midline of the cerebellum via pontine nuclei to the cerebellar cortex. The ICP is a major afferent pathway connecting fibers from the spinal cord and the olivary nucleus to the cerebellum [17]. The ICP also makes efferent connections from the cerebellum toward the vestibular nuclei along the border of the pons and medulla [19].

2.2 Magnetic Resonance Imaging (MRI)

MRI is fundamentally based on manipulating the magnetic moment of hydrogen atoms in the body. This is done in a specific way to create an oscillating magnetic field which, due to Faraday’s law, produces a current on a receiver coil. While this sounds simple, it is actually quite complicated because the behavior of an atom cannot be predicted by the classical mechanical perspective and requires a quantum mechanical analysis. Fortunately, when it comes to practical aspects of MRI, an oversimplified classical picture leads to conclusions that are also predicted by the quantum mechanical analysis. In this section, the physical principles of MRI will be explained from the classical mechanics perspective

in a simplified manner but a brief mention of quantum mechanics will be made when appropriate. For a detailed coverage of MRI principles and the quantum mechanical perspective, the reader is referred to [2] and [20].

Let us first start by thinking of a proton as a spinning ball. Under this analogy, which is actually inaccurate, the proton has an angular momentum and a magnetic moment parallel to its rotation axis. When a constant external magnetic field is present, similar to the behavior of a spinning top under the influence of gravity, the proton's rotation axis and hence its magnetic moment vector will precess around the direction of the external magnetic field (Figure 2.6). The frequency of this precession is known as the Larmor frequency and is directly proportional to the strength of the external magnetic field:

$$\omega_0 = \gamma B_0 \quad (2.1)$$

where ω_0 is the Larmor frequency in megahertz(MHz), γ is the gyromagnetic ratio of the specific particle and B_0 is the strength of the constant external magnetic field in tesla (T). Note that the gyromagnetic ratio is sometimes defined such that its unit is rad/s/tesla but we are using MHz/tesla. It can be converted to rad/s/tesla easily by multiplying with 2π which will also convert the Larmor frequency to rad/s from MHz.

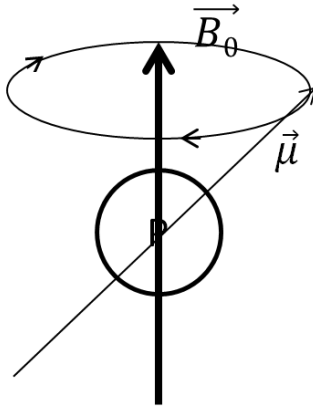


Figure 2.6: An illustration of the magnetic moment ($\vec{\mu}$) of a proton precessing around the constant magnetic field \vec{B}_0 .

In practice, it is not possible to measure the magnetic moments of single protons in an MRI experiment so “net magnetization” is defined as the local magnetic moment per

unit volume as follows:

$$\mathbf{M} = \frac{1}{V} \sum_{i=\text{protons in } V} \boldsymbol{\mu}_i \quad (2.2)$$

where $\boldsymbol{\mu}_i$ is the individual magnetic moment of proton i and V is a volume small enough that the external magnetic field is constant or nearly constant in the volume but big enough to contain a large amount of protons. Under a constant external magnetic field \mathbf{B}_0 , the net magnetization is parallel to the external magnetic field because the perpendicular components of individual magnetic moments cancel each other out as they are randomly distributed on the perpendicular plane. The reality is different from the classical picture. In quantum mechanics, spin is an intrinsic property of many particles and it is an angular momentum that is not caused by a rotation. It simply always exists and the direction of the spin angular momentum is the same as the direction of the magnetic moment for particles with a positive gyromagnetic ratio. The proton is one such particle. Without an external magnetic field, the direction of the spin angular momentum is random and hence the net magnetization is zero. Under a constant external magnetic field \mathbf{B}_0 , at thermal equilibrium, the spin angular momentum vectors will exhibit an anisotropic distribution, slightly favoring the direction of \mathbf{B}_0 . This produces a net magnetization parallel to \mathbf{B}_0 . Note that this is the same conclusion predicted by the incorrect classical picture. The magnitude of the net magnetization at thermal equilibrium is predicted by quantum mechanics as

$$M_0 = \frac{\rho_0 \gamma^2 \hbar^2}{4kT} B_0 \quad (2.3)$$

where ρ_0 is the spin density, \hbar is the Planck constant, k is the Boltzmann constant and T is the temperature in Kelvin (see the quantum mechanical discussion in [2]). The behavior of net magnetization, which is produced by a huge number of protons, can be studied using classical mechanics. An ensemble of spins that behave similarly are sometimes called a spin-isochromat and when discussing spin in the context of MRI from a classical mechanics perspective, spin usually refers to a spin-isochromat, not individual spins which can only be discussed with a quantum mechanics perspective. The component of net magnetization that is parallel to \mathbf{B}_0 cannot be measured because it is very small compared to the external

field \mathbf{B}_0 . Hence, at equilibrium under \mathbf{B}_0 , there is no MRI signal. In order to receive a signal, the net magnetization vector must be flipped away from \mathbf{B}_0 . This can be done by introducing a second external magnetic field \mathbf{B}_1 that precesses around \mathbf{B}_0 with the Larmor frequency ω_0 . In practice, this is done by a radiofrequency (RF) pulse perpendicular to \mathbf{B}_0 with frequency ω_0 . Flipping the net magnetization using an RF pulse is illustrated in Figure 2.7 on a rotating reference frame that rotates around the z-axis with frequency ω_0 . In the stationary frame (from the perspective of someone standing in the imaging room), the net magnetization vector will spiral down to the transverse plane precessing around the z-axis. Once the net magnetization has components on the transverse (xy) plane, the net magnetization vector on the transverse plane will precess with frequency ω_0 around the z-axis in the stationary frame. The oscillating magnetic field induces a current on a receiver coil due to Faraday's law, creating an MRI signal. Flipping the magnetization vector 90 degrees so that it is entirely on the transverse plane is usually preferred as this provides the maximum signal. The RF pulse that achieves this is called a 90° RF pulse. Another commonly used pulse is the 180° pulse, the purpose of which will be explained later. Flipping the magnetization vector using an RF pulse is also called excitation. In the human body, the most abundant nuclei with a high gyromagnetic ratio is hydrogen and therefore, the MRI signal is dominated by hydrogen. Hydrogen has a gyromagnetic ratio of 42.58 MHz/T so in a 3T MRI machine, assuming the machine applies a constant \mathbf{B}_0 with magnitude 3T, the Larmor frequency of hydrogen nuclei at equilibrium will be 127.74 MHz which is in the radiofrequency range. This is why the excitation pulses are called RF pulses. Since MRI requires only magnetic fields and RF pulses, it is safer than imaging methods like computed tomography (CT) and positron-emission tomography (PET) that require ionizing radiation.

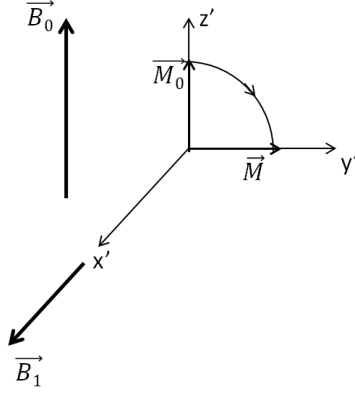


Figure 2.7: *An illustration of the net magnetization vector being flipped from the z -direction into the transverse plane using an RF pulse. The primed reference frame is a rotating frame that rotates with frequency ω_0 around the z -axis.*

2.2.1 Relaxation

Right after the application of a 90° pulse to the system at equilibrium, the net magnetization is entirely on the transverse plane with magnitude equal to the net magnetization at equilibrium \mathbf{M}_0 . This situation creates the highest intensity signal. After this moment, the signal starts decaying due to two interactions: spin-lattice and spin-spin.

2.2.1.1 Spin-lattice Interaction and T1 Relaxation

The equilibrium state is the minimum energy state and the RF pulse introduces energy into the system hence moving it out of equilibrium. The system will gradually return back to the minimum energy state by transferring away energy. The spin energy is transferred to the lattice of nearby atoms and this is known as spin-lattice interaction. Let us call the net magnetization component parallel to \mathbf{B}_0 the longitudinal magnetization and denote it $\mathbf{M}_z = M_z \mathbf{z}$ and similarly, let us call the net magnetization component on the xy -plane the transverse magnetization and denote it $\mathbf{M}_{xy} = M_x \mathbf{x} + M_y \mathbf{y}$. The magnitude of the longitudinal magnetization will increase with time until it reaches M_0 at the equilibrium state and hence the transverse magnetization will decay with time, decreasing the intensity of the MR signal. The growth rate of the longitudinal magnetization is proportional to

the difference between M_0 and M_z as follows:

$$\frac{dM_z}{dt} = \frac{1}{T_1}(M_0 - M_z) \quad (2.4)$$

where T_1 is an experimental parameter and is dependent on tissue type. The decay of the MR signal due to the increase of longitudinal magnetization is called T1 relaxation and its tissue dependence is the basis of contrast in “T1 images”.

2.2.1.2 Spin-spin Interaction and T2 Relaxation

In addition to the external magnetic field, the spins are also affected by the local fields of their neighbors. This leads to slight variations in the precession frequencies of individual spins. As a result of this spin-spin interaction, individual magnetic moments “dephase”. In the rotational frame, this can be seen as individual moments having the same direction at first but then “fanning out” with time. Since the transverse magnetization is the sum of individual moments on the transverse plane, “dephasing” reduces the magnitude of the transverse magnetization (Figure 2.8). The decay rate of the transverse magnetization can be written in the rotating frame as

$$\left(\frac{d\mathbf{M}_{xy}}{dt}\right)' = -\frac{1}{T_2}\mathbf{M}_{xy} \quad (2.5)$$

where T_2 is an experimental parameter dependent on tissue type and prime denotes the rotating frame. The decay of transverse magnetization due to spin-spin interactions is called T2 relaxation and its tissue dependence is the basis of contrast in “T2 images”.

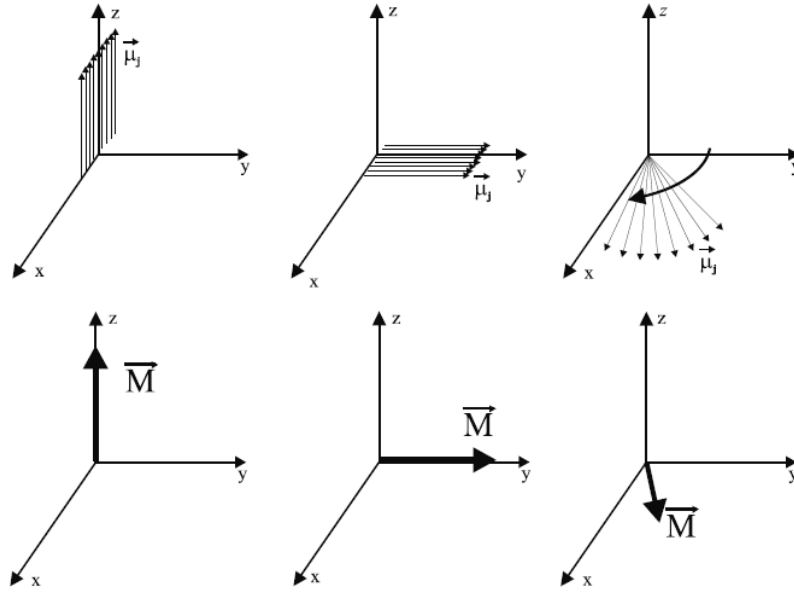


Figure 2.8: *Illustration of T_2 relaxation. Individual magnetic moments are illustrated in the up row and the net magnetization is illustrated in the bottom row. Left is the equilibrium state, middle is the state right after a 90° pulse and right shows how the magnetization decays due to individual moments having different phase on their precession around the z -axis. Figure reproduced from [2] with permission.*

2.2.2 Signal Acquisition with Basic Pulse Sequences

2.2.2.1 Free Induction Decay (FID)

The simplest MRI experiment is to receive a signal from the whole sample. After a 90° RF pulse is used, the precessing magnetization on the transverse plane induces a current on a properly placed RF receiver coil due to Faraday’s law. The signal oscillates with frequency ω_0 in the stationary (laboratory) frame so in practice, the signal is demodulated to remove the oscillation which is equivalent to measuring the signal in the rotating frame (Figure 2.9). This experiment is called free induction decay (FID) and is usually used to tune the MRI machine. MRI experiments are generally repeated to achieve better signal-to-noise ratio and the time it takes for one “cycle” is known as repetition time (T_R).

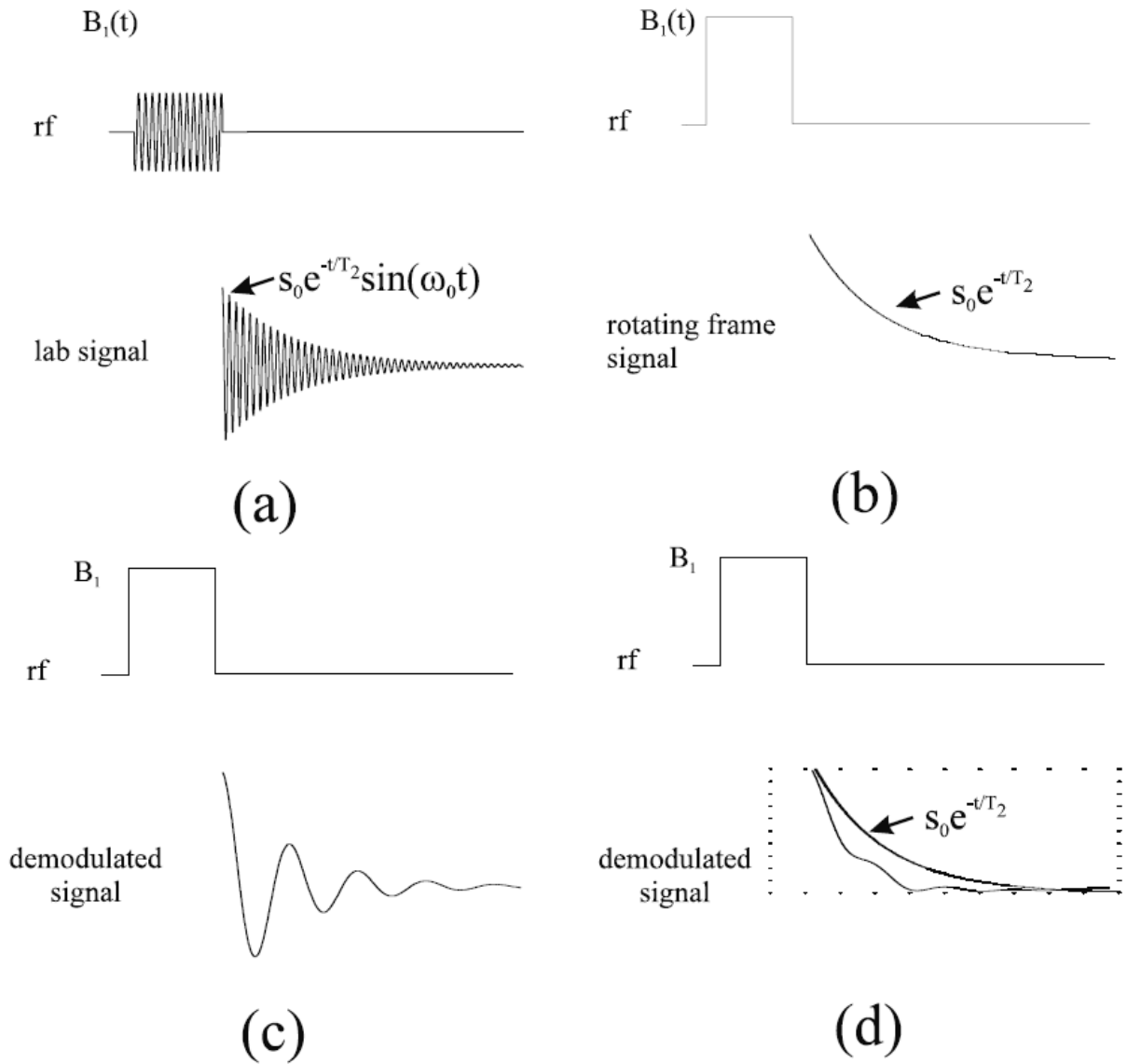


Figure 2.9: (a) The FID signal in laboratory frame. (b) The FID signal in rotating frame. (c) The demodulated FID signal when the demodulation is not exactly at the Larmor frequency. (d) The total demodulated FID signal from several ensembles each with slightly different Larmor frequencies. Figure reproduced from [2] with permission.

2.2.2.2 The Spin-Echo

In section 2.2.1.2, the T_2 relaxation was introduced. In reality, MRI machines are not perfect and the \mathbf{B}_0 field is not constant and has small inhomogeneities. This is a second cause of dephasing and is known as T_2' relaxation. The combined effect of T_2 and T_2' is

known as T_2^* relaxation and they are related as

$$\frac{1}{T_2^*} = \frac{1}{T_2} + \frac{1}{T_2'} \quad (2.6)$$

T_2' is reversible and the spin-echo experiment is designed to do just that and hence measure T_2 decay. In the spin-echo experiment, after the initial 90° pulse along the x' -axis, the spins will dephase due to T_2^* relaxation. After a time τ , a 180° pulse along the y' -axis is used to invert the sign of the phases. As a result, after another time τ , the spins will rephase, creating signal again. This second signal is called an echo and 2τ is called echo time (T_E). A sequence diagram and the corresponding MRI signal is illustrated in Figure 2.10 and the dephasing and rephasing of spins is illustrated on the rotating frame in Figure 2.11.

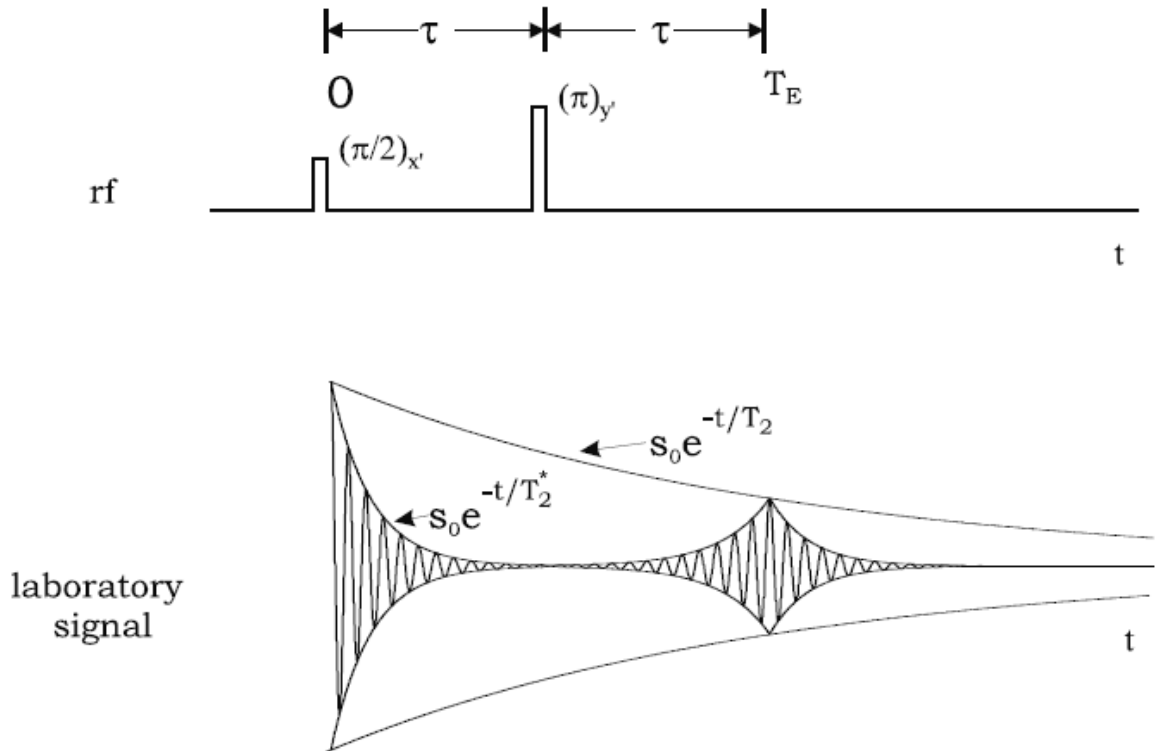


Figure 2.10: *The sequence diagram and corresponding MRI signal in a spin-echo experiment. Figure reproduced from [2] with permission.*

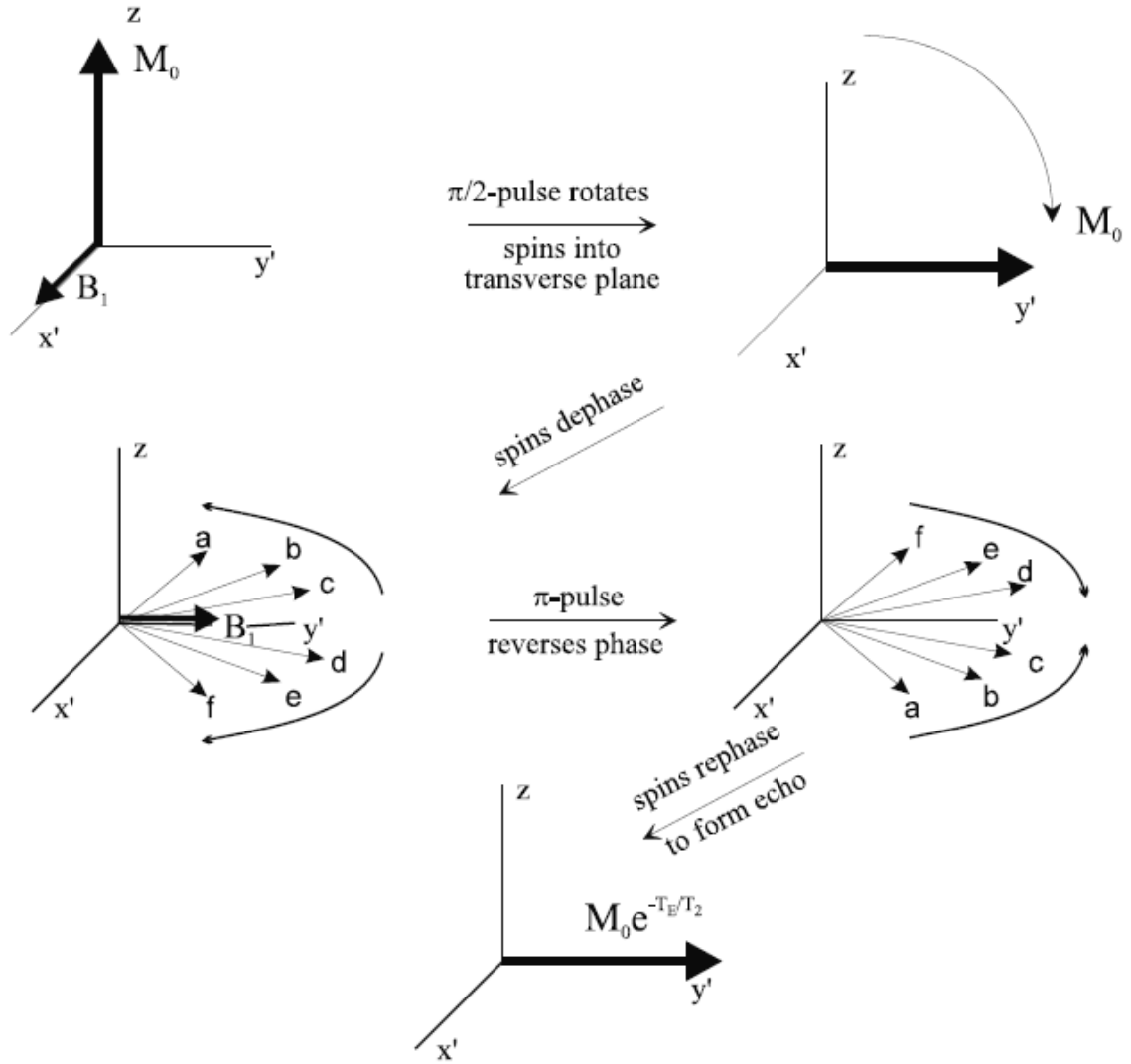


Figure 2.11: *Illustration of the dephasing and rephasing of spins on the rotating frame in a spin-echo experiment. Figure reproduced from [2] with permission.*

2.2.2.3 Inversion Recovery

Inversion recovery experiment is designed to measure T1. The longitudinal magnetization is first reversed by applying a 180° pulse and then after a time T_I , a 90° pulse is used. Since the magnetization will change from $-\mathbf{M}_0$ to \mathbf{M}_0 after the 180° pulse, assuming the imaged sample has uniform T1, there exists a time T_I such that the signal will be zero after the 90° pulse. By varying the time T_I and determining when the signal vanishes, T1 can be determined. More specifically, the longitudinal magnetization after the 180° pulse

is

$$M_z(t) = -M_0 e^{-t/T_1} + M_0(1 - e^{-t/T_1}) = M_0(1 - 2e^{-t/T_1}), \quad 0 < t < T_I \quad (2.7)$$

which is zero when $T_I = T_1 \ln 2$. The sequence diagram for an inversion recovery experiment is given in Figure 2.12.

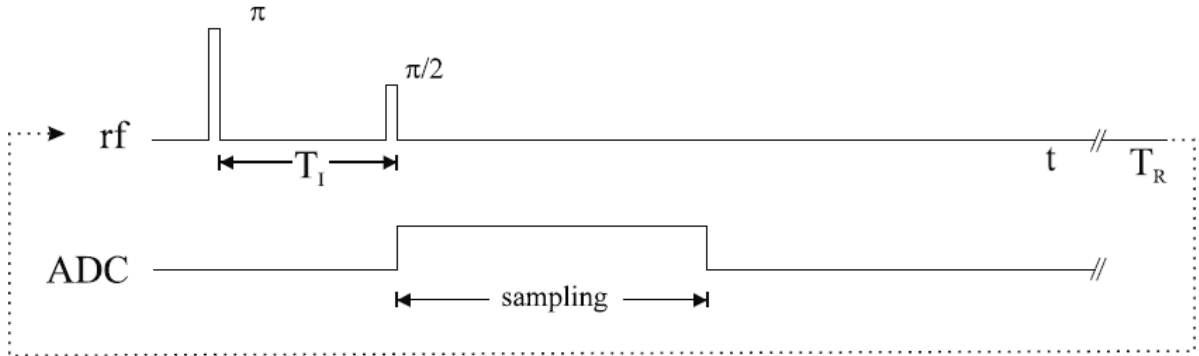


Figure 2.12: *The sequence diagram for an inversion recovery experiment. ADC stands for analog-to-digital converter and converts the analog MRI signal to digital. Figure reproduced from [2] with permission.*

2.2.3 Spatial Encoding and k-space

In the previous section, some basic sequences to acquire signal from a sample globally were introduced. However, in order to create a meaningful image, we need contrast between different volume elements of the sample. If we think of a classical grayscale 2D image, it is a rectangular matrix with values between 0 and 255. Similarly in MRI, we want to construct a 3D image where the volume is divided into a 3D matrix of volume cells (called “voxels”) with some intensity value in each voxel. Let us first see how this can be done in 1D and then generalize to the 3D case.

Suppose a constant linear magnetic field gradient, or shortly “gradient”, G is added along the z -axis. The z -component of the external magnetic field can then be written as

$$B_z(z) = B_0 + zG. \quad (2.8)$$

Due to (2.1), we then have

$$\omega(z) = \omega_0 + \gamma z G. \quad (2.9)$$

Using a gradient to establish a relationship between the position of spins along a certain direction and their precession frequencies in this manner is called frequency encoding along that direction. Since the frequency of precession now varies along the z -axis, the phase will be shifted as well depending on how long the gradient is applied. After a time t , the accumulated phase due to the gradient can be written as

$$\phi_G(z, t) = -2\pi\gamma z G t \quad (2.10)$$

where the phase unit is radians, or equivalently

$$\phi_G(z, t) = -2\pi k z \quad (2.11)$$

where

$$k(t) = \gamma G t \quad (2.12)$$

is the spatial frequency. In 1D, the k -space is the 1D space of possible k values so it is also known as the spatial frequency domain. Since the MRI signal is the sum of all magnetic moments, ignoring relaxation effects, the demodulated signal (with ω_0) can be written as

$$s(k) = \int \rho(z) e^{-i2\pi k z} dz \quad (2.13)$$

where $\rho(z)$ is the spin density. This equation shows a very important result. Under a constant linear gradient and ignoring relaxation effects, the MRI signal is the Fourier transform of the spin density. So if we have the signal for all k , the inverse Fourier transform gives us the 1D spin density image. Since spin densities of different tissues are different, the spin density image is an image with tissue contrast. The aim of a pulse sequence then would be to sample “enough” values of k to allow a good reconstruction of the spin density. An example pulse sequence to achieve this is known as the gradient echo and is illustrated in Figure 2.13. The generalization to 3D is straightforward. The signal will now be the 3D Fourier transform of the spin density:

$$s(k_x, k_y, k_z) = \int \int \int \rho(x, y, z) e^{-i2\pi(k_x x + k_y y + k_z z)} dx dy dz \quad (2.14)$$

and as in the 1D case, we want to use a pulse sequence that allows sufficient coverage of the now 3D k -space. The simplest solution is to apply separate linear gradients on the 3 dimensions and use a 1D gradient echo sequence multiple times to sample one line of the k -space each time. For example, if we want to create a $256 \times 256 \times 128$ image, we could repeat a 1D gradient echo sequence for the x -direction 256×128 times for every combination of k_y and k_z values. Of course the downside compared to the 1D case is that the imaging time required has now increased 256×128 times.

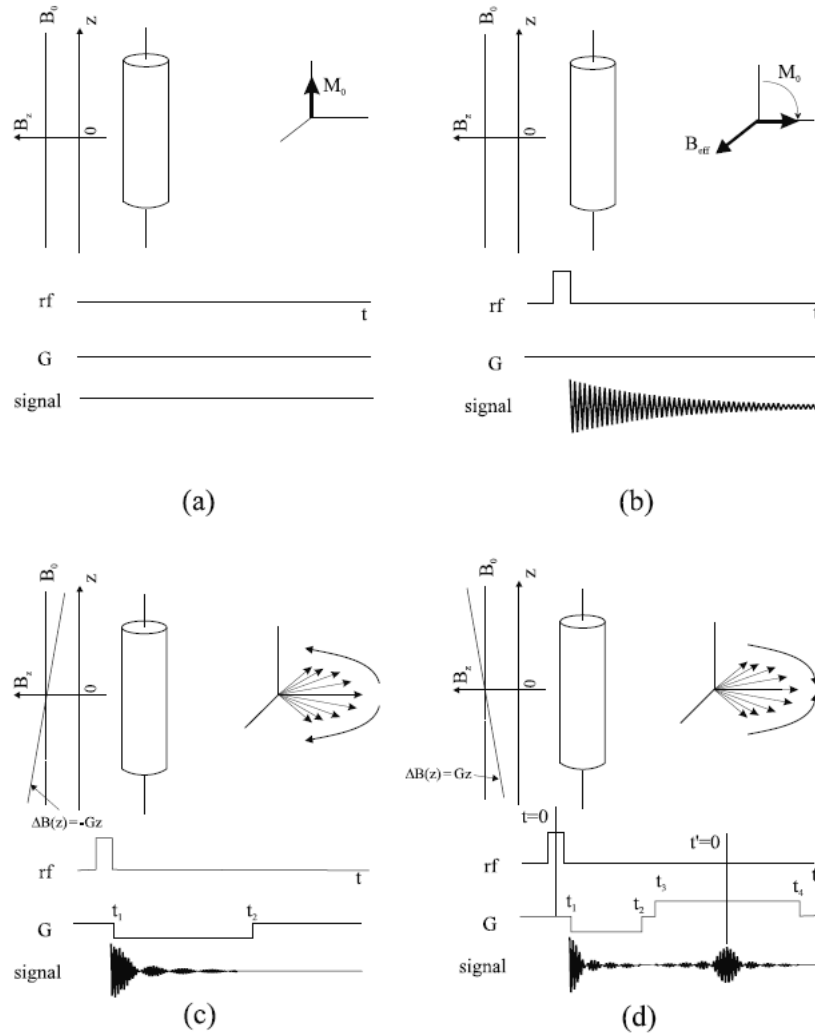


Figure 2.13: *Illustration of a 1D MRI experiment where a hypothetical 1D “cylinder” with random spin distribution is imaged. (a) The thermal equilibrium condition. With no gradient or rf pulse, there is no signal. (b) A 90° RF pulse is applied but no gradient. The signal gradually decays due to relaxation. (c) After a 90° RF pulse, a gradient is applied. Since the gradient will also dephase the spin in addition to relaxation, the signal decays more rapidly. Note that only positive k values can be sampled here. (d) A gradient echo sequence. First, a negative gradient is applied and after some time $(t_2 - t_1)$, the gradient is reversed. As a result, the dephasing due to the gradient will cancel out after $(t_2 - t_1)$ time and we get an “echo”. Note that if the signal is sampled during time t_3 to t_4 , both negative and positive values of k are sampled. Figure reproduced from [2] with permission.*

2.2.4 Diffusion Magnetic Resonance Imaging (DMRI)

So far, we have seen that the MRI signal can be used to estimate spin density and that the MRI signal is dominated by hydrogen nuclei which are very abundant in the body and have a high gyromagnetic ratio. Since most of the hydrogen resides in water, a spin density image is approximately a water density image. If we can measure the density of water, can we measure its motion as well? The answer is yes and diffusion MRI is a technique that allows measuring the diffusion of water. The diffusion of water provides very valuable information because the diffusion is anisotropic when it is constrained by surrounding tissue. In the brain, white matter tracts restrict water diffusion perpendicular to their trajectory so in principle, by measuring water diffusion anisotropy, the local orientation of white matter tracts can be estimated. In this section, how water diffusion can be measured by MRI is briefly explained. For more details, the reader is referred to [3].

In section 2.2.3, the dephasing and rephasing effect of gradients were explained but the nuclei were assumed to be stationary in space. This is actually not true because hydrogen atoms can move. Of course, when designing a pulse sequence to obtain a spin density image, we try to minimize the effect of motion but if we are trying to detect motion, we can sensitize the signal to motion by using an appropriate pulse sequence. In diffusion-weighted MRI or shortly diffusion MRI (DMRI), the signal is sensitized to the diffusion of water. This is done as follows: first, a dephasing gradient is applied. This gradient “tags” the hydrogens with a specific phase. It is easier to understand the concept on a 2D plane so let us say the gradient is applied along the x -axis. Then, the phase will change along the x -axis but will be the same along the y -axis. Then, we wait for a while to give water time to diffuse. As a result, hydrogen atoms will change location and any movement along the x -axis will result in an “out of phase” spin, that is, a spin that has different phase than the other spins on the same position on the x -axis. The more diffusion along the x -axis, the more the spins will dephase, leading to signal loss. After we wait for a certain time τ , a rephasing gradient is applied to bring the spins back to the same phase. However, only the spins that have not moved along the x -axis will come back to the same phase. This is illustrated in Figure 2.14. Thus, if there is a high amount of water diffusion along the x -axis, the signal loss due to diffusion will be high. It is important to mention that

the diffusion along the y -axis will not lead to phase incoherence and will not affect the signal. This means that only diffusion along a specific direction can be measured at a time. Hence, increasing the number of directions the diffusion is measured in will increase scan time. This is a significant problem in practice because even with modern MRI machines, measuring more than 100 directions at an acceptable spatial resolution and field of view (FOV) can take more than 30 minutes and as a result, most clinical data includes only 16 or 32 directions.

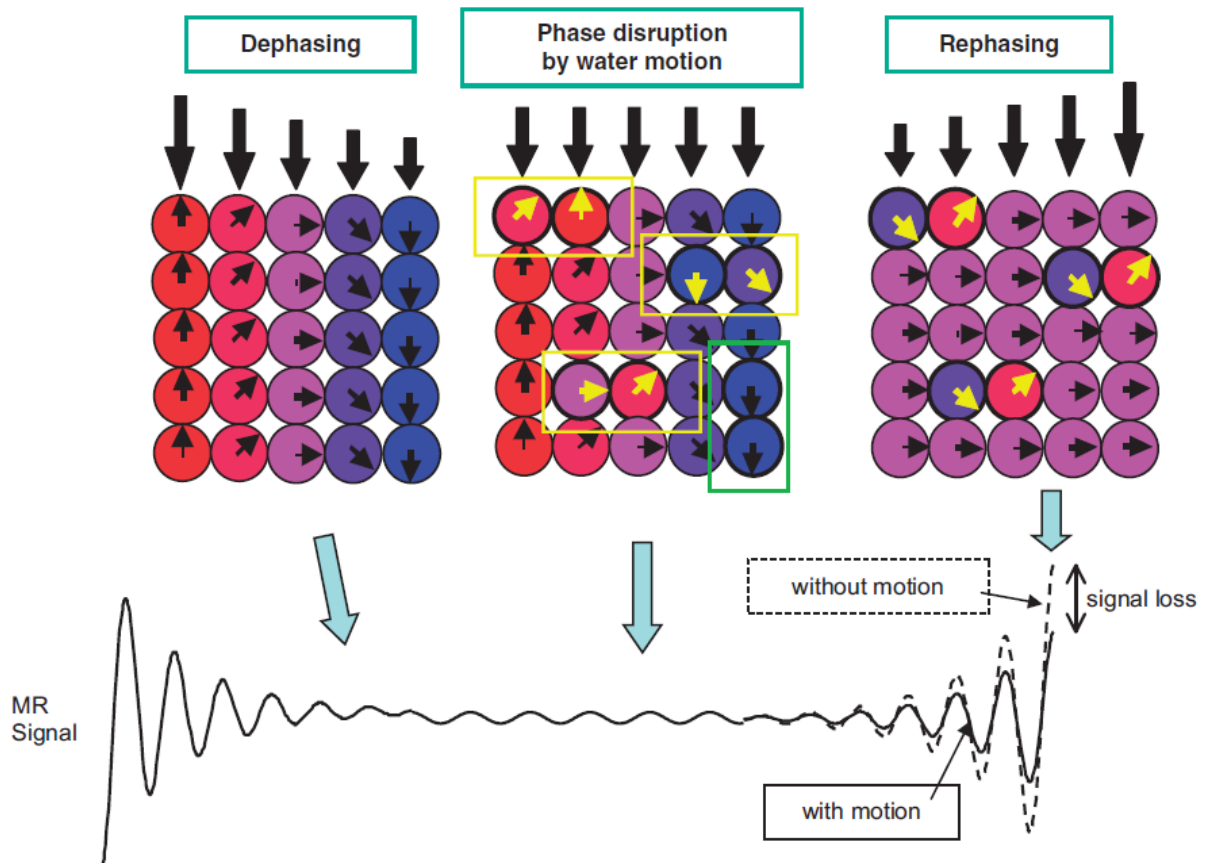


Figure 2.14: *Illustration of how water diffusion can lead to signal loss after a dephasing and a subsequent rephasing gradient. Each circle should be considered a spin-isochromat, not individual spins and the vectors show the magnetic moment direction on the rotating frame. Note that only diffusion along the gradient axis will lead to signal loss (yellow boxes). Diffusion along the y -axis does not lead to phase incoherence (green box). Figure reproduced from [3] with permission.*

Let us now derive in more detail how the signal intensity changes due to diffusion under the assumption of Gaussian diffusion. Accumulated phase due to a gradient was given in (2.10). If we call the length of the gradient δ , length meaning the duration the gradient is applied, equation 2.10 can be written as

$$\phi_G(z) = e^{-2\pi i \gamma z G \delta}. \quad (2.15)$$

If we assume that a hydrogen atom at $z = 0$ on time $t = 0$ exhibits Brownian motion along the z -axis, the probability that it resides on z after time t is given by

$$P(z, t) = \frac{1}{\sqrt{4\pi Dt}} e^{-z^2/4Dt} \quad (2.16)$$

which is the Gaussian distribution with standard deviation $\sigma = \sqrt{2Dt}$ where D is the diffusion coefficient [21]. $P(z, t)$ can also be thought of as the density of water molecules at position z after time t , of water molecules that were on $z = 0$ on time $t = 0$. The MRI signal intensity is determined by the sum of all magnetic moments so we can write

$$S \propto \int P(z, t) \phi_G(z) dz = \frac{1}{\sqrt{4\pi Dt}} \int e^{-z^2/4Dt} e^{-2\pi i \gamma z G \delta} dz = e^{-\gamma^2 G^2 \delta^2 Dt} \quad (2.17)$$

where S is the signal intensity. If we assume that the dephasing and rephasing gradients can be considered instantaneous, in other words, that diffusion during gradient application is negligible, and call the time elapsed between the application of the dephasing and rephasing gradients τ , we have

$$S = c e^{-\gamma^2 G^2 \delta^2 D \tau} \quad (2.18)$$

where c is some constant that depends on a variety of parameters like spin density distribution, filtering effects etc. Notice that G, τ and δ are all parameters we set for the experiment and γ is the gyromagnetic ratio. The only unknowns in the equation are the constant c and the diffusion constant D that we are trying to estimate. This shows that D cannot be estimated by only one measurement. However, c can be estimated by taking a measurement without applying diffusion-weighting. If we call the signal intensity with no diffusion-weighting S_0 , we then have

$$S = S_0 e^{-\gamma^2 G^2 \delta^2 D \tau}. \quad (2.19)$$

It can be shown that under certain realistic gradients (non-instantaneous), e.g. the square-shaped gradient, the equation becomes (see [3] for details)

$$S = S_0 e^{-\gamma^2 G^2 \delta^2 (\tau - \delta/3) D} \quad (2.20)$$

which is the famous Stejskal-Tanner equation [22]. Letting

$$b = \gamma^2 G^2 \delta^2 (\tau - \delta/3) \quad (2.21)$$

yields

$$S = S_0 e^{-bD}. \quad (2.22)$$

This equation tells us that the diffusion coefficient cannot be estimated by signal intensity, but it can be estimated by the signal loss compared to another measurement. In practice, diffusion MRI datasets all include a “B0 image”. The name comes from $b = 0$ but it should be noted that $b = 0$ is impossible in practice so the “B0 image” is the image acquired with as little diffusion-weighting as possible. This image can be used for comparison with diffusion-weighted images to estimate D . The estimated D is called “apparent diffusion coefficient”, or shortly ADC, because the Brownian motion assumption does not hold in real biological tissue.

2.2.4.1 Diffusion Tensor Imaging(DTI)

Diffusion Tensor Imaging [23] is one of the first practical applications of DMRI in medical imaging and is still the most widely used method in the clinic. It is based on estimating an ellipsoid that represents the diffusion anisotropy of water at each voxel. The direction and length of the three axes define the ellipsoid, therefore only 6 parameters have to be estimated at each voxel. (2.22) is valid for 1D or isotropic diffusion. In 3D and assuming Gaussian but anisotropic diffusion, it can be written as

$$S = S_0 e^{-\sqrt{\mathbf{b}} \mathbf{D} \sqrt{\mathbf{b}}^T} \quad (2.23)$$

where \mathbf{D} , called the diffusion tensor, is a 3×3 symmetric tensor and $\sqrt{b} = \gamma \mathbf{G} \delta \sqrt{(\tau - \delta/3)}$ where \mathbf{G} is the gradient vector. The eigenvectors of \mathbf{D} and the corresponding eigenvalues,

$$\begin{pmatrix} D_{xx} & D_{xy} & D_{xz} \\ D_{yx} & D_{yy} & D_{yz} \\ D_{zx} & D_{zy} & D_{zz} \end{pmatrix} = \begin{pmatrix} v_1 & v_2 & v_3 \end{pmatrix}^T \begin{pmatrix} \lambda_1 & 0 & 0 \\ 0 & \lambda_2 & 0 \\ 0 & 0 & \lambda_3 \end{pmatrix} \begin{pmatrix} v_1 & v_2 & v_3 \end{pmatrix}, \quad (2.24)$$

define an ellipsoid that characterizes the anisotropy of diffusion. The equation has seven unknowns (one from S_0 and six from \mathbf{D}) and hence \mathbf{D} can be solved for if we have the B0 image and diffusion-weighted images acquired with 6 different gradient directions. In practice, data is taken with more gradient directions, usually 16, and a least squares fitting is used to estimate \mathbf{D} . This is done to reduce the effect of noise. After D is estimated, some quantitative measures that describe the anisotropy can be derived. The most popular measure is the fractional anisotropy:

$$FA = \sqrt{\frac{(\lambda_1 - \lambda_2)^2 + (\lambda_2 - \lambda_3)^2 + (\lambda_3 - \lambda_1)^2}{2(\lambda_1^2 + \lambda_2^2 + \lambda_3^2)}}. \quad (2.25)$$

FA takes a value between 0 and 1. When all the eigenvalues are equal, corresponding to isotropic diffusion, it is 0, and when one of the eigenvalues is much higher than the others, corresponding to diffusion restriction along the directions of the other eigenvectors, it is close 1. Hence, high FA is expected in voxels that contain a single fiber population with coherent direction and the principal eigenvector will coincide with the direction of the fiber.

The limitations of DTI are apparent from the tensor model. In addition to relying on a Gaussian diffusion assumption which is not true in biological tissue, it also cannot represent multiple fiber orientations in one voxel. With the image resolutions used in typical DTI experiments, a high percentage of voxels contain multiple fiber populations with different orientations. A recent study reported that multiple fiber populations can be detected in around 90% of WM voxels [24]. The limitations of DTI are very serious. Not only does DTI fail to estimate all the directions of multiple fiber populations within a voxel, it can fail to estimate the correct direction of any of them. For example, if there are two fiber tracts crossing perpendicular to each other within a voxel, DTI will estimate a disk-like ellipsoid, suggesting isotropic diffusion on the disk which is a complete misrepresentation

of reality. Despite its limitations, DTI is still the most widely used method in routine clinical scanning due to its short scanning time. When working with DTI data, one must be aware of its limitations and be extremely careful when conducting subsequent analysis.

2.2.4.2 Methods That Can Detect Multiple Fiber Populations In a Voxel

Due to the importance of DMRI as the only non-invasive method that can estimate WM orientation *in vivo*, a large number of improvements to DTI have been proposed to better estimate the orientation of fibers when multiple fiber pathways are present in one voxel. A more general representation of diffusion that removes the Gaussian assumption is the diffusion propagator $P(\mathbf{r}' - \mathbf{r}, \tau)$ which is the probability of a spin traveling from position \mathbf{r} to \mathbf{r}' in diffusion time τ . The diffusion propagator is related to the signal intensity as

$$S(\mathbf{k}, \mathbf{q}) = \int \rho(\mathbf{r}) e^{i2\pi\mathbf{k}\cdot\mathbf{r}} \int P(\mathbf{r}' - \mathbf{r}, \tau) e^{i2\pi\mathbf{q}\cdot(\mathbf{r}' - \mathbf{r})} d\mathbf{r}' d\mathbf{r}. \quad (2.26)$$

where $\mathbf{q} = \gamma\delta\mathbf{g}$ [25]. \mathbf{q} is called the diffusion wave-vector, γ is the gyromagnetic ratio, δ is the length of the gradient and \mathbf{g} is the gradient direction. An ensemble average of the conditional probability density function $P(\mathbf{r}' - \mathbf{r}, \tau)$ is called the ensemble average diffusion propagator (EAP). Similar to how the average spin density in a voxel could be recovered from the signal by sampling the k -space, the EAP can be recovered by sampling both the k -space and the q -space. This approach known as q -space imaging is thus in essence a 6D imaging method. This method that was initially used for inanimate material is not immediately applicable to medical imaging due to gradient field and scan time requirements. Applications to medical imaging are known as diffusion spectrum imaging (DSI) [26, 27]. DSI method is not practical for routine clinical scans because it uses multiple b-values that can go up to $17000s/mm^2$ and samples the q -space on a Cartesian grid, requiring a high amount of samples. As a result, DSI suffers from very long scan times that can exceed an hour.

A more clinically practical method based on q -space imaging is high angular resolution diffusion imaging (HARDI) that samples the q -space on a single shell on a sphere, that is, gradients are applied along a high number of uniformly distributed directions on a sphere using a single b-value [28]. Typical b-values for HARDI are in the $2000 - 5000s/mm^2$

range. HARDI data was initially used to estimate multi-tensor or higher-order tensor diffusion models [28, 29]. Model-free approaches were later developed. In q-ball imaging (QBI), a diffusion orientation distribution function (dODF or ODF) that represents only the angular structure of the EAP is reconstructed from HARDI data [30]. The EAP is formulated as $P(\mathbf{r})$ where \mathbf{r} refers to the relative displacement $\mathbf{r}' - \mathbf{r}$ in (2.26) and is called the diffusion probability distribution function (PDF) or shortly, the diffusion function. The ODF is defined as the radial projection of the diffusion function as:

$$\psi(\mathbf{u}) = \frac{1}{Z} \int_0^\infty P(r\mathbf{u})dr \quad (2.27)$$

where Z is a normalization constant. In generalized q-sampling imaging (GQI), the spin density function (SDF) which represents the quantitative distribution of the spins undergoing diffusion is estimated [31]. The spin density function is defined as

$$Q(\mathbf{r}, \mathbf{R}) = \rho(\mathbf{r})P(\mathbf{r}, \mathbf{R}) \quad (2.28)$$

where \mathbf{R} is the relative displacement $\mathbf{r}' - \mathbf{r}$ in (2.26). Normalizing the SDF yields the ODF. The SDF can be calculated from the diffusion weighted images $W(\mathbf{r}, \mathbf{q})$ using

$$Q(\mathbf{r}, \mathbf{R}) = \int W(\mathbf{r}, \mathbf{q}) \cos(2\pi\mathbf{q} \cdot \mathbf{R}) d\mathbf{q}. \quad (2.29)$$

The quantity of spins that undergo diffusion in a particular direction \mathbf{u} is then given by

$$\psi_Q(\mathbf{r}, \mathbf{u}) = \int_0^{L_\Delta} Q(\mathbf{r}, L\mathbf{u}) dL \quad (2.30)$$

$$= L_\Delta \int W(\mathbf{r}, \mathbf{q}) \text{sinc}(2\pi L_\Delta \mathbf{q} \cdot \mathbf{u}) d\mathbf{q} \quad (2.31)$$

where L_Δ is the diffusion sampling length and $\text{sinc}(x) = \sin(x)/x$ for all x except 0, and $\text{sinc}(0) = 1$.

The ODF and the orientation distribution of underlying fibers are of course closely related due to the diffusion being restricted by the fiber structure. However, it is important to remember that they are not the same. The peaks of the ODF are assumed to correspond to the orientations of fiber populations but this is not always the case. For two crossing fiber populations, it was shown that the peaks of the ODF correspond to the fiber orientations when the crossing angle is 90° , however the peaks of the ODF deviate

from true fiber orientations as the crossing angle of fibers becomes smaller [32]. Some methods attempt to directly estimate the fiber orientation distribution function (fODF) without estimating the ODF. One of the most popular approaches that directly estimate the fODF is known as spherical deconvolution [33, 34, 35]. The signal attenuation due to a single coherently oriented fiber population is represented by a response function $R(\theta)$ where θ is the elevation angle in spherical coordinates and the signal is assumed to be given by the sum of the response functions of all distinct fiber populations weighted by their respective volume fractions. Then the signal is written as $S(\theta, \phi) = F(\theta, \phi) \otimes R(\theta)$ where $F(\theta, \phi)$ is the fODF, ϕ is the azimuthal angle in spherical coordinates and \otimes is the convolution operator. $F(\theta, \phi)$ is then estimated by deconvolution of the signal using spherical harmonics.

2.2.4.3 Discussion on Tradeoffs Between Different DMRI Methods

As we have seen in the preceding section, there are a large variety of proposed improvements to DTI that aim to detect the orientation of multiple fiber populations in a voxel and it can be overwhelming to study all the different methods and decide which is best. There are however some principles that are true for any method and these principles can help guide the decision. First of all, the ability to detect multiple fiber populations increases with higher b-values and higher angular resolution. The reason is obvious for angular resolution and the reason for requiring high b-values is illustrated in Figure 2.15. The problem is, higher b-value means longer scan time and lower SNR because the echo will be weaker when we increase the wait time τ between the gradient pulses. Higher angular resolution requires longer scan time as well since gradients will have to be applied along more directions. Similarly, image resolution has a tradeoff with scan time. Longer scan time not only reduces the amount of patients that can be scanned per day, it also increases patient discomfort and may lead to lower image quality due to artifacts caused by patient motion. Hence, before deciding to use one method over another, one must think of what is being sacrificed. For example, if we fix the scan time and increase the b-value and angular resolution, we must reduce the image resolution so that the scan time remains the same. In addition, the SNR will be lower due to higher b-value. The tradeoffs need to

be carefully considered and the imaging method should be chosen based on the goals and requirements of the specific study. This is the main reason DTI is still the most widely used method in routine clinical scans despite its severe limitations. However, it can be expected that the advanced methods will become more common in routine clinical scans in the future as MRI machines improve.

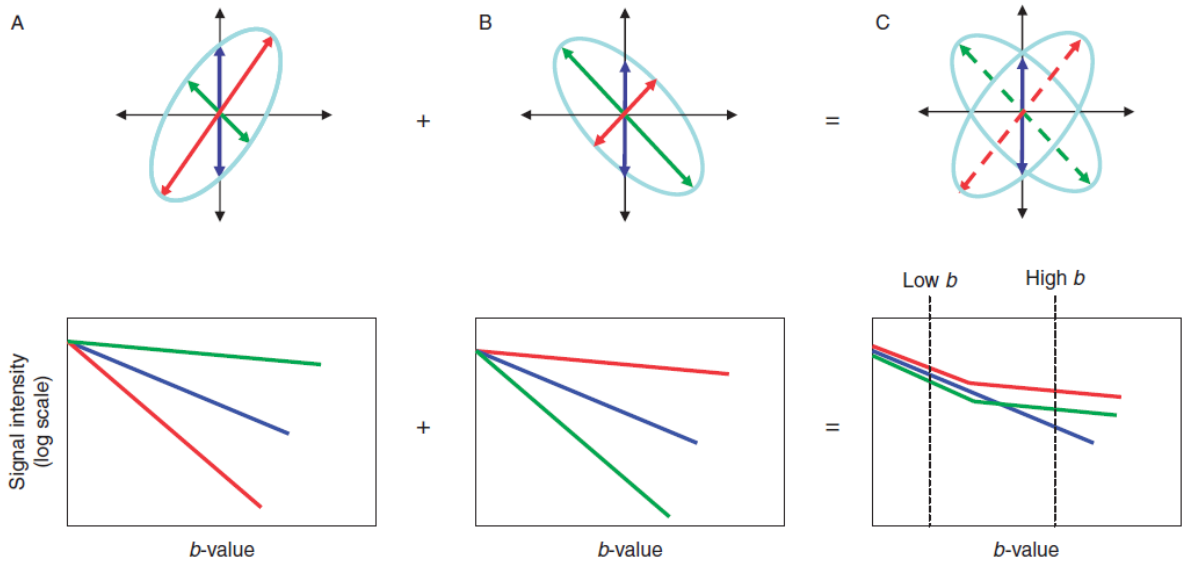


Figure 2.15: *Illustration on a hypothetical example of why high b-values are required to detect multiple fiber populations. (A) and (B) show two different fiber populations by themselves and the signal attenuation in 3 different gradient directions. (C) shows the situation when both of these fibers are present. The signal attenuation is now the sum of the attenuations caused by each fiber and as it is seen, it is not possible to distinguish the separate fiber populations from the signal for low b-values. Figure reproduced from [3] with permission.*

2.3 Image Registration

Image registration is the process of aligning two or more images that are not defined on the same space. This is a common situation in medical imaging because the images obtained from scans of different patients or different scans of the same patient are not aligned. Rigid registration refers to limiting the transformation between the different

coordinate systems to translation, rotation, scale and shear. Rigid-body transformation is defined by 12 parameters which are optimized to maximize/minimize a cost function. Let us denote two misaligned images as functions $I(\mathbf{x})$ and $J(\mathbf{y})$ where $I(\mathbf{x})$ is the image intensity of image 1 at point \mathbf{x} and similarly $J(\mathbf{y})$ is the image intensity of image 2 at point \mathbf{y} . The goal of rigid registration is to find a transformation \mathbf{T} that relates the positions in the two images as $\mathbf{y} = \mathbf{T}\mathbf{x}$, or more openly:

$$\begin{pmatrix} y_1 \\ y_2 \\ y_3 \\ 1 \end{pmatrix} = \begin{pmatrix} T_{11} & T_{12} & T_{13} & T_{14} \\ T_{21} & T_{22} & T_{23} & T_{24} \\ T_{31} & T_{32} & T_{33} & T_{34} \\ 0 & 0 & 0 & 1 \end{pmatrix} \begin{pmatrix} x_1 \\ x_2 \\ x_3 \\ 1 \end{pmatrix}. \quad (2.32)$$

Since we want the relation to be meaningful, some cost function based on the values $I(\mathbf{T}\mathbf{x})$ and $J(\mathbf{y})$ is maximized/minimized. If the imaging modalities are the same, a simple cost function such as sum square error can give satisfactory results but for different modalities, information theoretical cost functions such as mutual information or correlation ratio are used.

If the true transformation between image spaces is not rigid, then non-linear registration methods are utilized. Non-linear registration is an important area of study and research is ongoing to improve the methods. While sophisticated non-linear registration methods may improve the performance of certain types of fiber classification algorithms, the methods developed on this thesis do not rely on very accurate registration. Hence, rigid registration was used in all experiments in this thesis due to its simplicity and speed.

2.4 Tractography

Tractography is the process of reconstructing digital representations of white matter fiber pathways from DMRI data. The earliest and simplest form of tractography is deterministic streamline tractography based on DTI data [36, 37, 38, 39]. First, a seed region is selected either manually or automatically and seeds are randomly placed inside the seed region. From each seed, a tract is grown by following the principle (largest) eigenvector of the diffusion tensor (eq. 2.24) in both positive and negative direction until a set of

termination criteria are met. Some of the most common criteria are the angle between the previous and current step and the FA value. The growth of the tract is terminated when the angle is higher than a threshold, corresponding to an unrealistic tract trajectory or when FA is below a threshold, corresponding to low diffusion anisotropy according to the tensor model in the voxel. The output of streamline tractography is a set of tracts. Each tract is a set of ordered 3D points, hence a “streamline” that represents an approximation to the trajectory of a population of underlying fibers. For other models like ODF and fODF, deterministic streamline tractography can still be used in a similar manner. The tract is then grown in the direction where the ODF or fODF attain their highest value within a certain maximum angle threshold.

Since there is uncertainty regarding the estimated fiber orientations in any model, methods that randomly choose a path to follow based on a probability density function were also proposed [40, 41, 42, 39]. Compared to deterministic methods, probabilistic methods are better at following fibers through noisy or low anisotropy regions and regions that contain multiple fiber orientations. However, they are more prone to false positives, i.e. creating tracts that do not correspond to real fibers. The results of a deterministic and a probabilistic method are visualized in Figure 2.16. It should be noted that even the deterministic method results in a large number of false positive tracts. It is well established that this is a common problem with tractography [43]. Removal of spurious tracts and classification of tracts into anatomically meaningful pathways is the main topic of this thesis and will be discussed in detail in subsequent sections.

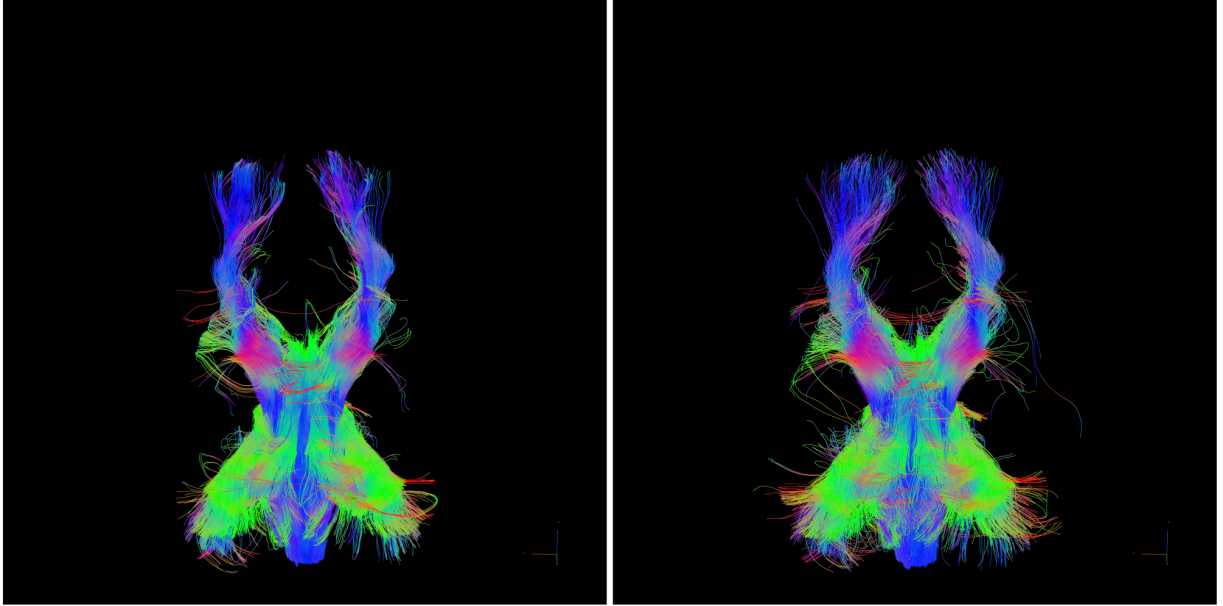


Figure 2.16: *Visualization of 10000 fiber tracts extracted by seeding the brainstem. Tracts are colored according to local orientation where superior-inferior direction is blue, left-right is red and anterior-posterior is green. Left: Result of a deterministic method. Right: Result of a probabilistic method.*

2.5 Literature Review of Fiber Clustering and Classification

Fiber clustering is the process of grouping “similar” fiber tracts together. The set of input tracts is the output of the tractography method. The similarity may be defined as geometrical, anatomical or a combination of both. Fiber classification entails labeling all tracts into known anatomical pathways that are defined by e.g. *in vitro* fiber dissection techniques [44]. Most of the methods in literature cluster the fibers first and then if needed, assign labels to the clusters for classification. Directly classifying individual tracts is an area that remains largely unexplored as there are only a few recent methods that use this approach.

Fiber clustering methods in literature can be generally classified into three main categories: (i) ROI (region of interest)-based; (ii) similarity-based; (iii) hybrid approaches

which combine (i) and (ii). ROI-based methods cluster or directly classify fibers according to the regions they pass or do not pass through. ROIs are selected based on known trajectories of major bundles of interest. Similarity-based methods rely on a similarity measure defined between fiber tracts or bundles. The measure can be geometrical, anatomical or both.

2.5.0.4 ROI-based methods

ROI-based methods can be further classified into two categories as manual or automatic. In manual methods, ROIs are interactively placed by a WM anatomy expert who can interpret images derived from diffusion MRI data [8, 45, 46, 47, 48, 49, 50, 51, 52, 17, 53]. Manual ROI approach is very popular due to few spurious tracts and guaranteed anatomically known clusters. The disadvantage is that manually selecting multiple ROIs (mROIs) is time consuming and subject to user expertise, bias, or error. Therefore, automation is a desired feature for the fiber clustering/labeling problem, while maintaining robustness of the automatic technique. Automatic ROI-based methods attempt to mimic the manual ROI placement by defining the ROIs on a template space and bringing the ROIs to the subject space using an estimated transformation between the template and subject spaces [54, 55, 56, 57, 58]. The disadvantage of this approach is that it relies heavily on the accuracy of template-subject registration. A further problem is that ideal placement of ROIs can vary between individuals, especially for pathological data, and this can lead to inaccurate clustering results. On the other hand, when there are no registration errors or pathology, clusters produced by automatic ROI methods are anatomically meaningful and contain few or no spurious fibers. Another advantage is that they are fast and their result can be used as initialization to more sophisticated methods, e.g. [59]. “The White Matter Query Language”, which was recently proposed in [60], enables a user to select tracts by using logical operations, anatomical terms and relative position terms. In essence, it is a semi-automatic ROI-based method. This method is also reliant on the accuracy of template-subject registration.

2.5.0.5 Similarity-based methods

Most similarity-based methods define a fiber (dis)similarity metric and use it within a known data clustering algorithm. The metric is usually chosen such that fibers that are geometrically close are put into the same bundle, hence this approach often emphasizes geometric properties of fibers instead of neuroanatomical knowledge. Some geometry-based metrics proposed in literature are fiber length and mean Euclidean distance [61], a measure based on distance between endpoints [62], Hausdorff distance, mean closest point distance [63, 64, 65], a dynamic time-warping-based distance [66], longest common subsequence [67], total square loss (with fibers modeled as Gaussian Mixture Models) [68]. Although most similarity metrics are geometric, neuroanatomy-based metrics have also been proposed [69, 59]. These techniques utilize clustering algorithms such as k -nearest neighbors clustering [61, 63], spectral clustering [62, 65], agglomerative hierarchical clustering [64], hierarchical total Bregman soft clustering [68], density-based clustering [66, 67] and expectation-maximization [59]. Lacking prior anatomical information, geometric or pure feature-based fiber clustering algorithms may produce artificially split or merged fiber clusters, which do not correspond to known anatomical bundles. In an alternative similarity-based approach, an atlas is created from clusters extracted with the manual ROI method and a similarity-to-atlas measure is used to cluster new subjects. The atlas can consist of sets of fiber tracts in the atlas space [70, 4] or be a probability map for each bundle of interest [71]. Similarity-based approaches utilizing an atlas have disadvantages similar to those of automatic ROI methods since both approaches rely on registration of an atlas to subject images. Recobundles [72], which also utilizes manually created bundle models, register the fibers instead of the images to reduce the errors from registration. While similarity-based methods are relatively more robust to registration errors and individual variability due to incorporation of a similarity-based score, they are more prone to spurious fibers because they are not as restrictive as ROI-based methods. Clustering normally requires computation of all pairwise distances but since this can be very computation intensive, either a random subset of streamlines or a faster clustering method such as QuickBundles [73] is used in practice.

2.5.0.6 Hybrid methods

Hybrid methods combine ROI-based and similarity-based approaches. [74] use automatic ROIs as a first step and then refine the resulting clusters with a geometric similarity-based method. [75] combine manual ROIs and a geometric similarity-based approach. The geometric similarity is used only for bundles that cannot be reliably separated by regions. [6] model fiber bundles as Gaussian processes and define a bundle-to-bundle geometric similarity measure. Agglomerative hierarchical clustering is then performed and anatomically meaningful clusters are selected from a dendrogram based on atlas ROIs. [76] use a multiple-step method that involves atlas-based ROIs, fiber-to-fiber and bundle-to-bundle geometric similarity measures with agglomerative hierarchical clustering. [77] first create multiple tract atlases by a manual ROI method, then for automatic clustering of new subjects, make an initial clustering based on automatic ROIs and finally refine further with a similarity-based label fusion approach making use of the multiple atlases. [78] presented a method for an atlas based fiber clustering as well as for setting up correspondences between subjects for population studies. A connectivity-based fiber representation is utilized in a Gaussian mixture model with an online training scheme.

In this thesis, we propose two different hybrid fiber classification methods that first constrain the input tract sets with loose ROIs, then cluster the remaining tracts and finally classify the clusters by comparison to manually reconstructed fiber models. The first method is designed for DTI and brainstem fibers and hence contains certain heuristics for that task. The second method is more general and utilizes a novel translation-invariant fiber representation called Neighborhood Resolved Fiber Orientation Distribution (NR-FOD).

2.5.0.7 Direct Supervised Classification of Individual Tracts

Methods that are based on supervised classification of individual fiber tracts, that is, methods based on learning a mapping from fiber features to class probabilities using a labeled training set of fibers, have started appearing in literature only very recently and this area remains largely unexplored. To our knowledge, there are only three published methods. In [79], the authors used heuristic geometric fiber features and a Viola-Jones

object detection framework to classify fibers into three classes of bundles. In [80] and [81], a convolutional neural network (CNN) based fiber classification scheme is proposed. However, the number of training subjects is only four and the method for creating the training set requires a significant amount of manual work and is highly subjective. It is also unclear how the test set was created.

In a different supervised approach, that can be called a direct volumetric segmentation of fiber bundles, the authors take tractography out of the process and train an encoder-decoder fully connected convolutional neural network (FCNN) to segment binary volume masks for each fiber tract of interest [82]. This method is very fast and volumetrically accurate compared to previous fiber clustering approaches but if streamlines representation of tracts is desired, additional steps are required to construct the fiber tracts. Using a similar network architecture, the authors later created tract orientation maps (TOM) for each bundle [83]. This approach is more suitable for constructing streamlines as the voxels now contain fiber-specific orientation information.

In this thesis, we propose a neural network based supervised classification method that utilizes the NRFOD representation. A practical training and validation dataset creation scheme is also proposed to reduce the human effort and bias in the creation of these sets.

Chapter 3

Automatic Labeling of Brainstem Fiber Pathways Using Anatomically-Constrained Density-Based Clustering¹

3.1 Materials and Methods

We describe the proposed automatic method that extracts and labels five major WM tracts that go through the human brainstem. Our approach is based on a density-based clustering technique, which is adapted to the fiber clustering problem. Here, we explain the details of the proposed brainstem fiber clustering method.

3.1.1 Dataset

Diffusion MRI (D-MRI) and corresponding datasets are obtained from two sources: (i) 20 unrelated subjects from Human Connectome Project (HCP)’s publicly available “WU-Minn 500 Subjects + MEG2 dataset” (<http://www.humanconnectome.org/documentation/S500/>). (ii) Yeditepe DATA: 3D T1 TFE (Turbo field echo) and DTI data acquisition of

¹The contents of this chapter were included in the project report of our TUBITAK Project No. 112E320.

10 subjects were performed on a 3T MR scanner (Philips Ingenia, Netherlands) with 16 channel head coil. 3D T1 TFE was acquired on a sagittal plane using a TR/TE 99/4.5ms, FA 8, TI 1000ms, image matrix 300x768, slice thickness 0.8mm, gap 0mm, acquisition time 6 minutes. DTI was acquired on axial plane, using TR/TE 3440/93ms, EPI factor 45, image matrix 90x128, slice thickness 2.5mm, gap 0mm. 16 diffusion directions at $b = 800\text{s/mm}^2$ were acquired in addition to $b = 0$ images (B0), acquisition time 7 minutes. This study was approved by the Ethics Review Committee of Yeditepe University Hospital (YUH).

3.1.2 Pre-processing and tractography

HCP preprocessed diffusion data is in NIFTI format and already eddy current corrected. For Yeditepe data, raw subject D-MRI images are in DICOM format and are first converted to NIFTI format using dcm2nii tool of mricron (<http://www.mccauslandcenter.sc.edu/mricron/mricron/>). Then, eddy current correction (only for YUH data), BET brain extraction and diffusion tensor estimation is performed in FSL (<http://fsl.fmrib.ox.ac.uk/fsl/fslwiki/>) to obtain a DTI volume. Initial tractography is performed with tensor deflection streamline method ([38]) using the following parameters: $f = 0.9$, $g = 0.7$, step size = 0.75mm, FA threshold = 0.15, max angle = 30, step size = 0.75mm, length constraint = 30 – 200mm. Seeding is done in the brainstem region which is obtained by an affine registration of Harvard-Oxford subcortical structural atlas (<http://fsl.fmrib.ox.ac.uk/fsl/fslwiki/Atlases>) to the subject’s B0 image. To account for the affine transformation between the MNI152 standard space [84, 85] and the B0 space, T1-weighted image of the subject is registered to the MNI152 structural template image (1mm) using FSL’s FLIRT tool. The output of the tractography step is a set of fibers where each individual fiber is a set of points in 3D space. Throughout the text, the terms fiber and tract are used interchangeably to refer to a single fiber curve, whereas a fiber bundle refers to a collection of fibers.

3.1.3 Clustering algorithm overview

An overview of proposed method is given as a flowchart in Figure 3.1. First, a tractography is performed seeding the whole brainstem region and the MCP is extracted by running the OPTICS algorithm on the set of fibers and then selecting the most similar cluster to the MCP mask. A reason to why only MCP is extracted in this first step is that its shape is very different from other fiber bundles in the brainstem, hence it leads to the most clear-cut labeling. Moreover, as the MCP is relatively large, it is highly likely that many of the fibers created by the tractography acquired by seeding the whole brainstem belong to MCP. Thus, the extracted cluster is expected to contain a sufficient number of fibers. Smaller bundles like the ICP on the other hand, may not be sufficiently represented in such whole brainstem fiber sets. Another significant advantage of extracting the MCP is that it is later used to aid in separation of the CST and the ML, which cannot be reliably extracted with a bundle-to-bundle similarity score like the one proposed here without additional constraints.

For extraction of the SCP and the ICP, manually defined ROIs/ROAs in the standard space are brought to the specific individual’s D-MRI space and tractography is performed using those as constraints. These ROIs/ROAs are chosen large enough to account for registration error and individual variability since false positives are expected to be removed later by similarity-based parts of the framework. Thus, two fiber sets, one for the ICP and one for the SCP, are created. These are then separately clustered by the OPTICS algorithm and clusters corresponding to ICP left, ICP right, SCP left and SCP right are selected by using the bundle-to-bundle similarity score against corresponding bundle masks. As a final step for the SCP, fibers extending to the sensorimotor cortex are removed using an ROA at internal capsule defined on the standard space.

Due to geometrical and spatial proximity of the CST and the ML, ROI constraints play a relatively more important role in their extraction. Defining a large ROI on the standard space would fail and a higher precision is required for their ROIs to be positioned correctly on the individual D-MRI data. In fact, these two bundles can only be reliably separated at the brainstem [14], and even there, the ROIs they are expected to pass through are spatially close. Fortunately, a neuroanatomical prior based on the MCP can aid in their

separation because at the pons level, the ML passes posterior to posterior pontocerebellar fibers while CST passes between the posterior and anterior pontocerebellar fibers. ROIs for the CST and the ML are located using an algorithm based on that prior information. In addition to these ROIs, automatically selected ROIs on medulla and sensorimotor cortex are also used to constrain tractography when extracting the CST and the ML. As a result, four sets of candidate fiber tracts for CST left, CST right, ML left and ML right are obtained, which are then separately clustered using the OPTICS, and the final bundles are extracted using the bundle-to-bundle similarity score as before.

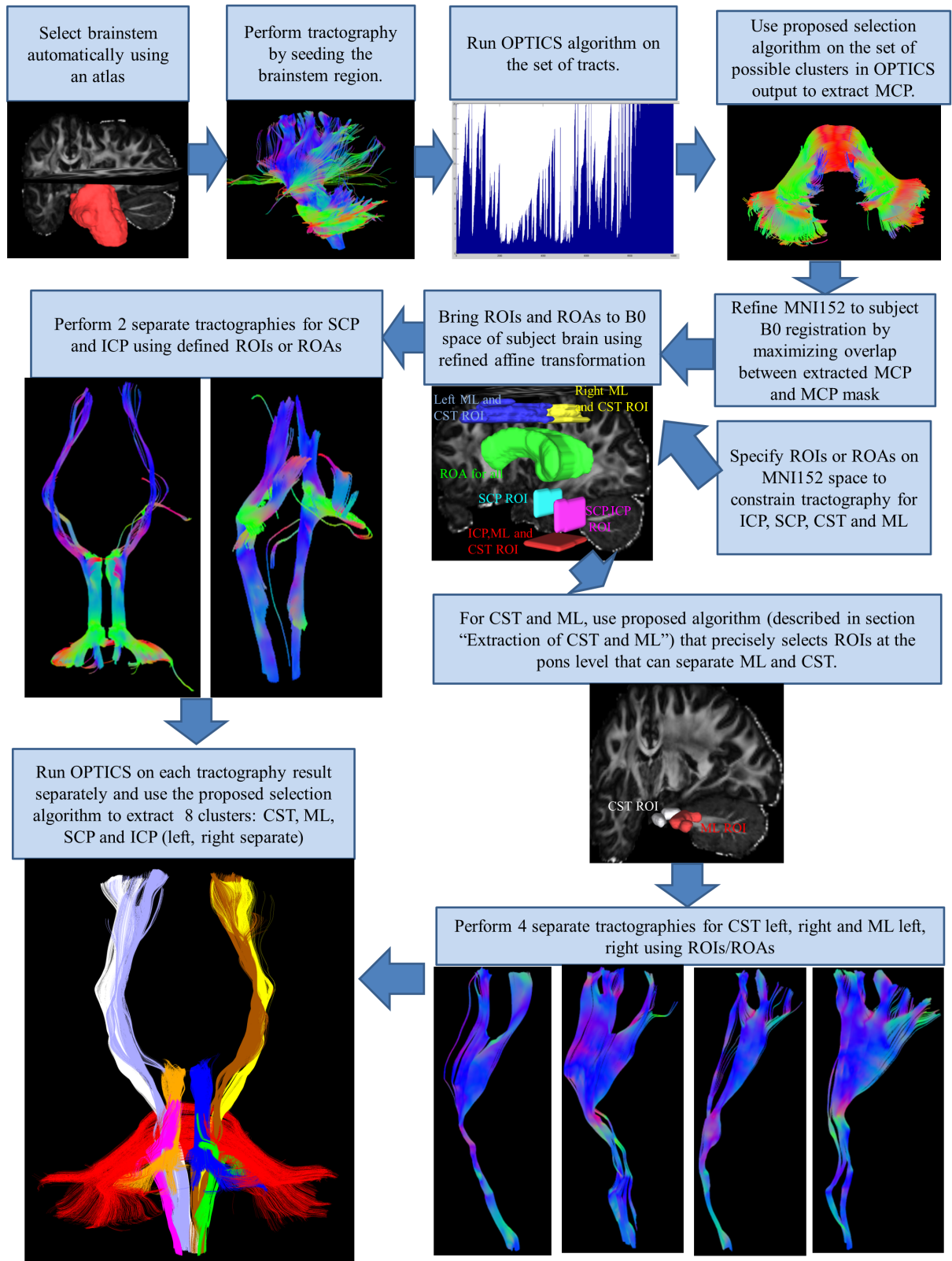


Figure 3.1: *Flowchart overview of the proposed brainstem fiber clustering framework.*

3.1.4 Fiber Bundle Mask Creation

Although there are already available WM atlases like e.g. ICBM-DTI-81 white-matter labels atlas (<http://fsl.fmrib.ox.ac.uk/fsl/fslwiki/Atlases>), they are not suitable for our proposed scheme because these atlases only label the bundles over voxels at which they are clearly separable from other bundles. However, in areas like the internal capsule where ML and CST are practically inseparable, no separate labels but a common label is used for them in the atlas. Thus, defining a similarity measure between possible bundles obtained from the OPTICS and bundle regions obtained from such atlases is not ideal. To overcome this problem, we created a bundle mask representing an “average bundle” in the standard space, which is a binary image, for each bundle of interest using clusters obtained with the manual ROI method of 10 brains over a training dataset. This is done by setting to non-zero all voxels for which the probability of the bundle passing through the voxel is greater or equal to 0.2. This way, a dissimilarity measure can be conveniently defined between a bundle mask and a possible bundle in order to select neuro-anatomically known bundles matching the output of the OPTICS algorithm according to a geometric bundle-to-bundle distance measure. For SCP, fibers extending to the cortex are included for creating the mask to aid in the selection algorithm to distinguish left SCP from right SCP. This is required because the courses of the left and right SCP are close and similar in shape in the midline over the midbrain level.

3.1.5 Dissimilarity measure between fibers

To use a geometric clustering approach, a fiber dissimilarity measure must be defined. We design a dissimilarity measure such that geometrically close fibers that have similar orientation give a small dissimilarity value. To formally define the proposed measure, let us first define a fiber as a set of 3D points: $A_i, i = 1, 2, \dots, N$ where N is the number of points that make up the fiber A . Let A and B be two fibers with number of points N and M respectively. The dissimilarity between A and B is calculated in 6 steps. For the sake of simplicity, let us assume $N \leq M$ (B is the longer fiber) and that $d(A_1, B_1) \leq d(A_1, B_M)$ where $d(A_i, B_j)$ denotes the Euclidean distance between i th point of A and j th point of

B . This assumption can be enforced by changing fiber names and/or point ordering so there is no loss of generality. Let us use the notation $A_i \leftrightarrow B_j$ to denote that the i^{th} point on A is matched with the j^{th} point of B . In the first step, the start and end points of B are matched to the closest point on A , that is, we find $i, j \in \{1, 2, \dots, N\}$ such that $d(A_i, B_1)$ and $d(A_j, B_M)$ are minimized and then set $A_i \leftrightarrow B_1$ and $A_j \leftrightarrow B_M$. In the second step, all points on A that come before i are matched to B_1 and all points that come after j are matched to B_M , that is, set $A_k \leftrightarrow B_1, k = 1, \dots, i - 1$ and $A_k \leftrightarrow B_M, k = j + 1, \dots, M$. The third step is simply long fiber to short fiber closest point matching, that is, $\forall k \in \{2, 3, \dots, M - 1\}$: find $A_l, l \in \{1, 2, \dots, N\}$ such that $d(A_l, B_k)$ is minimized and set $A_l \leftrightarrow B_k$. These first three steps are illustrated in Figure 3.2-a,b,c. In the fourth step, a preliminary dissimilarity between fibers A and B is calculated as follows:

$$D_{\text{spatial}}(A, B) = \frac{\sum_{i,j} d(A_i, B_j)}{K} \quad \text{s.t.} \quad A_i \leftrightarrow B_j, \\ i \in \{1, 2, \dots, N\}, j \in \{1, 2, \dots, M\}, \quad (3.1)$$

where K is the total number of matches. This simply takes the mean of Euclidean distances between all matching points found in the first three steps. The fifth step is the comparison of fiber orientation. First, the fibers are represented as a set of c vectors, obtained by uniformly sampling points on a fiber and drawing vectors between consecutive points. Fiber A is thus represented as

$$a_i = A_{k_{i+1}} - A_{k_i}, \quad k_{l+1} = 1 + \lfloor \frac{(N-1)l}{c} \rfloor, \quad l = 0, 1, \dots, c, \\ \lfloor \cdot \rfloor: \text{floor operation}, \quad i = 1, 2, \dots, N-1. \quad (3.2)$$

and fiber B is also similarly represented. This is illustrated in Figure 3.2-d for $c = 6$. Then, an orientation penalty term is calculated as follows:

$$\text{orientationPenalty}(A, B) = \frac{\sum_{i=1}^c p_i}{c}, \quad \text{where} \quad (3.3)$$

$$p_i = \frac{\gamma - 1}{1 + e^{-\frac{\cos\theta_i - \beta}{\alpha}}} + 1 \quad \text{and} \quad \cos\theta_i = \frac{a_i \cdot b_i}{\|a_i\| \|b_i\|}, \quad (3.4)$$

where γ, α and β are user-defined parameters. The idea is as follows. If the angle between corresponding directions are close to 0° , we should have $p_i \approx 1$ and if it is close to 180° ,

we should have $p_i \approx \gamma$. So basically, for each direction i , the range of $\cos\theta_i$ is mapped to the interval $[\gamma, 1]$ using a sigmoid function for smoothness. The final orientation penalty is calculated by taking the mean of penalties for each pair of corresponding directions. This term greatly helps in situations like shown in Figure 3.2-e,f, to make the defined measure regard orientational similarity in line with human perception. The sixth and final step just combines $D_{spatial}$ with the orientation penalty term to get the final dissimilarity measure as

$$D(A, B) = D_{spatial}(A, B) \times orientationPenalty(A, B). \quad (3.5)$$

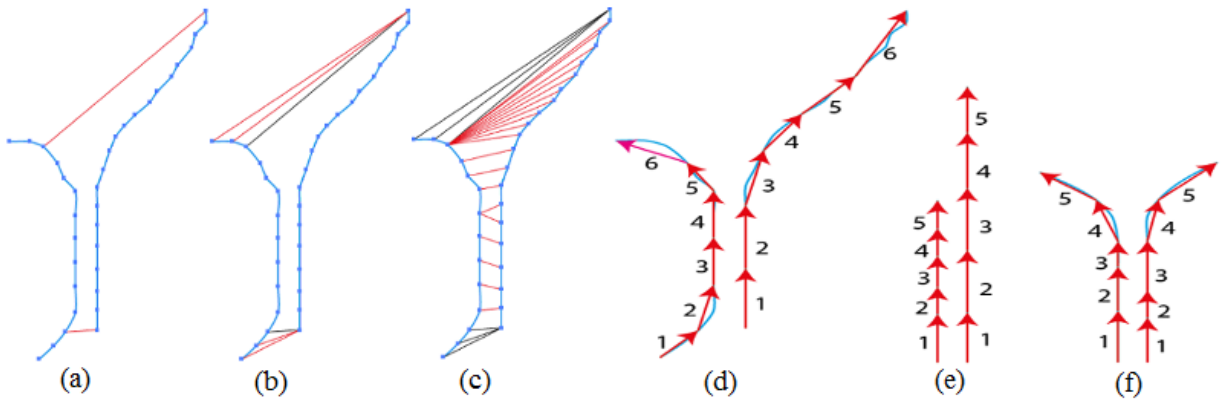


Figure 3.2: (a,b,c) An illustration of the three steps involved in matching points between two fibers in the definition of the fiber dissimilarity measure. (d) Representation of the same two fibers as sets of c vectors each ($c = 6$ here). (e,f) A toy example illustrating the advantage of the orientation term. Both tract pairs here would give small dissimilarity values with the mean closest point distance and the end point distance. With the addition of the orientation term, similarity of the fibers in (e) is higher than that of the fibers in (f). This is in agreement with human perception of fiber dissimilarity.

3.1.6 Geometry-based clustering algorithm

For geometry-based clustering, we use OPTICS [86], which is a density-based clustering algorithm that does not directly output a clustering but a specific ordering of the fibers from which possible clusters can be extracted. From here on, the distance between fibers refers to the proposed dissimilarity measure between them.

We will first briefly summarize OPTICS from a fiber clustering point of view in order to explain how our bundle-to-bundle similarity measure will make use of the OPTICS output. The OPTICS algorithm requires a set of fibers and two user-defined input parameters ϵ and $minFiber$. ϵ is chosen as the greatest expected intra-cluster distance and $minFiber$ indicates the minimum number of fibers required to form a fiber bundle. If we have a set of N fibers, the output of OPTICS is a list of N distances given in a specific ordering. The concepts of core-distance and reachability-distance are defined next.

Definition 1 *Let t be a fiber trajectory, represented as a 3D curve, uniformly sampled over its length. Let ϵ be a distance parameter, $N_\epsilon(t)$ the ϵ -neighborhood of t , $minFiber$ a positive integer and $minFiberDistance(t)$ the distance from t to its $minFiber^{th}$ neighbor (the neighbor that has the $minFiber^{th}$ smallest distance from t). Then the $coreDistance$ of t is defined as*

$$coreDistance(t) = \begin{cases} \infty & : |N_\epsilon(t)| < MinFiber \\ minFiberDistance(t) & : otherwise \end{cases}$$

where $|N_\epsilon(t)|$ denotes the number of fibers in the ϵ -neighborhood of fiber t .

Definition 2 *Let t_1 and t_2 be two fibers. Then, the $reachabilityDistance$ of t_2 with respect to t_1 is defined as*

$$reachabilityDistance(t_1, t_2) = \begin{cases} \infty & : |N_\epsilon(t_1)| < MinFiber \\ \max(coreDistance(t_1), distance(t_1, t_2)) & : otherwise \end{cases} \quad (3.6)$$

Let us denote the output of OPTICS as an ordered list $l = (d_1, d_2, \dots, d_N)$ where d_i is the distance associated with fiber t_i . This distance d_i is the smallest reachability distance from all predecessors of t_i , that is, t_1, t_2, \dots, t_{i-1} , to t_i . We refer the interested reader to [86] for further details of the OPTICS algorithm. To illustrate how the output of OPTICS reflects the clustering structure of fibers, we created an example fiber set by using the manual mROI method to pick 1000 fibers each from CST, SCP and MCP. A visualization of output list l and input fibers are given in Figure 3.3-a. Each valley in the visualization of l corresponds to a cluster. It can be noticed however that even in this simple example,

many different possible hierarchical clusterings exist due to smaller valleys inside larger valleys. Thus, an extraction scheme is required to extract clusters from l . The simplest way is to cut the graph with a horizontal line at some user-defined height y and take the created valleys as output clusters.

Although this could be quite useful in a few simple cases, it can be difficult, even impossible to choose a satisfactory y value in other cases as this scheme cannot capture clusters with varying density. This scheme is illustrated in Figure 3.3-b with $y = 10$ and Figure 3.3-c with $y = 2$ on the example fiber set. A more advanced scheme, which is capable of extracting clusters with varying densities is given in [86], which selects all possible clusters. In a typical dataset containing fibers passing through the brainstem, hundreds of clusters, which usually are not pairwise disjoint, are extracted. Thus, manually selecting neuro-anatomically meaningful clusters from this set of geometrically close fibers is impractical. On the other hand, having a set of all possible clusters instead of clusters that satisfy a user-defined criteria, as in cutting the graph with a horizontal line method, eliminates robustness issues and provides a richness of information. In order to take advantage of this in practice, an automatic algorithm for extracting meaningful clusters is required, which is explained next.

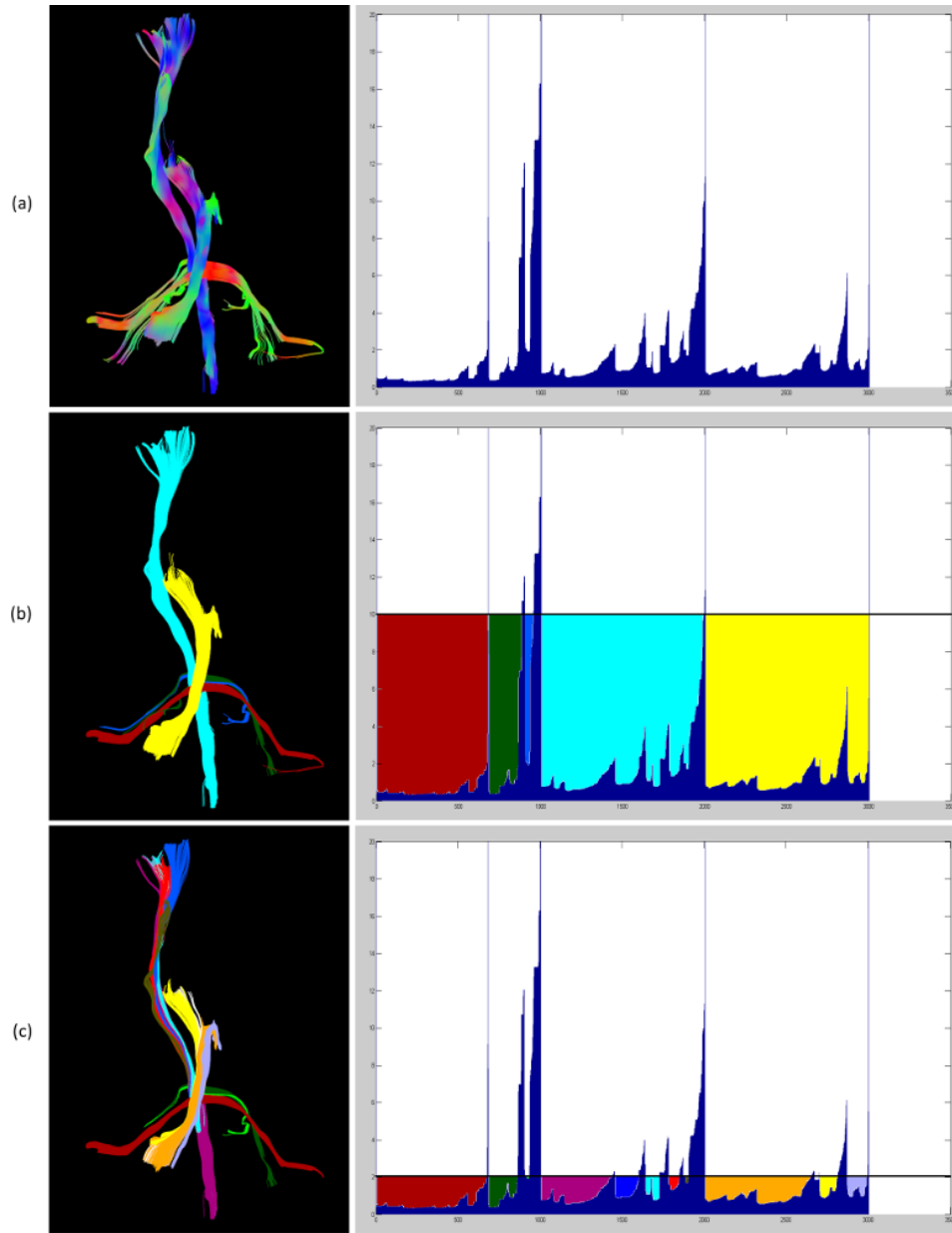


Figure 3.3: (a)-Left: Input fibers colored according to local diffusion direction. (a)-Right: OPTICS output: ordered reachability distances (y) versus fiber indices (x). (b)-Left: Fibers colored according to clustering done with horizontal line cut method with $y = 10$. (b)-Right: OPTICS output with colored areas corresponding to clusters in (b), indicated with the same color. (c)-Left: Fibers colored according to clustering done with horizontal line cut method with $y = 2$. (c)-Right: OPTICS output with colored areas corresponding to clusters in (c), indicated with the same color.

3.1.7 Cluster Selection from OPTICS output

In order to automatically extract anatomically meaningful clusters from OPTICS output, we define a bundle-to-bundle dissimilarity measure that compares a candidate bundle to a bundle mask, which is described previously. We use a symmetrized Chamfer distance between volumes corresponding to the bundles divided by the logarithm of the number of fibers in the candidate bundle. The weighting with the logarithm here is used as a “tie-breaker” to prefer clusters that contain more fibers as two bundles with a different number of fibers may have the same volume.

Simply selecting the candidate cluster that minimizes the bundle-to-bundle dissimilarity to the corresponding bundle mask usually works fine, however, fibers belonging to the same bundle may not always form a single cluster. For example, due to D-MRI limitations, FA values may be significantly reduced at voxels on the transverse fibers of the MCP. This leads the MCP to be fragmented, usually as two clusters, one in each hemisphere. In order to overcome this issue, ideally, instead of selecting one cluster, we would select a union of a subset of possible clusters that minimizes the dissimilarity measure. Finding the exact solution of this problem is unfortunately computationally intractable as the search space involves all possible subsets of all possible clusters extracted from OPTICS. Therefore, we use a simple greedy algorithm to make an approximately optimal selection as follows: The algorithm first finds the best two-element subset and then adds one more element at a time until the dissimilarity score cannot be reduced further.

3.1.8 Extraction of MCP

Extraction of MCP is straightforward as MCP is one of the largest bundles and its shape is quite distinct from nearby bundles. The brainstem region is already automatically selected (Section 3.1.2). By seeding the whole brainstem, the initial fiber set is obtained, on which the OPTICS algorithm is then run. The final MCP bundle is extracted by using the proposed selection algorithm (Section 3.1.7). The steps involved in the MCP extraction are illustrated in Figure 3.1: top row.

In cases where there is signal loss or noise in voxels that contain transverse fibers of the

MCP, the proposed algorithm can give even a better result than that of drawing manual ROIs on two hemispheres, as is usually done by an expert when extracting the MCP. Such an example is shown in Figure 3.4. This is thanks to the ability of the proposed algorithm to merge clusters creating a larger bundle that agrees with the bundle mask.

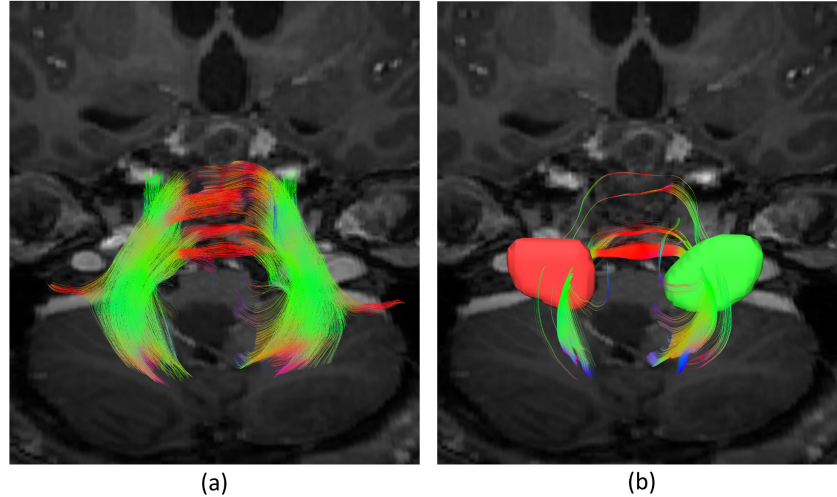


Figure 3.4: (a): MCP obtained with the proposed method. (b): MCP obtained with the mROI method. Green: Seed region. Red: ROI. It is seen that when the MCP is fragmented because of signal loss on D-MRI data, the proposed method gives better results than an mROI approach (using typical ROIs shown) for extracting MCP.

3.1.9 Extraction of SCP and ICP

ICP and SCP are extracted in a similar manner where for both of them, two ROIs are used for the initial tractography and no left-right discrimination is made. Extraction of SCP and ICP is illustrated in Figure 3.5. A coronal region in the cerebellum is used as one of the automatic ROIs for both bundles. For ICP, an axial ROI is automatically determined on medulla level and for SCP, a coronal ROI is automatically determined on thalamus. After the initial tractography, the OPTICS algorithm is run separately for both fiber sets and two clusters are chosen from each set according to the bundle-to-bundle similarity to match corresponding bundle masks to obtain the four desired clusters: SCP left, SCP right, ICP left and ICP right. As a final step for SCP, fibers extending to the cortex are removed using a loosely placed automatic ROA in the internal capsule (Figure 3.5 and

Figure 3.1).

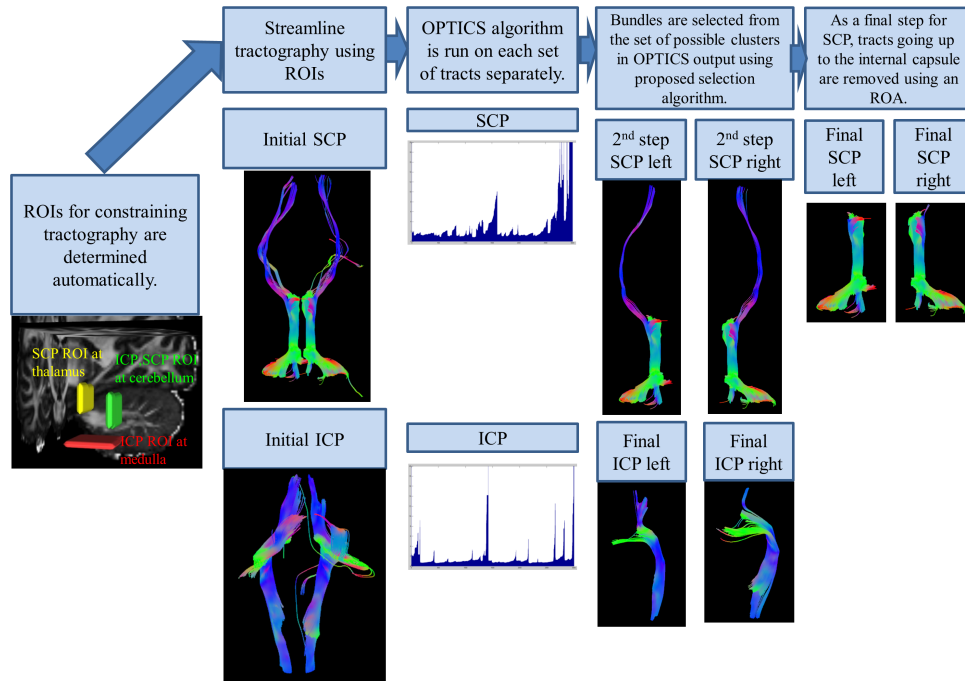


Figure 3.5: *Illustration of steps involved in extraction of the SCP and the ICP.*

3.1.10 Extraction of CST and ML

Extraction of the CST and the ML is the most difficult because these bundles have high shape similarity and spatial proximity. They are observed to be separable only at the brainstem level and indistinguishable at the supratheralamic level [14]. To tackle this difficult task, we design an algorithm for determining CST and ML ROIs at the pons level as follows: First, we specify five distinctive points (p_1, p_2, \dots, p_5) on an axial slice at the pons level on the MNI152 space. Figure 3.6 illustrates how these points define two rectangular ROIs for the CST and ML. It can be observed however that the separation of CST and ML ROI is quite sensitive to the position of p_2 and thus simply transforming the points defined on the standard space to the individual space is not adequate due to possible registration errors and individual variability. The ROIs specific to the individual brain should be obtained more precisely. To this end, the automatically extracted MCP and the DTI data of the subject are used.

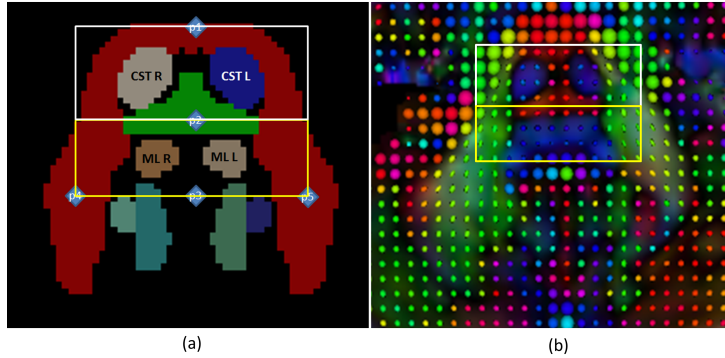


Figure 3.6: (a): Five points (p_1, \dots, p_5) manually chosen on an axial slice at the pons level on the standard space that define ROIs for CST and ML. Background image is JHU-ICBM-DTI-81 atlas colored according to labels. Red: MCP, Green: transverse pontine fibers (considered part of MCP) and ML and CST are annotated on the image (R: right, L: left). Other colors (SCP and ICP) are not relevant for CST, ML extraction. (b): An axial slice at the pons level from an individual brain with diffusion tensors visualized as ellipsoids illustrating how the rectangle ROIs defined in (a) would ideally look like on an individual brain.

Let us call an affine transformation matrix from the MNI152 space to the individual's B0 space T^a , let $q_i = T^a p_i$, and similarly define the corresponding rectangles in the B0 space using points q_i . Note that the rectangles on the MNI space may not lie on a single axial slice in B0. As a first step in refinement, we register the extracted MCP to the MCP mask and use the transform to reposition the points q_i . Even a pure translation model is adequate here as the MNI152 to B0 transformation already handles most of the rotation. Let us call the transformation matrix found in this second step T^b and let $T = T^b T^a$ and $r_i = T p_i$. These r_i 's are positioned better than q_i 's. The location of these ROIs are sensitive to only the anteroposterior axis, and the dominant fiber orientation in the neighbourhood of r_1 and r_2 on the coronal plane is mainly mediolateral. Based on that, the positions of r_1 and r_2 are further refined as follows: First, along each line over a set of mediolateral lines on the anteroposterior axis, number of voxels along the line in which the dominant diffusion direction is mediolateral is counted and recorded as the mediolateral diffusion dominance value. Then, the two lines, i.e. the most-anterior and the most-posterior lines, are chosen

such that their calculated mediolateral diffusion dominance values achieve a peak and is above a threshold relative to the highest mediolateral diffusion dominance value among all lines. The two selected lines ideally correspond to the posterior and anterior lines of the rectangle which contains the ROIs for the CST as depicted in Figure 3.6. Finally, using the two determined rectangles, the ROIs for the CST and the ML are selected as all voxels that are both in the corresponding rectangle and have superior-inferior dominant diffusion.

In addition to the ROIs at the pons level, two more ROIs, one on the sensorimotor cortex and one on the medulla are utilized. These are chosen on the standard space and brought to the individual space through registration. For those datasets, where the lower part of the CST or the ML from the pons to the medulla cannot be constructed with tractography due to noise and partial volume effects on the D-MRI volume, the ROI on the medulla is not used. The automatic algorithm detects such cases via a user-defined threshold on the ratio of the number of constructed fibers to number of seeds ($< 1\%$). Finally, the corpus callosum template is brought from the ICBM-DTI-81 white-matter labels atlas (<http://fsl.fmrib.ox.ac.uk/fsl/fslwiki/Atlases>) and dilated and used as an ROA to prevent crossing between hemispheres (depicted in Figure 3.1 and Figure 3.7). Using these constraints, four sets of fibers are constructed: each for CST left, CST right, ML left and ML right. Finally, the OPTICS algorithm is run separately on those fiber sets, and the final bundles are extracted using the proposed selection algorithm as described previously. Overview of the process of extracting the CST and the ML is illustrated in Figure 3.7.

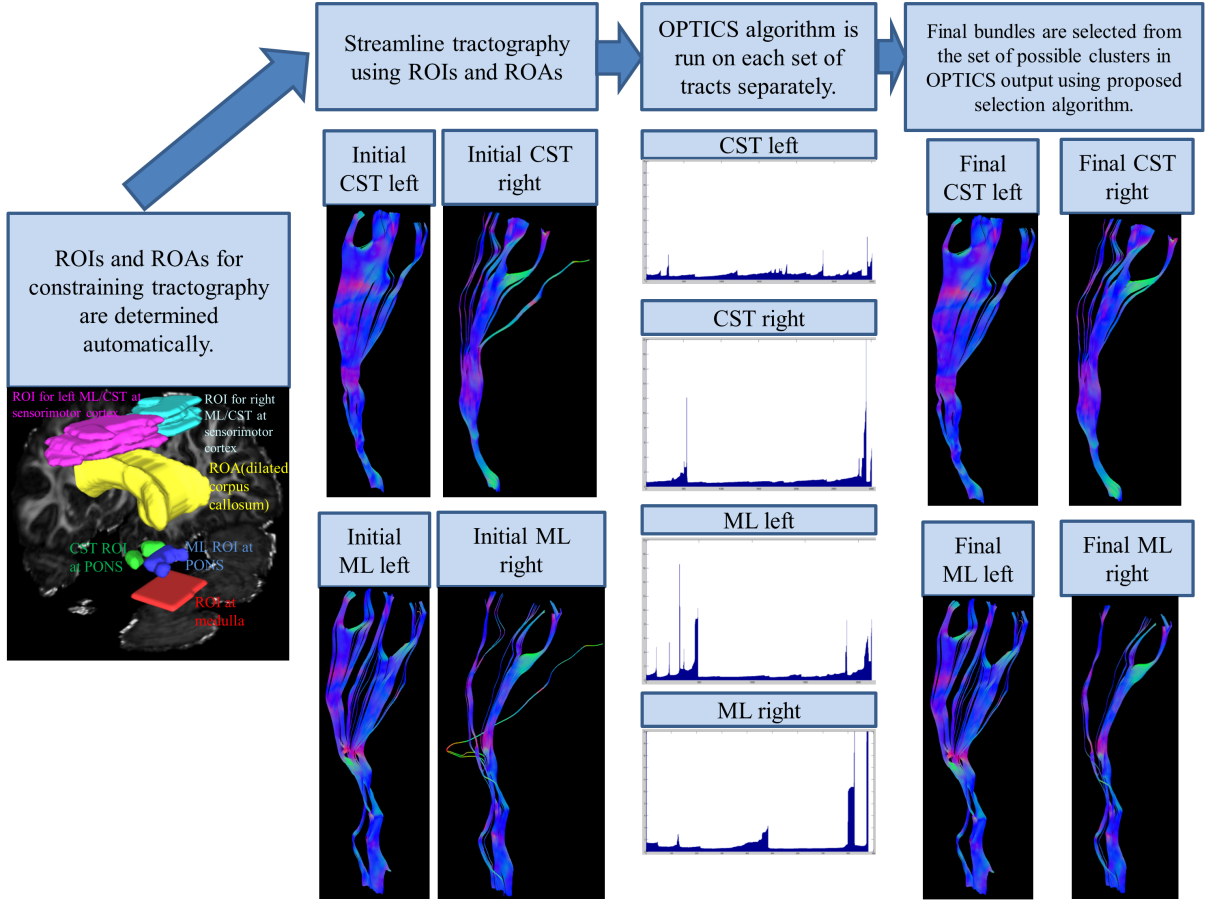


Figure 3.7: Illustration of steps involved in extraction of the CST and the ML.

3.2 Results

3.2.1 Implementation Details

Like other clustering techniques, a few number of important parameters has to be specified by the user to run the OPTICS algorithm. Throughout the experiments, we fix the *epsilon* and *minFiber* parameters to $\epsilon = 20, \text{minFiber} = 30$. The γ, α, β in the sigmoid function definition is fixed to $\gamma = 20, \alpha = -0.04, \beta = 0.9$. As the results are satisfactory for both the HCP dataset and the YUH dataset, we have not optimized the parameter selection, which can be done through an exhaustive parameter tuning, if desired. The YUH dataset was used in training (creating the bundle masks) and the HCP dataset was used in testing. Computation time was between 40 minutes and 70 minutes

on a desktop computer with AMD FX-8350 processor for the HCP data. The code was not optimized for performance.

3.2.2 Comparison of the Proposed Method to Manual ROI Method

We validate the proposed method by comparing it to the manual ROI method which is considered the most reliable but time-consuming approach. The bundles reconstructed by the two methods are compared quantitatively in terms of Cohen’s Kappa values and qualitatively by visual inspection of two expert raters (Rater 1: ZF- radiology specialist; Rater 2: UT - neurosurgeon). A visualization of all bundles created by both methods are given in Figure 3.8. Mean and standard deviation of Kappa values for each bundle are given in Table 3.1 and a visualization is given for each bundle when they achieve their best and worst Kappa scores in Figure 3.9. Mean and standard deviation of qualitative scores given by experts after visual inspection are given in Table 3.2.

We performed Wilcoxon signed-rank test on the visual scores to test for statistical significance between means of manual and automatic results for each bundle and the results are given in Table 3.3. At 1% significance level, there is no statistical evidence to reject the null hypothesis, i.e. to suggest that the means are different for manual and automatic results of all bundles for both raters. At 5% significance level, this is also valid for 14 out of 18 bundle evaluation experiments. For the left SCP and MCP (Rater 1) and the left and right SCP (Rater 2), manual ROI results were rated higher than results of the proposed method.

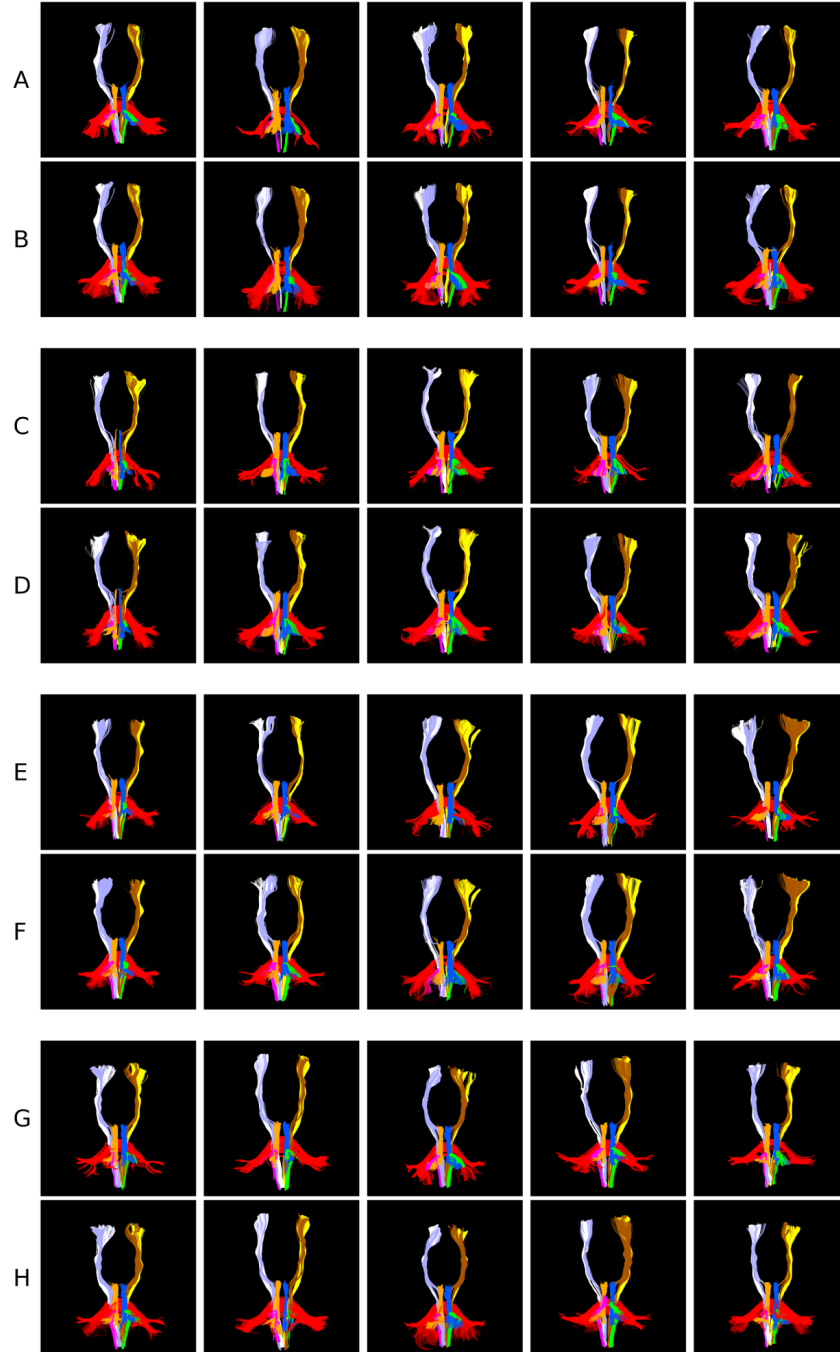


Figure 3.8: *Visualization of clustering results for all 20 test subjects. A: Manual ROI method for subjects 1-5; B: Proposed method for subjects 1-5; C: Manual ROI method for subjects 6-10; D: Proposed method for subjects 6-10; E: Manual ROI method for subjects 11-15; F: Proposed method for subjects 11-15; G: Manual ROI method for subjects 16-20; H: Proposed method for subjects 16-20.*

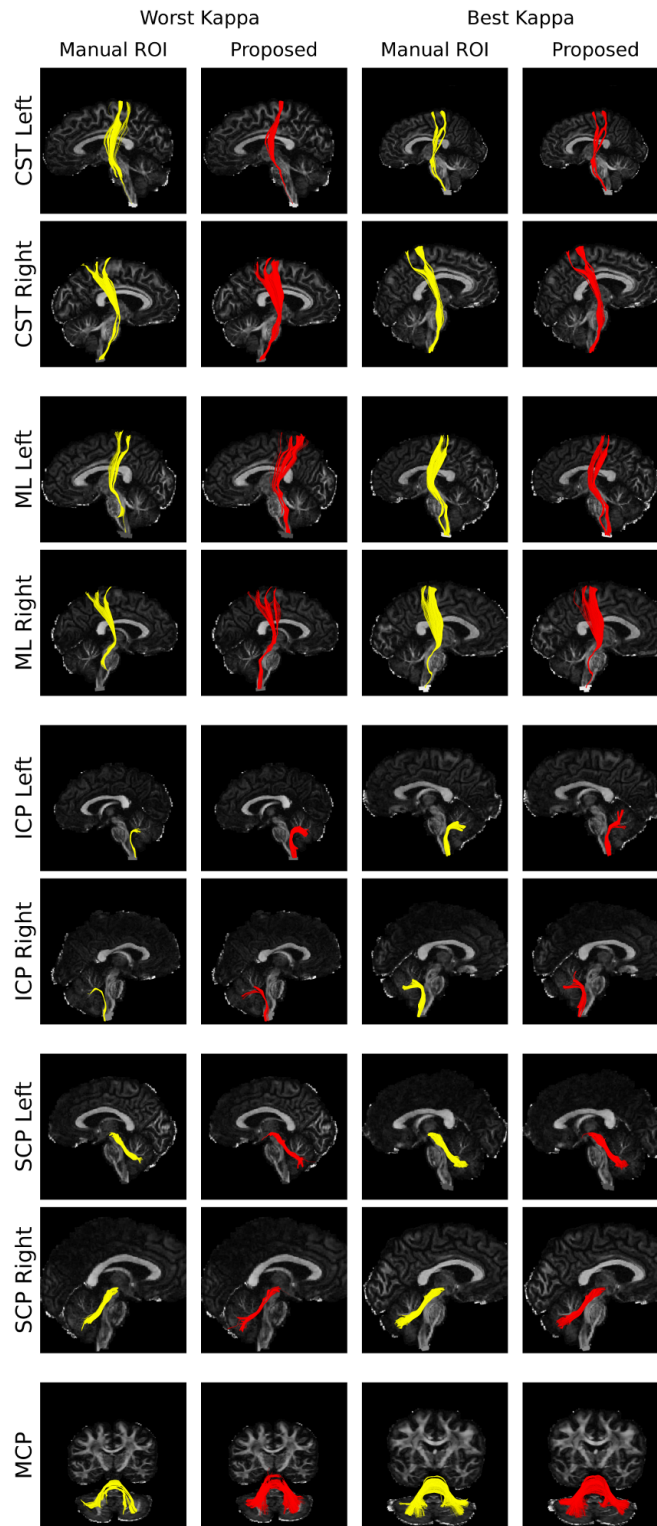


Figure 3.9: Visualization of bundles created with the manual ROI method vs. the proposed method for best and worst Kappa scores achieved among the 20 test subjects.

Table 3.1: Mean and standard deviation of Cohen’s Kappa values between bundles reconstructed by the manual ROI method and the proposed method.

	CST_L	CST_R	ML_L	ML_R	ICP_L	ICP_R	SCP_L	SCP_R	MCP
Kappa	0.85 ± 0.11	0.86 ± 0.10	0.74 ± 0.14	0.77 ± 0.12	0.55 ± 0.14	0.60 ± 0.18	0.79 ± 0.10	0.79 ± 0.10	0.62 ± 0.10

Table 3.2: Visual scoring by two experts. Score is given based on how well the reconstructed bundle agrees with known neuroanatomy. 1: Very poor; 2: Poor; 3: Mediocre; 4: Good; 5: Very good. R1 refers to Rater 1; R2: Rater 2; M: Bundle reconstructed with the manual ROI method; A: Bundle reconstructed with the proposed automatic method.

	CST_L	CST_R	ML_L	ML_R	ICP_L	ICP_R	SCP_L	SCP_R	MCP
R1_M	4.45 ± 0.51	4.30 ± 0.57	3.50 ± 0.51	3.45 ± 0.60	4.05 ± 0.69	4.15 ± 0.75	4.25 ± 0.72	4.25 ± 0.72	4.30 ± 0.80
R1_A	4.40 ± 0.50	4.25 ± 0.79	3.45 ± 0.69	3.45 ± 0.60	3.65 ± 0.67	3.75 ± 0.72	3.75 ± 0.64	3.80 ± 0.70	4.05 ± 0.76
R2_M	4.20 ± 0.62	4.20 ± 0.77	3.55 ± 0.60	3.50 ± 0.69	3.75 ± 0.44	3.85 ± 0.37	3.80 ± 0.52	3.80 ± 0.52	4.05 ± 0.60
R2_A	4.30 ± 0.57	4.10 ± 0.79	3.35 ± 0.59	3.45 ± 0.60	3.60 ± 0.68	3.90 ± 0.45	3.50 ± 0.51	3.60 ± 0.60	3.55 ± 0.60

Table 3.3: p-values for Wilcoxon signed-rank test on the visual scores for difference of means between manual and automatic results for each bundle.

	CST_L	CST_R	ML_L	ML_R	ICP_L	ICP_R	SCP_L	SCP_R	MCP
Rater 1 p-values	0.5000	0.6250	0.2891	1.0000	0.5488	1.0000	0.0313	0.3594	0.0107
Rater 2 p-values	1.0000	1.0000	1.0000	1.0000	0.0869	0.0723	0.0107	0.0156	0.2734

3.3 Discussion and Conclusion

The proposed method makes use of both similarity-based and ROI-based clustering to minimize the disadvantages of these two approaches. It is more robust to registration errors and individual variability compared to pure automatic ROI methods because larger template ROIs can be used as the subsequent similarity-based part of the method is expected to remove spurious fibers. Further, the proposed method contains fewer spurious fibers compared to pure similarity-based methods due to its use of ROI constraints to eliminate fibers that are too far from expected bundle trajectories. Finally, as with any automatic method, it eliminates the user bias and required human effort that plagues manual ROI methods. The quality of resulting bundles is usually comparable to that of manual ROI method. Despite being designed specifically for clustering brainstem bundles, the framework can be generalized to full-brain clustering albeit with some effort.

An important limitation of the proposed method is that automatic selection of the ROIs on the pons level for the CST and the ML may fail to give satisfactory results in pathological or noisy data. Such conditions can be checked from the implausible ROIs produced by the algorithm and corrected manually or can be considered for further development.

As with any clustering algorithm, the accuracy of the proposed method is heavily influenced by the tractography method as well as the resolution and quality of the DTI image. Thus, the limitations associated with DTI and the chosen tractography method will apply. Multiple fiber populations within a voxel is a tricky issue in processing Diffusion MRI data. Recently proposed high angular resolution diffusion MR approaches such as HARDI [28], QBI [30], spherical deconvolution [33], and DSI [28, 27] create multi-peak fiber orientation distributions to enable representation of underlying multiple fiber populations in a voxel. Advanced imaging systems and protocols as those in the latest brain research initiative Human Connectome Project (HCP) provide high-resolution diffusion MRI data, but those systems are not yet available in routine clinical practice. DTI is still the common choice for clinical scanning routine in hospitals due to demanding acquisition times and complex computations required for the high-resolution diffusion MRI. Since in

this study, we mainly aimed to ease the routine clinical medical image processing workflow by providing the expert with subject-specific fiber clusters of the five main bundles in the brainstem at an acceptable quality, the experiments were done only on DTI. It should be noted that the proposed method is largely independent of the diffusion MRI method. The only part that is dependent on DTI is the selection of the ROIs for the CST and the ML at pons level regarding dominant fiber orientations. This part can be naturally adapted to other types of diffusion MR images. Similarly, the proposed method is not dependent on a specific tractography method, it only requires that the output of the tractography method is a set of fibers, each fiber defined as a set of points. Thus, in the future, more advanced diffusion MR techniques and tractography methods can be utilized as desired.

Although the SCP, the ML, and the CST decussate at midbrain and medulla, respectively, majority of fibers in the reconstructed trajectories are constrained to the same hemisphere due to the nature of fiber reconstruction and tracking techniques. This limitation causes physically crossing fibers to produce kissing fiber trajectories as also pointed out by [9]. At the pons level, both the MCP and the CST frequently occupy the same set of voxels. This can lead the CST to fail to reach the medulla or to follow the MCP. Similarly, some MCP fibers may fail to cross to the other hemisphere or follow the CST to the cortex. At the internal capsule level, the ML and the CST are not distinguishable on DTI data. Hence the thalamocortical continuation of those bundles, particularly the ones projecting to the primary somatosensory cortex which are thought to be associated with both the CST and the ML, may in reality belong to either of them.

To conclude, the proposed brainstem fiber clustering technique automates the process of construction and labeling of subject-specific major brainstem white matter pathways, hence relieves the operators from that tedious manual task. To our knowledge, this is the first study that presents such a solution customized to the brainstem. The designed fiber dissimilarity measure and the neuroanatomical knowledge-based ROI placements coupled with a density-based clustering scheme are shown to work comparable to the manual ROI method through both quantitative scores and qualitative expert scores against the latter. Therefore, the proposed method is expected to be of use in planning of brainstem surgery as well as analysis of white matter fibers related to brainstem. Furthermore, after addition of

a step to set up correspondences among fiber bundles of different subjects, it can facilitate various population-based connectivity studies on neurological and developmental diseases that relate to the structural organization of fiber pathways traversing the brainstem.

Chapter 4

Neighborhood Resolved Fiber Orientation Distributions (NRFOD) in Automatic Labeling of White Matter Fiber Pathways²

4.1 Materials and Methods

An overview of the proposed method is illustrated for left projection fibers (CST and ML) in Figure 4.1. Similar steps are used for all bundles of interest. We use fiber and tract interchangeably to refer to a single 3D curve representing a fiber, whereas a bundle refers to a collection of fibers.

²This chapter appeared as a journal article in *Medical Image Analysis, Volume 46, pages 130-145, May, 2018*. The introduction section of the journal article is not repeated here because a more detailed background is given in Chapter 2.

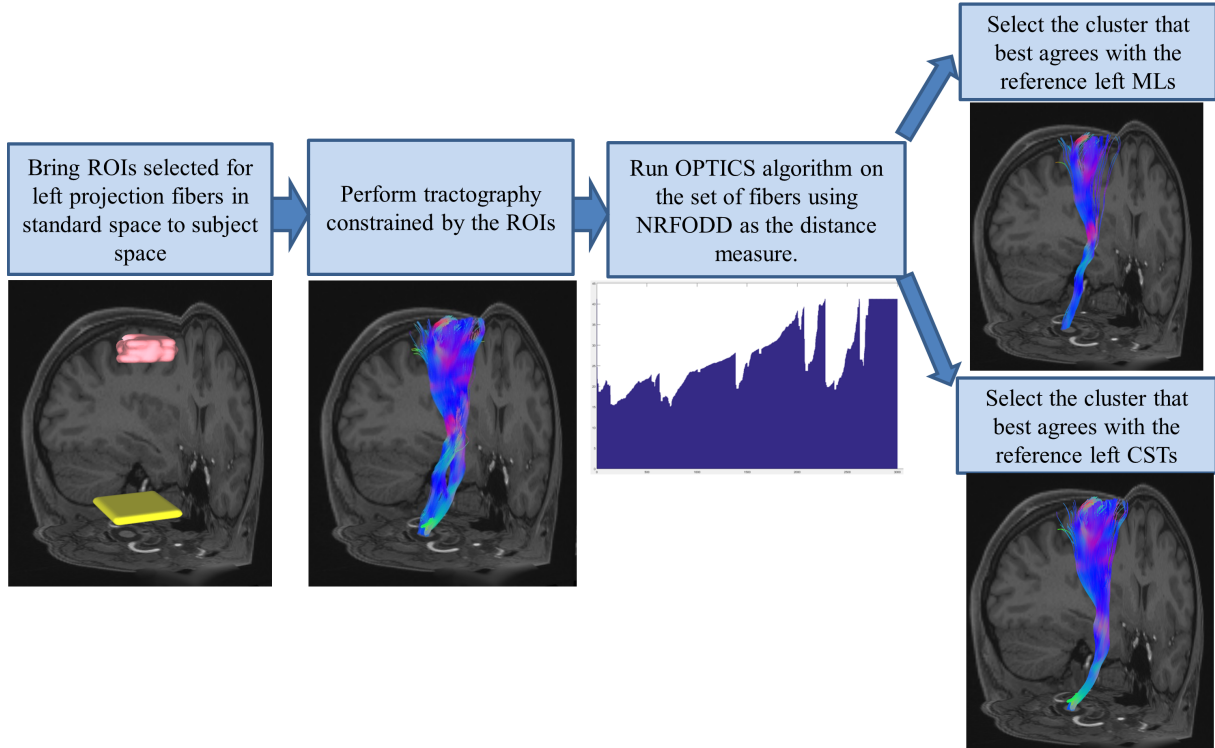


Figure 4.1: *Illustration of the proposed method on the left CST and ML bundles.*

4.1.1 Dataset

Diffusion MRI (D-MRI) and corresponding datasets are obtained from 30 unrelated subjects from Human Connectome Project (HCP)’s publicly available “WU-Minn 500 Subjects + MEG2 dataset” (<http://www.humanconnectome.org/documentation/S500/>). Due to significant time requirements for manual clustering which is needed for quantitative evaluation of the proposed method, 30 subjects are included from the dataset.

4.1.2 Reconstruction of Orientation Distribution Functions

Generalized q-sampling imaging (GQI) method, which has the practical advantage of being able to reconstruct ODFs from a large variety of diffusion MRI datasets including multi-shell data, is used coupled with an ODF decomposition method [87] to resolve at most three fiber orientations per voxel. A diffusion anisotropy value (QA) [31] that quantifies the spin population in each resolved orientation is also obtained. The reconstruction

is performed by DSISudio (<http://dsi-studio.labsolver.org>).

4.1.3 Manual ROI Selection on Standard Space

If a whole brain tractography output was used as input to the density-based clustering algorithm, majority of the fibers in the input set would not correspond to any of the bundles we are interested in. Thus, in order to reduce computation time and increase the likelihood that a sufficient number of fibers are reconstructed for each bundle of interest, the initial fiber sets passed to the density-based clustering algorithm are constrained by ROIs that are selected on the standard MNI152 space [84, 85] and transformed to the subject space. The transformation is assumed to be affine and the transformation matrix is obtained by registering the subject T1 image to the MNI152 T1 image. It is important to emphasize that the ROIs are not meant to obtain a good clustering by themselves, their main purpose is to reduce the number of fibers passed to the density-based clustering algorithm. The ROIs are thus selected large enough to account for registration errors, individual variability and possible pathologies. We have defined ROIs for the following sets of fibers: left projection fibers (left CST and ML), right projection fibers (right CST and ML), SCP, ICP and MCP (Figure 4.2).

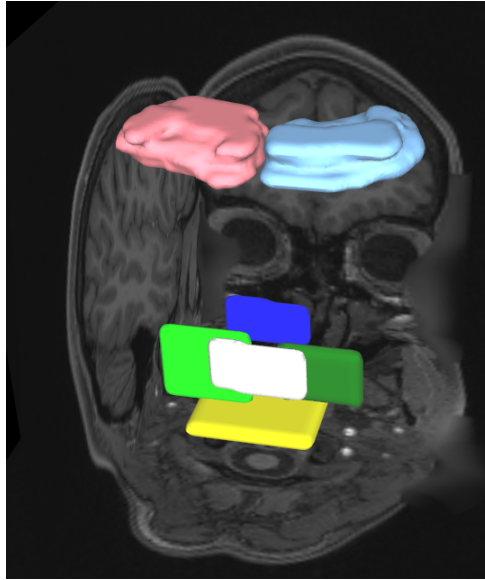


Figure 4.2: *The ROIs defined on the standard MNI space to constrain initial fiber sets that will be passed to the density-based clustering algorithm. Yellow: Axial ROI on medulla for left, right projection fibers and ICP; Pink: ROI on left sensorimotor cortex for left projection fibers; Teal: ROI on right sensorimotor cortex for right projection fibers; White: Coronal ROI on cerebellum for ICP and SCP; Green: Coronal ROI on cerebellum on the left hemisphere for MCP; Dark Green: Coronal ROI on cerebellum on the right hemisphere for MCP; Blue: Coronal ROI near thalamus for ICP and SCP. Note that the ROIs are selected very large to account for individual variability and possible registration error.*

4.1.4 Tractography

A simple probabilistic streamline tractography algorithm is implemented to construct the initial fiber sets that will be utilized by the density-based clustering step. The ROIs defined on the standard space in the previous step are brought to the subject space using an affine registration and the tractography algorithm starts from randomly generated seed points inside one of these ROIs and grows a fiber as follows: First, a direction is randomly selected from the set of resolved fiber orientations present in voxels closest to the current point. The chance of a direction being selected depends on its corresponding QA value, the distance of current point on the fiber to the voxel center and the angle between the previous direction taken by the fiber and the current candidate direction (details are given

in 4.A). Once a direction is chosen, a step of $stepSize = 0.75$ millimeters is taken in that direction. The process terminates when the fiber is out of image bounds or there is no possible direction whose angle with the previous direction chosen by the fiber is less than $maxAngle = 20$ degrees and its QA value is larger than $minQA = 2$. This fiber generation process is repeated until a desired number of fibers are constructed that pass through all the ROIs and have length between $minLength = 30$ mm and $maxLength = 200$ mm. The tractography parameters are empirically set.

We construct five initial fiber sets for the brainstem: left projection fibers (left CST and ML), right projection fibers (right CST and ML), SCP, ICP and MCP. We note that the tractography step can be carried out by any other method existing in current tools such as DSISstudio.

4.1.5 Neighborhood Resolved Fiber Orientation Distribution (NRFOD) of a Fiber and the Fiber-to-fiber Distance Measure (NRFODD)

For clustering a collection of fibers, first a fiber representation should be selected. We define a descriptive fiber representation, NRFOD, which relies on the distribution of orientations of fibers in the neighborhood of a given fiber. Next, based on the NRFOD, we utilize a fiber-to-fiber distance measure that is independent of Euclidean distances between points on a fiber, thanks to the new fiber representation. Let us first describe and motivate our novel fiber representation that will allow such a measure to be defined between fibers.

Using GQI with a subsequent diffusion decomposition method [87], the resulting image is a set of voxels in 3D space where each voxel contains a set of resolved fiber orientations and corresponding quantitative anisotropy (QA) values that represent the spin population in the corresponding orientation [31, 87]. In order to segment bundles from such an image, neuroanatomy experts typically rely on slices of the volume on which resolved fiber orientations are visualized with lines colored and oriented according to their voxel-wise diffusion orientation or in the case of DTI, FA maps colored according to the principal

direction of the diffusion tensor. An example axial slice at the pons level is illustrated in Figure 4.3. The human approach to identifying the area of for instance the left CST bundle on such a slice is as follows: in the neighborhood of the left CST, mostly green lines (or colors) are expected to the left; similarly mostly reds (lines) are above and below, and mostly blue and some reds to the right. The NRFOD representation is an attempt at mathematically capturing this human approach in 3-dimensions where a fiber is distinguished by the resolved fiber orientation distributions in the neighborhoods of points sampled on the fiber. The fiber-to-fiber distance measure based on the NRFOD, which we will call NRFODD, is then based on the intuition that the aggregated similarity of distributions of white matter fiber orientations in the neighbourhood of all points on two fibers should be large in order to cluster those fibers together.

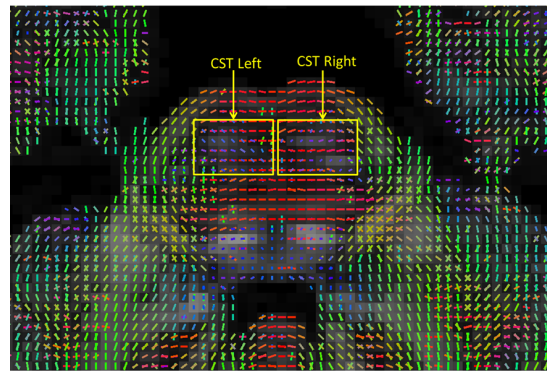


Figure 4.3: *An axial slice of a GQI image at the pons level. Each resolved orientation on a pixel is represented by a line color-coded according to the resolved orientation where red is left-right , green is anterior-posterior and blue is inferior-superior orientation.*

Formally, let $T = \{t_1, t_2, \dots, t_K\}$ be a fiber where K is the number of points that define the fiber. A NRFOD is a set of $M \times K$ histograms that represent the distribution of resolved fiber orientations around each point t_k of the fiber for M probing directions. Each histogram is defined to contain N bins, each bin representing an orientation, and the count in each bin is determined by the number of resolved fiber orientations that fall into a certain bin, in a cylinder along the probing direction (see Figure 4.4). We aim to probe a roughly spherical region around each point t_k , hence the M probing directions are chosen using a spherical covering with M points. The spherical coverings were calculated

by [88]. Cylinders were selected as probing regions for simplicity. Other probing shapes could have been used to a similar effect, e.g. rectangular prisms or cones. N may be smaller than the number of sampling directions used in the GQI scheme in which case a resolved fiber orientation is simply assigned to the bin that minimizes the angle between the fiber orientation and the orientation represented by a histogram bin. Similarly, M need not be the same as the number of sampling directions of the GQI scheme. In fact, we recommend choosing M and N smaller than the number of sampling directions of the GQI scheme in order to reduce computational load and the impact of noise in fiber orientations. Finally, we obtain a $K \times M \times N$ -dimensional representation of each fiber, which includes a probing of local neighborhood diffusion profiles around the fiber.

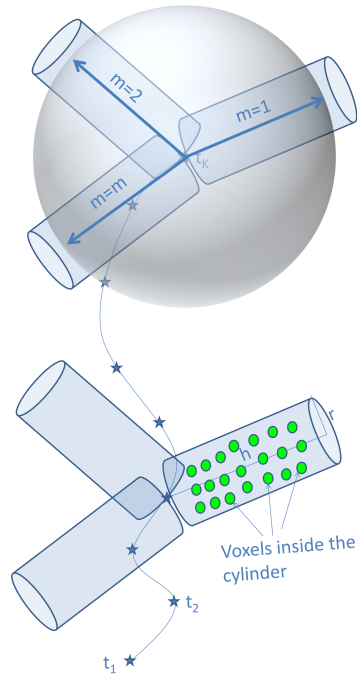


Figure 4.4: *Illustration of construction of the NRFOD representation of a fiber. At each point on the fiber, the neighborhood is probed with cylinders in M directions and a histogram of resolved fiber orientations in the cylinders are computed.*

Now that we have a fiber representation in terms of local diffusion orientation histograms around each fiber point, we devise a fiber-to-fiber distance measure as follows. Generally, two histograms can be compared using a measure such as the Chi-Square histogram distance ([89]). Let $G = \{g_1, g_2, \dots, g_N\}$ and $H = \{h_1, h_2, \dots, h_N\}$ be two his-

tograms with N bins. The Chi-Square distance between G and H is defined as

$$\chi_{G,H}^2 = \frac{1}{2} \sum_{i=1}^N \frac{(g_i - h_i)^2}{g_i + h_i}. \quad (4.1)$$

Let $T = \{t_1, t_2, \dots, t_K\}$ and $U = \{u_1, u_2, \dots, u_K\}$ be two fibers that both have K uniformly sampled points. If the input fibers do not satisfy this condition, the fibers are simply resampled such that the condition is satisfied. Further, let P and R be the NRFOD representations of fibers T and U . Then, the proposed neighborhood resolved fiber orientation distribution distance (NRFODD) between the two fibers is defined as

$$\text{NRFODD}(T, U) = \min(d_{\text{direct}}(T, U), d_{\text{flipped}}(T, U)) \quad (4.2)$$

where

$$d_{\text{direct}}(T, U) = \frac{\sum_{k=1}^K \sum_{m=1}^M \chi_{P_{km}, R_{km}}^2}{KM}, \quad (4.3)$$

and

$$d_{\text{flipped}}(T, U) = \frac{\sum_{k=1}^K \sum_{m=1}^M \chi_{P_{(K-k+1)m}, R_{km}}^2}{KM}. \quad (4.4)$$

where P_{km} is the histogram at the k th point of the fiber T for the probing direction m and similarly, R_{km} is the histogram at the k th point of the fiber U for the probing direction m . Calculating a flipped distance is necessary due to the ambiguity in start and end points of fibers.

Notice that the proposed fiber-to-fiber distance measure is independent of Euclidean distances between the points defining the fibers and is instead solely determined by the fiber orientation distributions around them. This property makes the proposed measure more reliable than Euclidean-distance based measures when comparing fibers that are originally defined on different spaces and registered to a common space because the proposed measure is translation invariant. It is however still affected by errors in the rotational component of the registration which is why N , the number of bins in the histograms, should be chosen carefully such that it is large enough that the orientation space is not undersampled but small enough that the distance measure is insensitive to small rotations (see Section 4.2.1).

4.1.6 Density-based Clustering with OPTICS

The aim of the clustering step is to separate the initial set of projection fibers into two bundles as ML and CST, the SCP fibers into left and right SCP and ICP bundles into left and right ICP and to remove any spurious fibers in MCP as well as in other bundles. Density-based clustering is based on the intuition that data points within a cluster will be densely packed compared to outside of the cluster. This approach is suitable for fiber clustering as evidently a fiber bundle consists of densely packed fibers.

OPTICS ([86]) is a density-based clustering algorithm that outputs not a set of clusters but a reordering of the fibers and a “reachability distance” that together encode their hierarchical clustering structure. The nature of this output is illustrated in Figure 4.5. Each possible “valley” in the output is a cluster. The OPTICS method has several advantages compared to other clustering methods. It has only two parameters that can be set relatively easily compared to a method like spectral clustering; it contains an inherent noise removal mechanism which is very useful for fiber clustering (fibers that are less densely packed with other fibers have higher reachability distances); it encodes the hierarchical clustering structure in a way that is easily visualized as in Figure 4.5³; and the hierarchical information allows incorporation of neuroanatomical priors to select neuroanatomically meaningful clusters from all candidate clusters. Although disjoint clusters can be extracted from the output with a simple horizontal cut method as illustrated in (b,c), this scheme is incapable of detecting clusters of varying density and it is not clear what value one should cut at to capture a specific bundle. Instead, we propose to select the most anatomically meaningful cluster from all possible clusters encoded in the output. In order to do so, reference bundles are previously reconstructed in a set of subjects which we will call the “training set”. Then, when performing clustering on new subjects, the most anatomically meaningful cluster is determined by comparing all clusters encoded in the OPTICS output to the reference bundles in the training set. The details of the creation of the reference bundle set and the cluster selection scheme are given in Section 4.1.7. In the experiments, $minPts = 30$, $\epsilon = 200$ were used as OPTICS parameters and $\xi = 0.001$ was used for the extraction of all possible clusters.

³Figure 4.5 is same as Figure 3.3, it is replicated here for convenience

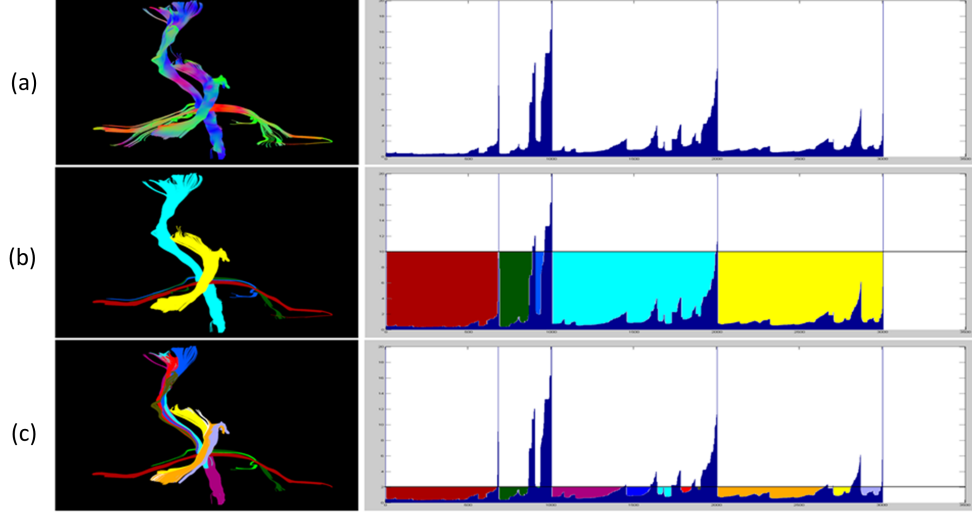


Figure 4.5: (a)-Left: Input fibers colored according to local diffusion direction. (a)-Right: OPTICS output: ordered reachability distances (y) versus fiber indices (x). (b)-(c)-Left: Fibers colored according to clustering done with horizontal line cut method with $y = 10$ and $y = 2$, respectively. (b)-(c)-Right: OPTICS output with colored areas corresponding to clusters on the left, indicated with the same color.

4.1.7 Reference Bundle Creation and Cluster Selection from OPTICS Output

The training set is an initial fixed set of S subjects selected for creating the reference bundles. The following nine bundles are extracted from each subject in the training set using the manual ROI method: left CST, right CST, left ML, right ML, left SCP, right SCP, left ICP, right ICP and MCP. The reference bundles are created on the subject native space and then transformed to the MNI152 space using the affine registration of T1-weighted MR image of subjects to MNI152 T1 template with 1mm resolution. Those manually extracted bundles, which are now defined on the MNI152 space, are used as a reference to guide the selection of anatomically meaningful clusters from the OPTICS output when clustering new subjects. We note that a different training set is not required for a different dataset that includes new subjects.

When performing clustering on a new subject, i.e. a subject from the test set, the reference fiber bundles are transformed to the subject space with affine registration. Then, a

bundle-to-bundle similarity measure, Bundle-based Minimum Distance (BMD) [90], which is based on an average of minimum fiber-to-fiber distances between bundles, is used to compare each candidate cluster in the OPTICS output to all reference bundles. The minimum average direct-flip (MDF) distance that is used in the BMD calculation in the original article is based on an average of Euclidean distances between points of the two given fibers. Here, the fiber-to-fiber distance in BMD is replaced with the proposed distance NRFODD. Let us call this distance $\text{BMD}_{\text{NRFODD}}$, the set of all possible clusters $C = \{C_1, C_2, \dots, C_n\}$, and the set of reference bundles brought to subject space after a registration step $R = \{R_1, R_2, \dots, R_S\}$ ($S = 10$ in our case). Then, C_i is selected as the best cluster by simply solving

$$\arg \min_{C_i} \sum_{j=1}^S \text{BMD}_{\text{NRFODD}}(C_i, R_j), \quad \text{for } i = 1, \dots, n. \quad (4.5)$$

Finally, using the proposed clustering and cluster selection scheme, each fiber bundle of interest is extracted from the corresponding initial fiber collection. It is important to emphasize that $\text{BMD}_{\text{NRFODD}}$ is translation-invariant and hence invariant both to the translational component of the computed affine transformation between the subject spaces and the translation of bundles due to individual variability. Hence, the proposed method is expected to perform better than simple atlas-based approaches on spatially close bundles.

4.2 Results

4.2.1 Selection of NRFOD Parameters

As explained in a previous section, constructing the NRFOD representation involves the following parameters: K : the number of points per tract, M : the number of probing directions at each point on a tract, N : the number of bins in the histograms, h : the height of probing cylinders and r : the radius of cylinders. It is not clear what values would be best for these parameters. As testing all possible parameter settings was not time-wise feasible, we used the following approach: First, K is fixed to 50 because the longest expected length for the bundles of interest is around 200 mm and 50 sample points

are deemed sufficient to both probe the neighborhood and achieve a good representation. Next, as the neighborhood probing is introduced analogous to a human’s approach, r was fixed to $h/2$ for a “reasonably-shaped” cylinder. Then, in the first step of parameter selection, we fixed $N = M/2$ because M is the number of probing directions sampled on a full sphere and N is the number of orientation bins sampled on a half-sphere. Varying only M and h on the training set of 10 subjects, the proposed algorithm was used to extract each bundle of interest in the brainstem using the different parameter settings. The BMD [90] with the original Euclidean-based fiber-to-fiber distance MDF was used to compare the closeness of the bundles obtained with manual extraction and the proposed algorithm. The mean BMD values across all training subjects for various different parameter settings are given in Figure 4.6. No significant improvement was observed for higher M and h values compared to $M = 20$ and $h = 6$, hence these parameter values are considered as a good tradeoff between the score and computation cost. Finally, we fixed $M = 20, h = 6$ and varied N which showed no significant improvement for higher values than $N = 10$. It is important to set N as small as possible because in addition to a less computation cost, smaller values of N will make the representation less sensitive to rotation. On the other hand, very small values like $N = 5$ do not sufficiently sample the orientation space and significantly reduce accuracy. Guided by these experiments, the parameters are set as $K = 50, M = 20, N = 10, h = 6, r = 3$ for further tests and results in the subsequent sections. With the selected parameter values, the runtime of the proposed method was approximately 30 minutes on a workstation with 4 Intel Xeon E5-2690 v3 @ 2.60GHz processors (the code is not optimized for performance nor implemented on GPU).

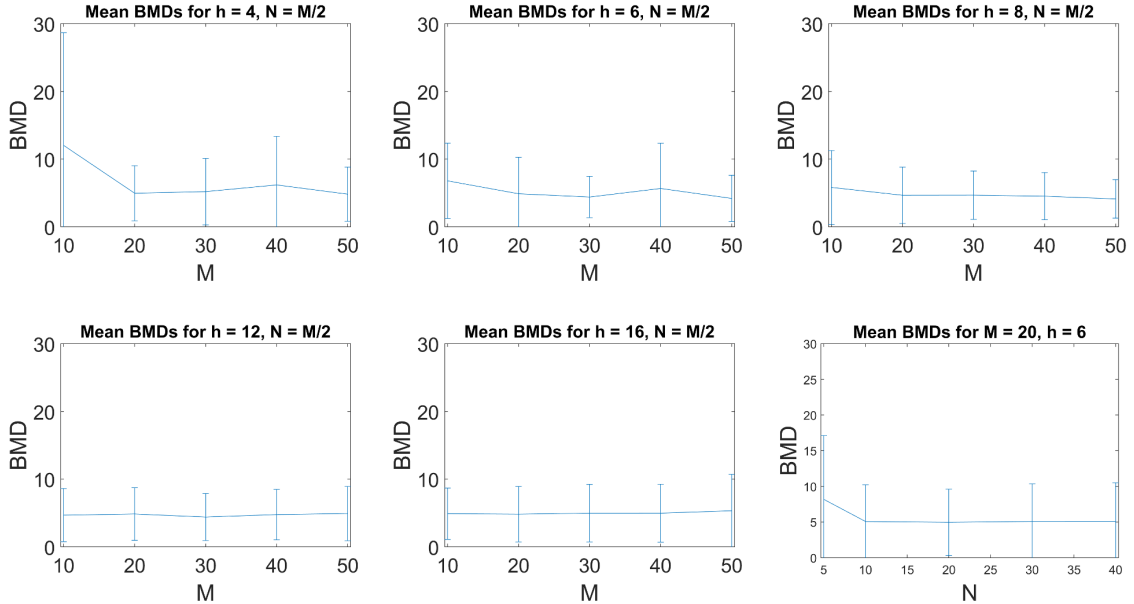


Figure 4.6: Mean BMD values between manually extracted bundles and bundles extracted by the proposed method for various parameter settings. $K = 50, r = h/2$ for all plots. Mean is taken across all 10 training subjects and all bundles of interest.

4.2.2 Sensitivity of NRFODD to Registration Errors Compared to MDF

In order to illustrate the sensitivity of the proposed fiber-to-fiber distance measure to registration errors, a subject was randomly selected from the training set and 250 tracts from each bundle of interest were first extracted in the original space using the manual ROI method. Then, the diffusion-weighted images (DWI) of the subject were rotated around all 3 axes with $\theta = 0.05, 0.10, 0.15, 0.20$ radians and translated in all directions by 2.5, 5.0, 7.5 and 10.0 millimeters. The manually placed ROIs utilized for the extraction of bundles of interest in the original space were also transformed with the same transform and used to extract the bundles in the transformed spaces. The fiber-to-fiber distances from all tracts in the original space to all tracts in the transformed space are then computed for each transformation with both the proposed distance measure and the MDF. Heat maps of the resulting distance matrices are given in Figure 4.7. In the heat maps, heat colors corresponding to low distances are desired in 250×250 square blocks on the diagonal

since those distances are between fibers representing the same bundle. Similarly, heat colors corresponding to high distances are desired outside of the 250×250 square blocks on the diagonal since those distances are between fibers representing different bundles. Note the difference in the ranges of the distance values for the MDF and NRFODD. It can be observed in the translation experiments (first two rows) that the MDF distance starts to produce lower distances between fiber pairs from different bundles than between fiber pairs from the same bundle as soon as the translations exceed a few mm's when the bundles in question are spatially close like e.g. CST and ML. As the NRFODD is translation-invariant, the distance matrices for different amounts of translation are very similar. Note that the matrices are not exactly the same because the fiber sets in transformed spaces are not the original fibers that are transformed, rather, the ROIs and the DMRI space are transformed and new fibers are extracted in each new space. Moreover, NRFODD performs better than the MDF distance in distinguishing between the ML and CST, as the MDF distance matrices have very similar colors on the ML-ML, CST-CST and CST-ML blocks whereas in NRFODD matrices, CST-ML blocks are more distinguishable from ML-ML and CST-CST blocks. Further, as can be observed from the rotation experiments (third and fourth rows), although the proposed measure is based solely on the orientation distribution of local fiber populations, its sensitivity to rotation is lower than that of the MDF. The only disadvantage of the proposed method compared to the MDF seems to be in the separation of the left and the right SCP when there is very small or no transformation. This is likely caused by the fact that there are no major bundles surrounding the neighborhood of SCP, thus lowering the distinctiveness of the NRFOD representation. In order to quantify the discriminative power of the two different distances under registration errors, we use the error rate, i.e. the number of times the nearest neighbor of a fiber comes from a different bundle divided by the total number of fibers in the distance matrices. The error rates of the different distances are given in Table 4.1 and demonstrate the invariance of the NRFODD to translation and its insensitivity to small rotations compared to the MDF.

Table 4.1: The error rate of the distances NRFODD and MDF under various registration errors (no error, translations from 2.5 to 10.0 mm and rotations from 0.05 to 0.20 radians). The error rate is defined as the number of times the nearest neighbor of a fiber comes from a different bundle (i.e. the number of rows for which the minimum is not achieved on the 250×250 diagonal blocks) divided by the total number of fibers on the distance matrices.

	No Transform	2.5 mm	5.0 mm	7.5 mm	10.0 mm	0.05 rad	0.10 rad	0.15 rad	0.20 rad
NRFODD	0.0009	0.0013	0.0013	0.0004	0.0009	0.0027	0.0133	0.0524	0.1418
MDF	0.0022	0.0751	0.1787	0.2933	0.3564	0.0222	0.1996	0.3671	0.4378

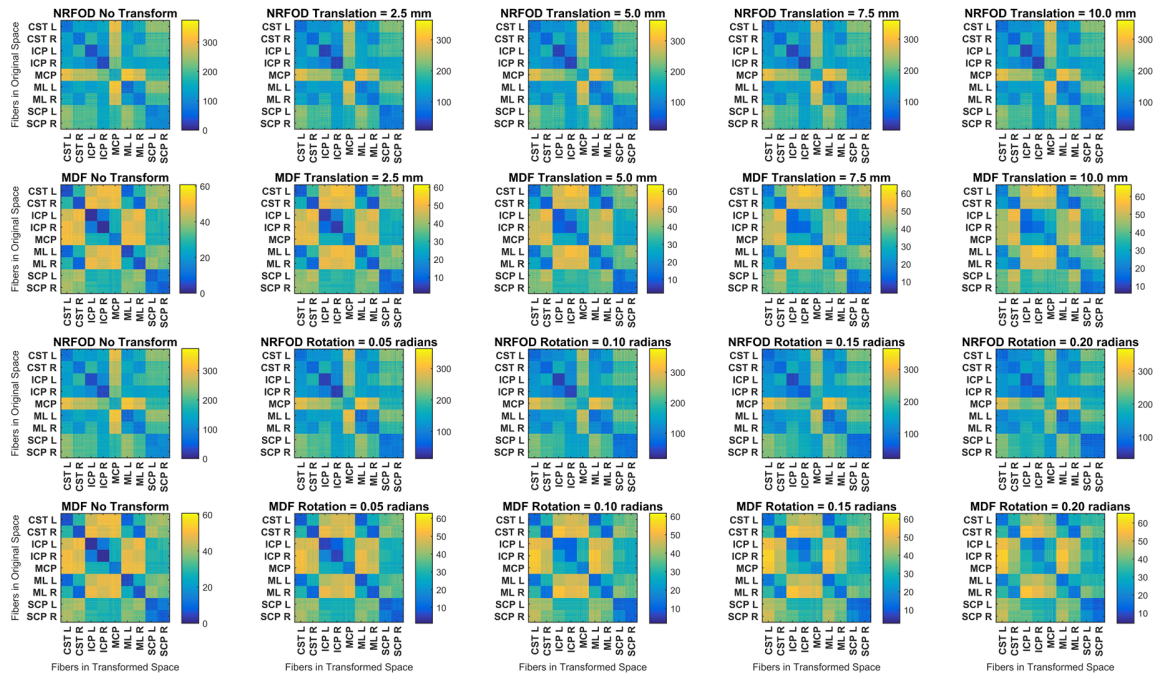


Figure 4.7: Heat maps of the distance matrices between tracts on the original space and the transformed spaces. There are 250 tracts from each bundle of interest in the following order: CST left, CST right, ICP left, ICP right, MCP, ML left, ML right, SCP left, SCP right.

Table 4.2: Quantitative comparison of the proposed method (*P_NRFODD*), the proposed method with MDF fiber-to-fiber distance (*P_MDF*), the naïve maximal overlap method (*MaxOverlap*) spectral clustering [4, 5] with added cluster selection: (*S+CS*); and Tract Querying (*TQ*): [6]. Bundles created by the manual ROI method are used as “ground truth” and the mean \pm standard deviation of BMD and Cohen’s Kappa values between the bundles created by the automatic methods and the “ground truth” are given for each fiber bundle of interest. The best results for both measures are highlighted in bold. Note that BMD is a dissimilarity measure and Cohen’s Kappa is a similarity measure, hence higher values represent better accuracy for Cohen’s Kappa and lower accuracy for BMD.

	CST_L	CST_R	MLL	MLR	SCP_L	SCP_R	ICP_L	ICP_R	MCP
P_NRFODD_BMD	2.13 \pm 2.33	1.15 \pm 0.49	3.10 \pm 3.87	6.73 \pm 9.18	10.68 \pm 14.27	6.88 \pm 4.94	3.33 \pm 5.54	2.82 \pm 3.86	7.20 \pm 4.14
P_MDF_BMD	3.28 \pm 6.20	6.08 \pm 10.53	9.15 \pm 23.97	13.03 \pm 26.57	10.53 \pm 15.77	8.14 \pm 8.31	4.88 \pm 6.80	3.78 \pm 5.21	9.01 \pm 11.06
MaxOverlap_BMD	2.40 \pm 1.36	2.49 \pm 1.81	3.04 \pm 2.06	9.92 \pm 30.32	11.98 \pm 5.37	23.75 \pm 20.56	14.71 \pm 21.40	19.31 \pm 13.49	12.02 \pm 4.88
(TQ)_BMD	24.36 \pm 21.43	24.39 \pm 27.84	12.89 \pm 14.85	14.47 \pm 8.95	29.19 \pm 26.68	30.02 \pm 19.61	17.49 \pm 25.76	11.63 \pm 8.76	31.79 \pm 14.54
(S+CS)_BMD	2.62 \pm 1.72	4.33 \pm 5.80	6.40 \pm 7.84	7.29 \pm 9.30	13.68 \pm 12.95	13.06 \pm 9.42	4.78 \pm 4.97	7.02 \pm 6.34	9.85 \pm 9.92
P_NRFODD_Kappa	0.70 \pm 0.19	0.77 \pm 0.08	0.58 \pm 0.16	0.51 \pm 0.20	0.58 \pm 0.18	0.56 \pm 0.12	0.61 \pm 0.18	0.67 \pm 0.08	0.70 \pm 0.09
P_MDF_Kappa	0.71 \pm 0.17	0.69 \pm 0.16	0.57 \pm 0.17	0.46 \pm 0.22	0.53 \pm 0.12	0.56 \pm 0.14	0.57 \pm 0.17	0.62 \pm 0.16	0.68 \pm 0.15
MaxOverlap_Kappa	0.72 \pm 0.08	0.78 \pm 0.04	0.59 \pm 0.05	0.62 \pm 0.04	0.32 \pm 0.11	0.24 \pm 0.12	0.23 \pm 0.08	0.19 \pm 0.06	0.56 \pm 0.06
(TQ)_Kappa	0.14 \pm 0.04	0.15 \pm 0.06	0.20 \pm 0.06	0.24 \pm 0.11	0.19 \pm 0.10	0.17 \pm 0.08	0.34 \pm 0.15	0.30 \pm 0.12	0.13 \pm 0.04
(S+CS)_Kappa	0.74 \pm 0.04	0.76 \pm 0.06	0.69 \pm 0.06	0.64 \pm 0.09	0.50 \pm 0.12	0.46 \pm 0.11	0.47 \pm 0.14	0.45 \pm 0.12	0.68 \pm 0.11

Table 4.3: Visual scoring by two experts. Score is given based on how well the reconstructed bundle agrees with known neuroanatomy. 1: Very poor; 2: Poor; 3: Mediocre; 4: Good; 5: Very good. R1 refers to Rater 1; R2: Rater 2; Manual: Bundle reconstructed with the manual ROI method; Auto: Bundle reconstructed with the proposed automatic method.

	CST_L	CST_R	MLL	MLR	ICP_L	ICP_R	SCP_L	SCP_R	MCP
R1_Manual	4.95 \pm 0.22	4.95 \pm 0.22	4.80 \pm 0.41	4.75 \pm 0.44	4.90 \pm 0.31	4.95 \pm 0.22	4.60 \pm 0.60	4.60 \pm 0.60	4.80 \pm 0.41
R1_Auto	4.75 \pm 0.55	4.90 \pm 0.31	4.20 \pm 1.00	4.35 \pm 0.81	4.50 \pm 0.51	4.50 \pm 0.51	3.55 \pm 0.89	3.65 \pm 0.59	4.25 \pm 0.64
R2_Manual	4.75 \pm 0.44	4.85 \pm 0.37	4.75 \pm 0.55	4.80 \pm 0.41	4.85 \pm 0.37	4.95 \pm 0.22	4.25 \pm 0.55	4.40 \pm 0.50	4.90 \pm 0.45
R2_Auto	4.35 \pm 0.75	4.65 \pm 0.49	4.20 \pm 0.83	4.20 \pm 0.70	4.60 \pm 0.60	4.50 \pm 0.51	3.40 \pm 0.82	3.95 \pm 0.60	4.10 \pm 0.45

4.2.3 Comparison of the Proposed Method to the Manual ROI Method

We validate the proposed method by comparing it to the manual ROI method which is considered the most reliable but time-consuming approach. The bundles are reconstructed on the 20 test subjects using the two methods and are compared quantitatively in terms of Cohen’s Kappa and BMD values, and qualitatively by visual inspection of two expert raters (Rater 1: ZF- radiology specialist; Rater 2: UT - neurosurgeon). The raters were blinded for the evaluation, i.e. they were not told which bundles are manually extracted and which ones are automatically extracted. The ROIs for manual extraction were drawn by a senior PhD candidate after receiving training from the raters. In order to calculate Cohen’s Kappa values, the bundles are converted to binary 3D volumes where each voxel is assigned a true or false value based on whether the voxel contains a point from the bundle. Figure 4.8 shows visualizations of fiber clusters created by the proposed method and the manual method. Mean and standard deviation of Kappa and BMD values for each bundle are given in Table 4.2 and a visualization is given for each bundle when they achieve their best and worst BMD scores in Figure 4.9. Mean and standard deviation of qualitative scores given by experts after visual inspection are given in Table 4.3. While the proposed method is not quite as accurate as the manual ROI method, it achieves good to very good evaluations by the experts on all bundles except the SCP in which the average evaluation is between good and mediocre. The relatively poor performance on SCP compared to other bundles were expected by the fiber-to-fiber distance matrices discussed in the previous section (Figure 4.7). While the proposed method does not confuse the SCP fibers with other bundles, it performs poorly at distinguishing between the right and left SCP bundles. Thus, in a practical implementation, utilizing a heuristic to separate the two hemispheres for instance through a brain hemisphere mask will certainly improve the method’s performance on SCP.

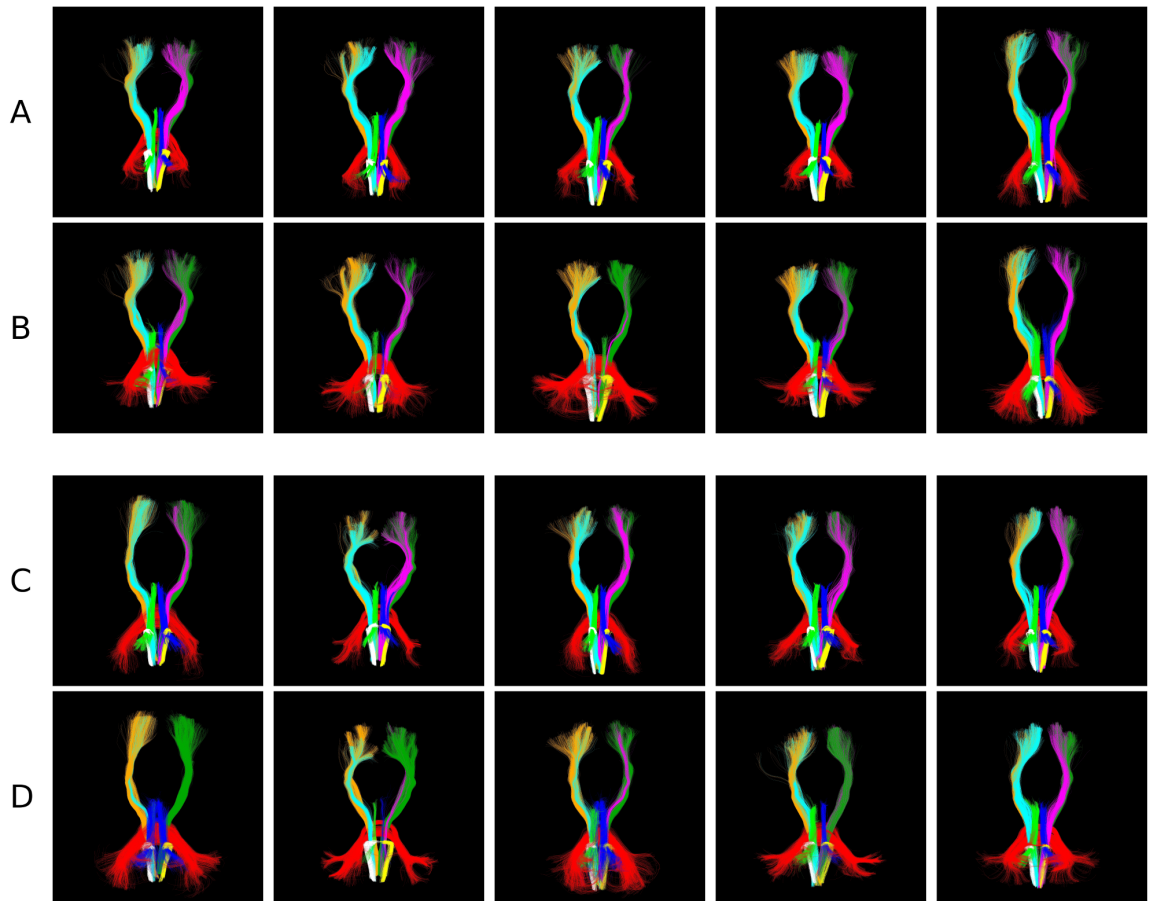


Figure 4.8: *Visualization of clustering results from the set of test subjects. A: Manual ROI method for subjects 1-5; B: Proposed method for subjects 1-5; C: Manual ROI method for subjects 6-10; D: Proposed method for subjects 6-10. Tracts are colored according to assigned bundle as follows: CST Left: orange; CST Right: dark green; ML Left: teal; ML Right: pink; ICP Left: white; ICP Right: yellow; SCP Left: green; SCP Right: blue; MCP: red.*

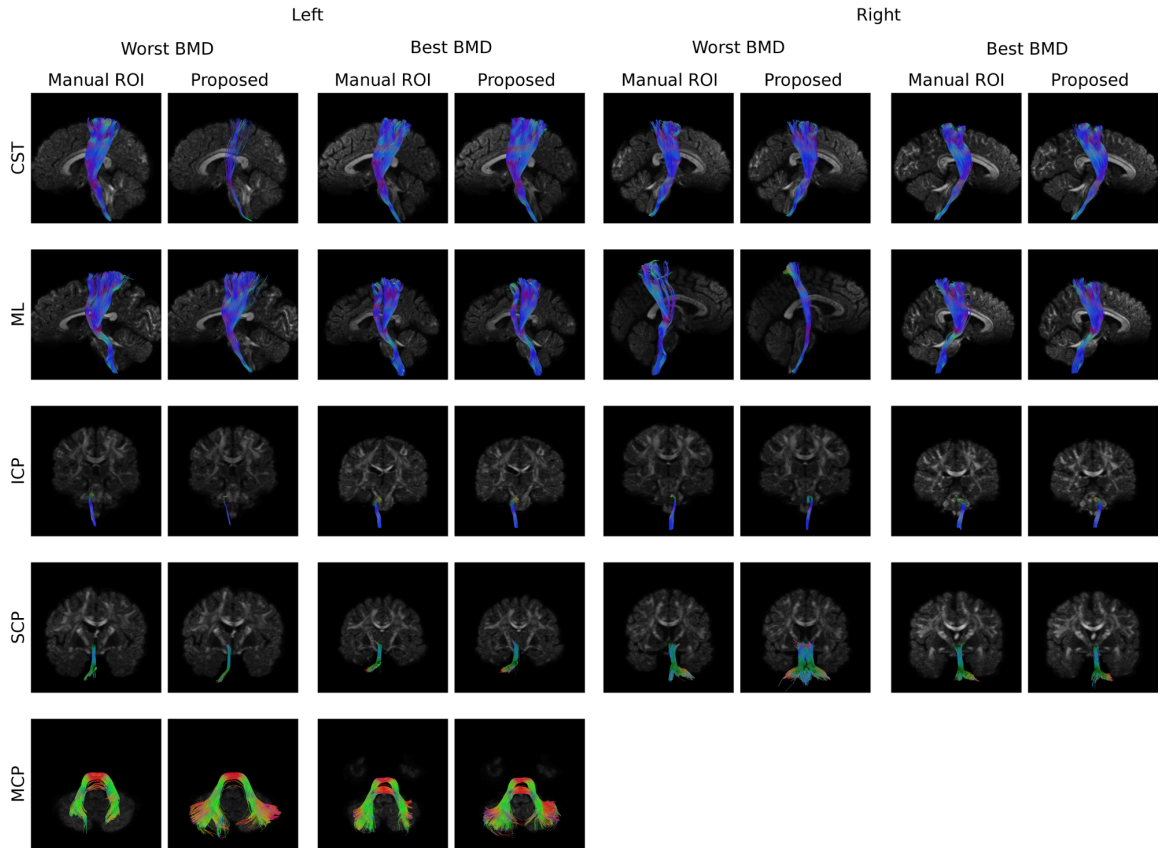


Figure 4.9: Visualization of bundles created with the manual ROI method vs. the proposed method for best and worst BMD values achieved among the test subjects. Tracts are colored according to local direction.

4.2.4 Comparison of the Proposed Method to Other Automatic Methods

The proposed method is compared to four other automatic approaches:

1. The proposed method which is modified to use the MDF fiber-to-fiber distances instead of NRFODD.
2. A naïve method where each fiber acquires the label of the reference bundle with which it maximally overlaps (MaxOverlap);
3. The spectral clustering method by [4, 5] with an addition of a cluster selection step (S+CS);

4. The tract querying method which is based on agglomerative hierarchical clustering and selection from the resulting dendrogram by [6] (TQ).

The codes of the spectral clustering and tract querying methods were kindly provided by the authors. In order to make a fair comparison, the step of the proposed method that constrains the initial fiber sets as candidate left projection fibers (left CST and ML), right projection fibers (right CST and ML), SCP, ICP and MCP is used for the other methods as well. The same training set as the proposed method is used to create the cluster atlases required by the spectral clustering method for each of the five different fiber sets. For the querying step of the tract querying method, the ICBM-DTI-81 white-matter labels atlas (http://www.loni.usc.edu/ICBM/Downloads/Downloads_DTI-81.shtml) is used to extract the nine bundles of interest. In order to quantitatively compare the automatic methods, bundles extracted with the manual ROI method are used as “ground truth”. Two different quantitative measures are used: BMD, a Euclidean-based bundle-to-bundle distance measure, and Cohen’s Kappa, a volumetric similarity measure. The bundles are converted to a binary volumetric mask using nearest neighbor method for the calculation of Kappa values. Since the spectral clustering method does not classify the clusters into anatomically known bundles and instead only clusters based on fiber distances, a cluster selection scheme must be incorporated to obtain a classification of the bundles in order to allow a quantitative comparison. We implemented the following procedure for this selection: the same reference bundles used for the proposed method were brought to subject spaces of the test data through affine registration. Then, the k clusters are sorted in ascending order according to their average BMD values with respect to the reference bundles. Finally, the clusters are iteratively merged starting from the cluster with the lowest BMD until adding a new cluster would increase the BMD value of the final bundle. In order to set k , the method was first tested with $k = 2, 4, 6, 8, 10, 20$ final clusters. The k value for which the mean BMD value across all bundles was minimum is selected, and all the test results are hence obtained with $k = 10$ in the spectral clustering method.

All five methods are run on the same test set of 20 subjects. Kappa and BMD values between resulting clusters of automatic methods and the clusters acquired by the manual ROI method are given in Table 4.2. A visualization of the clustering results for each

method on one of the test subjects is given in Figure 4.10. One can argue that the tract querying methodology described in [6] results in a traversal of the hierarchical tree which is too conservative and that, albeit good for tractography algorithms generating lots of false positive tracts, it might result in an underrepresentation of the extracted bundles⁴. Therefore, it was observed that the results lead to clusters that are much thinner than what is expected. The tract querying method, which is dependent on accurate registration, might be useful when the subject-standard space registration error is insignificant and the bundles of interest are thin bundles that are very prone to false positives, however, based on its available implementation, it apparently underperforms in the quantitative evaluations for the major brainstem bundles. According to the quantitative measures, the naïve maximal overlap method achieves surprisingly high accuracy for the CST and ML bundles where it is competitive with both the proposed method and the spectral clustering. However, it performs mediocly in MCP and quite poorly on the SCP and ICP. Overall, the proposed method performs better than all other methods for the SCP, ICP and MCP. This may have two reasons: First, the input fiber sets to the SCP, ICP and MCP contain more spurious fibers compared to the projection fiber sets due to the nature of the ROIs that are used to constrain the initial sets. Hence, density-based clustering that has an inherent noise removal mechanism performs better when the proportion of noisy fibers in the input set is higher. Second, as the main theoretical advantage of the proposed method is the translation-invariance of the NRFODD, it can be hypothesized that the selection of the ICP, SCP and MCP is more significantly affected by the translation error in transforming the reference bundles into the subject spaces of the test set. It should be noted that the Kappa and BMD values are not very sensitive to the separation of geometrically close bundles like ML and CST or left and right SCP. As a result, the quantitative analysis may not reflect how qualitatively well the separation of these bundles is achieved. For example, despite the high accuracy of the maximal overlap method on CST and ML with respect to quantitative measures, it can significantly confuse CST and ML bundles in some subjects as shown in Figure 4.11. Right SCP and ICP are also given in Figure 4.11 to give better insight into why the maximal overlap method performs poorly

⁴Personal communication with Dr. D. Wassermann, 19 Apr 2017

on those bundles. The initial fiber sets for those bundles contain many spurious fibers that cannot be removed by the maximal overlap method.

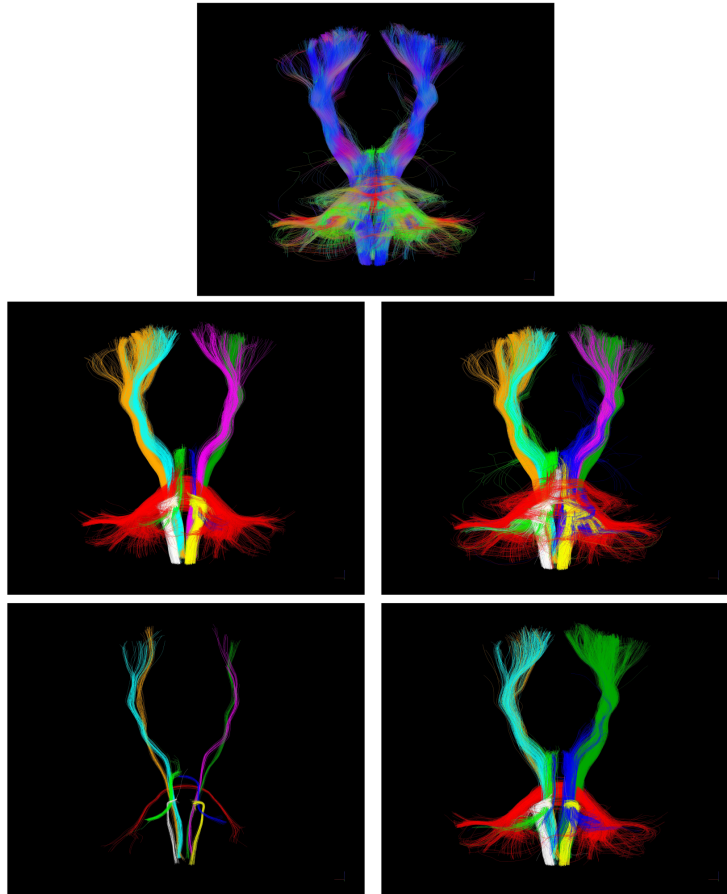


Figure 4.10: Visualization of clustering results for the proposed method (middle left), the naïve maximal overlap method (middle right), tract querying method (bottom left) and spectral clustering with additional cluster selection (bottom right) on one of the subjects in the test set. Fiber sets used as input to the clustering algorithms are shown at the top and are colored according to local direction. Clustered tracts are colored according to assigned bundle as follows: CST Left: orange; CST Right: dark green; ML Left: teal; ML Right: pink; ICP Left: white; ICP Right: yellow; SCP Left: green; SCP Right: blue; MCP: red.

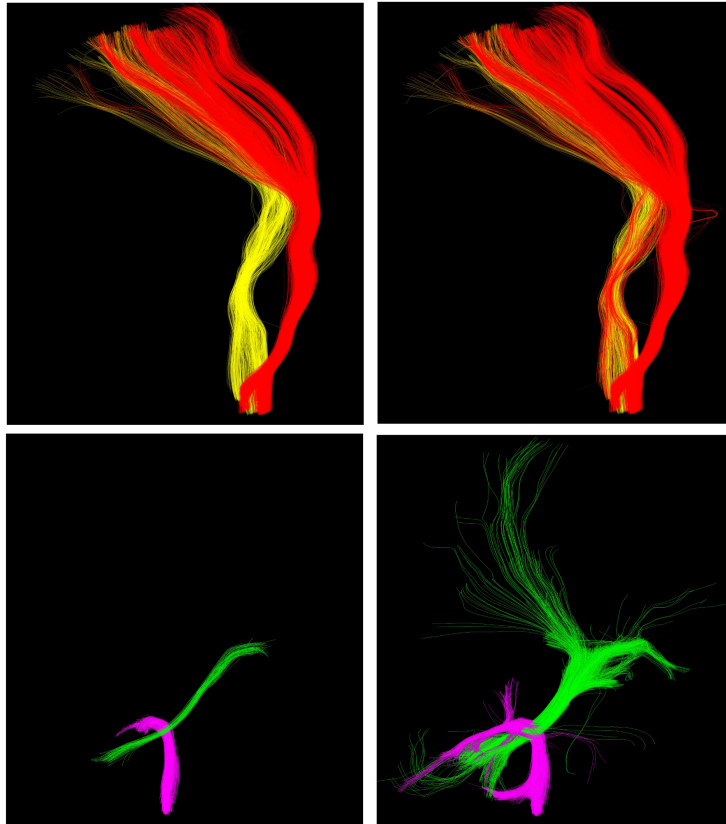


Figure 4.11: *A comparison of the proposed method (left) to a naïve maximal overlap approach (right) using the reference bundles for right CST (red) and ML (yellow) fibers (top row) and right SCP (green) and ICP (purple) fibers (bottom row) on one of the subjects in the test set. The maximal overlap approach can confuse spatially close bundles like CST and ML and can have many spurious fibers when the initial fiber set cannot be well-constrained by automatic ROIs as in the case of the SCP and ICP.*

4.2.5 Sensitivity of the Proposed Method to the Reference Bundles

In order to test the sensitivity of the proposed method to the reference bundles, we experiment with three different training-test set configurations. Training set 1 includes the original set, which is used in all the experiments in previous sections. Training set 2 includes subjects 11-20 and test set 2 becomes subjects 1-10 and 21-30; training set 3 includes subjects 21-30 and test set 3 becomes subjects 1-20. To compare the results

Table 4.4: *The mean and standard deviation of BMD and Cohen’s Kappa values between results of the proposed method and manual bundles using different training and test sets. Training Set 1 includes subjects 1-10 and its test set includes subjects 11-30; Training Set 2 includes subjects 11-20 and its test set, subjects 1-10 and 21-30; Training Set 3 includes subjects 21-30 and its test set, subjects 1-20.*

	CST.L	CST.R	ML.L	ML.R	SCP.L	SCP.R	ICP.L	ICP.R	MCP
Training Set 1 BMD	2.13 ± 2.33	1.15 ± 0.49	3.10 ± 3.87	6.73 ± 9.18	10.68 ± 14.27	6.88 ± 4.94	3.33 ± 5.54	2.82 ± 3.86	7.20 ± 4.14
Training Set 2 BMD	1.70 ± 1.21	1.64 ± 2.15	4.14 ± 3.92	8.40 ± 8.89	16.12 ± 19.93	7.27 ± 5.51	3.57 ± 5.62	3.28 ± 3.26	8.63 ± 4.75
Training Set 3 BMD	1.93 ± 1.10	1.37 ± 0.54	3.31 ± 3.53	7.44 ± 12.10	11.66 ± 12.47	8.55 ± 10.90	4.15 ± 6.01	2.65 ± 2.89	7.91 ± 4.42
Training Set 1 Kappa	0.70 ± 0.19	0.77 ± 0.08	0.58 ± 0.16	0.51 ± 0.20	0.58 ± 0.18	0.56 ± 0.12	0.61 ± 0.18	0.67 ± 0.08	0.70 ± 0.09
Training Set 2 Kappa	0.75 ± 0.10	0.79 ± 0.07	0.56 ± 0.17	0.51 ± 0.18	0.53 ± 0.18	0.55 ± 0.13	0.59 ± 0.20	0.65 ± 0.13	0.68 ± 0.08
Training Set 3 Kappa	0.69 ± 0.14	0.77 ± 0.11	0.58 ± 0.15	0.50 ± 0.21	0.55 ± 0.18	0.56 ± 0.16	0.59 ± 0.17	0.64 ± 0.14	0.69 ± 0.09

with these different configurations, we use the same approach as in Section 4.2.4. The mean BMD and Cohen’s Kappa values with respect to manual bundles achieved with the different configurations are reported in Table 4.4. From this table, the inter-reference set average over BMD differences between each pair of fiber bundles is 1.0087 mm, and the standard deviation of the maximum inter-reference difference across bundles is 1.553 mm. Similarly, the inter-reference set Kappa value differences on the average is 0.017 over all bundles, with the standard deviation of maximum differences being 0.0166.

4.3 Discussion

We introduced a new descriptive fiber representation based on the resolved fiber orientation distributions around a fiber. This representation is inspired by the human approach to differentiating which neuroanatomical bundle a fiber belongs to and allows the definition of a fiber-to-fiber distance measure that is translation-invariant, making the measurement of fiber-to-fiber distances across subjects in different spaces more robust. Utilizing the advantages of the new fiber representation, we proposed an automatic fiber clustering method that combines ROI-based and similarity-based clustering. As with other automatic fiber clustering methods, the aim is to reduce or ideally eliminate the need for human effort and the potential for human bias and error for the task of meaningful clustering of fibers.

Computation time for the proposed automatic method is on the order of minutes, potentially a few minutes with a GPU implementation, whereas a manual method typically takes half an hour to an hour as reported by the collaborating experts.

The proposed NRFOD-based method has better overall performance than the other automatic clustering methods we have tested in terms of Cohen’s Kappa and BMD values with respect to manually extracted bundles, which are used as “ground truth”. Visually, the NRFOD method usually creates anatomically meaningful bundles with close to expected thickness and trajectories. According to the quantitative measures, the performance of different methods can significantly vary between different bundle classes. Especially of interest is the unexpected performance of the naïve maximal overlap method on the CST and ML. This has important implications: Our idea of using reference bundles manually extracted on a “training set” to guide the clustering of new subjects is a valid approach that can both be used as part of a clustering framework or in some cases even be sufficient by itself. Hence, the investigation of more sophisticated ways than the naïve maximal overlap approach of classifying the fibers using the reference bundles such as supervised machine learning methods seems to be an important future direction. The validity of using reference bundles may however depend on a variety of factors such as the registration errors between the “training” and “test” subjects; the nature of the bundle of interest, e.g. its shape, its closeness to other bundles and its variability across different individuals; and the degree of shape deformations of the bundles when pathology is involved. As a consequence, it may be desirable to use different clustering methodologies based on these factors. For example, an unsupervised clustering step may not be necessary for certain bundle classes when the subject is healthy and the registration error to “training” subjects is small. Similarly, the advantage of using the proposed NRFOD representation and the associated NRFODD fiber-to-fiber distance becomes more pronounced as the fiber collection input to the algorithm become noisier, i.e. involves spurious fibers, and as the amount of registration error increases. The effect of each of the aforementioned factors on different clustering approaches requires further investigation in order to better understand which type of methods would be more appropriate for a given application.

While the proposed method achieved the best overall performance on our experiments,

it is important to note that the experiments were only performed on healthy subjects and the robustness of the method to shape changes of the fibers due to pathologies is unknown. Robustness analysis and evaluation for pathological data is difficult for several reasons: The deformation due to tumors largely depends on the size and type of the tumor. Different types of tumors produce different types of deformations and in order to analyze the robustness to these deformations, ideally, a database of subjects with different sizes and types of tumors is required. In some cases, the tumor may push spatially close bundles into appearing as one bundle (e.g. CST and ML). In other cases, the distortion of the water diffusion due to the tumor may prevent bundle extraction in a region in and around the tumor, resulting in the bundle of interest to appear fragmented in the tract reconstruction. Sometimes, a bundle of interest cannot be extracted at all. As a consequence, the manual reconstruction becomes highly dependent on the experience and bias of the neuroanatomy expert. Creating manual bundles consistent across operators is thus very challenging when pathology is involved and it is not clear how an automatic method is to be evaluated quantitatively in these situations. Further, using a healthy training set could be inappropriate if the bundles of interest are significantly deformed by a tumor. Reference bundles based on the type and degree of the tumor may need to be constructed for such cases. Another approach would be to use a tumor mask to exclude histograms calculated near the tumor to make the selection based on reference bundles more robust to local deformations. If a large portion of the fibers is unchanged and only a small part is deformed due to a tumor, reference bundles constructed on healthy subjects could still be utilized. Due to the aforementioned difficulties with experimental analysis on pathological data, this analysis is left as future work.

Although the proposed clustering method was tested on brainstem fiber bundles for the current study, it is generalizable to all bundles in the brain. The only obstacle is the manual work required for creating a training set. The NRFOD representation and the NRFODD measure can be readily used for other bundles without other additional effort.

Validation of automatic fiber clustering results is an open research problem. [64] presented a study where they used the results of the manual ROI method as ground truth and showed that the agreement between opinion of physicians and a quality measure called

Adjusted Rand Index are low. They proposed a new measure called Normalized Rand Index that was designed to agree better with physicians’ perspective. It can be seen from our results that a similar disagreement is present between Kappa values, BMD values and our raters (see Table 4.2 and Table 4.3). For example, for the proposed method, the Kappa value for the MCP is higher than ICPs but expert ratings for the automatic results are lower for the MCP than the ICP. The BMD value agrees with raters in this case but the BMD difference between the right and the left ML is not reflected in rater scores. This phenomenon also makes it hard to tune the parameters of an automatic clustering algorithm since maximizing a quantitative measure such as Cohen’s Kappa or BMD clearly may not be ideal from a physician’s perspective. Conversely, optimizing according to a physician’s perception is prone to user bias, error and properties of the human visual system. For example, a human may overestimate the importance of false positives compared to false negatives as they are far easier to notice especially when examining a direction-colored visualization of a set of fibers. Thus, it is more plausible to tune the automatic algorithm according to the given application. If the clusters are to be used for assistance in surgical planning, it is reasonable to tune the method according to the physician’s preferences while it may be preferable to tune according to a quantitative measure if the bundles are to be used in correlational population studies. Furthermore, it should be noted that the “ground truth” itself is solely the result of the manual ROI method and prone to user bias and expertise.

4.3.1 Limitations

There are two important limitations of the proposed fiber representation NRFOD. (i) It requires the construction of ODFs and subsequently resolved fiber orientations in each voxel. The accuracy of the representation is thus dependent on the reconstruction method and it is not clear which reconstruction method should be chosen for a given DMRI data. The GQI method [31, 87] produced good results on the Connectome data we used in our experiments but may not be ideal for different scanning parameters, especially on clinical data with lower amount of gradient directions because the resolved fiber orientations can be different for different number of gradient directions [31]. (ii) When the amount of

major bundles passing through the neighborhood of a fiber is low, the descriptive power of NRFOD decreases as seen on the SCP.

In addition to the limitations of the NRFOD representation, the proposed clustering method itself requires the manual creation of a training set of the bundles of interest. Further, as with any clustering algorithm, the accuracy of the proposed method is also heavily influenced by the tractography method.

It should be noted that the proposed method does not require a specific tractography or an ODF reconstruction method, it only requires a volume of resolved fiber orientations and that the output of the tractography method is a set of fibers, each fiber defined as a set of points. Thus, in the future, more advanced diffusion MR techniques and tractography methods can be utilized as desired.

4.4 Conclusion

The proposed fiber representation based on neighborhood resolved fiber orientation distributions (NRFOD) is a more expressive representation than the simple fiber representation as a set of points in 3D space and allows the definition of a translation-invariant fiber-to-fiber distance measure (NRFODD). Hence, it improves robustness to registration errors compared to fiber distance measures based on Euclidean distances when working with fibers extracted from different subject spaces. This advantage is utilized in a fiber clustering framework by incorporating prior neuroanatomical information in the form of training sets of manually extracted bundles, improving the anatomical meaningfulness of resulting clusters. Furthermore, the proposed method is demonstrated on labeling five major white matter fiber bundles in the brainstem, which are relatively less analyzed.

While the proposed method achieved closer results to the manual ROI method compared to the other automatic methods in terms of Cohen’s Kappa and BMD values, it was rated as less accurate than manual results by our expert raters. Hence, while the proposed method cannot fully relieve the experts from the tedious task of manual ROI placement, it can downscale the required effort if used in a semi-automatic framework. It can reduce human bias and errors caused by human expertise and fatigue by providing an initial

point or second opinion. Furthermore, the NRFOD representation and the corresponding fiber-to-fiber distance measure NRFODD can facilitate analysis in population-based connectivity studies on neurological and developmental diseases that relate to the structural organization of fiber pathways in the brain.

4.A The determination of the probability of following a direction in tractography

Let $\mathbf{p} = (p_x, p_y, p_z)$ be the point we are currently on, $\mathcal{N} = \{\mathbf{n}_1, \mathbf{n}_2, \dots, \mathbf{n}_8\}$ the set of neighboring voxel centers and $\mathcal{C} = \{\mathbf{c}_1, \mathbf{c}_2, \dots, \mathbf{c}_K\}$ the set of candidate directions. The set \mathcal{C} consists of the following directions: negative and positive signed directions of all resolved fiber orientations in the neighboring voxels such that the angle between the direction the tractography has taken in the previous step and the resolved fiber direction is below the *maxAngle* threshold and that the corresponding QA value is above the *minQA* threshold. K is the number of these directions. After \mathcal{C} is determined, let us also define $Q = \{q_1, q_2, \dots, q_K\}$ as the set of QA values corresponding to the candidate directions, $\mathcal{D} = \{d_1, d_2, \dots, d_K\}$ as the Euclidean distances between \mathbf{p} and each of the center of the neighbor voxels that contain the resolved fiber orientations corresponding to the directions included in the set \mathcal{C} , and $A = \{a_1, a_2, \dots, a_K\}$ as the set of angles between the previous direction taken by the tractography and the corresponding candidate direction. Next, three functions are defined that assign a weight to each candidate based on distance, QA and angle separately are defined respectively as follows:

$$f_d(x) = \begin{cases} \frac{1}{x} & x \geq 0.01\text{mm} \\ 100 & \text{otherwise,} \end{cases} \quad (4.6)$$

$$f_q(x) = x, \quad (4.7)$$

$$f_a(x) = \cos(x). \quad (4.8)$$

Finally, the separate weights are combined using a weight for each different measure and the final probability of choosing a direction \mathbf{c}_k is calculated as

$$P_k = w_d \frac{f_d(d_k)}{\sum_{i=1}^K f_d(d_i)} + w_q \frac{f_q(q_k)}{\sum_{i=1}^K f_q(q_i)} + w_a \frac{f_a(a_k)}{\sum_{i=1}^K f_a(a_i)}. \quad (4.9)$$

In our experiments, $w_d = 0.4, w_q = 0.2, w_a = 0.4$ are used.

Chapter 5

Supervised Classification of White Matter Fibers Based on Neighborhood Fiber Orientation Distributions Using an Ensemble of Neural Networks ⁵

5.1 Materials and Methods

5.1.1 Dataset, Reconstruction of ODFs and Tractography

Diffusion-weighted images (DWI) and corresponding T1 images are from 30 unrelated subjects in the Human Connectome Project (HCP)’s publicly available “WU-Minn 500 Subjects + MEG2 dataset”⁶. The preprocessed data is used. The ODF (Orientation Distribution Function) reconstruction is performed by DSISudio⁷) with the general q-sampling imaging (GQI) method [31]. At most three orientations are resolved per voxel

⁵This chapter will be presented in the MICCAI Workshop CDMRI’18, Granada Spain, September 2018.

⁶www.humanconnectome.org/documentation/S500/

⁷dsi-studio.labsolver.org

using an ODF decomposition method [87] and a diffusion anisotropy value (QA) that quantifies the spin population in each resolved orientation is also obtained. For tractography, the method presented in [7] is utilized.

5.1.2 Manual ROI Selection on Standard Space to Constrain Input Tract Sets

As typically, a whole brain tractogram contains millions of streamlines that may not correspond to any true tract, it is generally a good idea to use a rough preprocessing step to reduce the size of the streamline set to be input to a more sophisticated classification algorithm. Five sets of ROIs are defined on the standard MNI152 space [84] to reconstruct a collection of streamlines that will include the following sets of tracts: left projection fibers (left CST and ML), right projection fibers (right CST and ML), SCP, ICP and MCP. Naturally, the ROIs are chosen large enough to account for possible registration errors and individual variations, since this is a preprocessing step meant to reduce computation cost and does not aim to achieve an accurate classification by itself.

5.1.3 Construction of the Training and Validation Sets

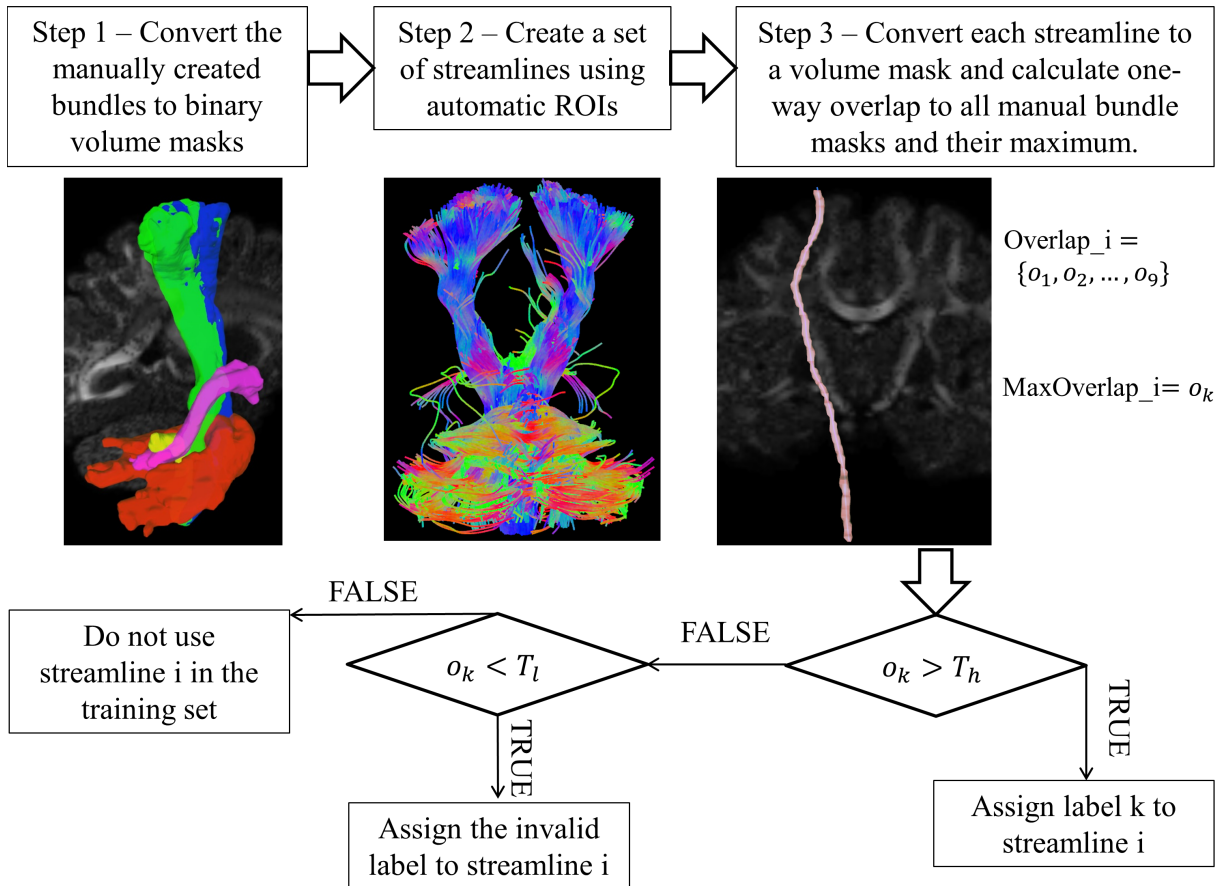


Figure 5.1: *Illustration of the proposed training set creation scheme. For every subject in the training set, Step 1: manually created streamlines for each fiber tract are converted to a volumetric mask. Depicted tract masks are colored as follows: Red: MCP, Blue: CST, Green: ML, Yellow: ICP, Pink: SCP. Step 2: A collection of streamlines are constructed by tractography using automatic ROIs. In step 3 and later, the process is illustrated for one streamline. This is repeated for every streamline created in step 2.*

Figure 5.1 depicts an illustration of a crucial procedure in our supervised fiber classification method, which inserts an “invalid” class that represents the class of invalid streamlines that do not belong to any true bundle. We reconstruct the following nine bundles of interest in the brainstem using the manual method for the 30 subjects in the dataset: left CST, right CST, left ML, right ML, MCP, left ICP, right ICP, left SCP and right SCP.

ROIs and ROAs are selected by the help of the radiology and neuroanatomy experts. An important issue that needs to be addressed when implementing a streamline-based supervised classification method is how to deal with invalid streamlines. Due to the existence of invalid streamlines, the classification problem is an “open set” recognition problem [91], which means that during the test phase, we expect to encounter streamlines that do not belong to any of the bundles the classifier has been trained on. Our approach in this study is to create a class of invalid streamlines in addition to the true bundles of interest, hence turning the problem into “closed set” recognition. Of course, the problem of how to create a training set for the “invalid” class remains. One way would be to use the streamlines that were deleted by the ROAs during manual classification, as in [92]. However, this would capture only a small subset of invalid streamlines that are likely to be present in an input set of streamlines encountered during the test phase because the ROIs used in manual reconstruction are much stricter and more accurate than the automatic ROIs used to constrain the streamline sets for the automatic classification. Another approach would be to use the automatic ROIs and many ROAs in the manual reconstruction, however this has the downside of requiring an extreme amount of time and adding additional human bias to the training set as well as being specific to the automatic ROIs chosen for this particular study, hence limiting the generalizability of the approach. Instead, we propose the following practical and important component to creating the training set which is also illustrated in Figure 5.1:

1. Convert the 9 bundles created with the manual classification method to binary volume masks.
2. Create an automatic streamline set using the automatic ROIs defined in Section 5.1.2.
3. Convert each streamline in the automatic input streamline set to a binary volume mask and calculate the one-way overlap to each bundle mask representing the true bundles and calculate the maximum overlap.
4. If the maximal overlap to true classes is higher than threshold T_h , assign to the streamline the class label of the true class for which the maximum overlap is achieved.

5. Otherwise, if the maximal overlap to true classes is lower than threshold T_l , assign to the streamline the label of the invalid class.

Notice that streamlines for which the maximal overlap is between T_l and T_h will not be assigned any label. This is on purpose, as we do not want to assign a label to streamlines for which it is unclear whether they are invalid or not. These streamlines are removed from the training set, for the purpose of avoiding potential false positives in the classification. The above procedure is repeated for every subject data in the training set.

Using this approach, we create six different training and validation sets using all combinations of threshold parameters $T_l = \{0.70, 0.75, 0.80\}$, $T_h = \{0.85, 0.90\}$. These parameters are selected heuristically. The first 20 subjects of the 30 subjects are used for the training set and the next 5 subjects are used for the validation set, leaving the last 5 subjects for the testing phase. A maximum of 200 streamlines per positive class per subject and 2000 streamlines per negative class per subject are used.

5.1.4 Network Architectures and Training

Since the NRFOD representation proposed in [7] is found to be an expressive feature vector, a simple neural network classifier is used with 3 fully connected layers and ReLU activation functions. The network architecture is illustrated in Figure 5.2. The NRFOD representation of a fiber is a set of orientation histograms calculated at each fiber point and accumulated over multiple directions on an approximately spherical region centered at the given point. NRFOD parameters were set as $K = 50, M = 20, N = 10, h = 6, r = 3$ same as in [7]. Since we have 6 different training sets, as described in Section 5.1.3, we train one classifier using each training set to obtain a total of 6 different classifiers. The networks are implemented in PyTorch⁸, stochastic gradient descent is used for optimization with learning rate 0.001, and momentum 0.9. Loss function is chosen as the cross entropy loss. The 6 classifiers are separately trained for 5 epochs with a batch size of 10 on all the training data. After each epoch, accuracy on the validation set is calculated and the final model of each classifier in the ensemble is selected as the model that achieves the best

⁸pytorch.org

accuracy.

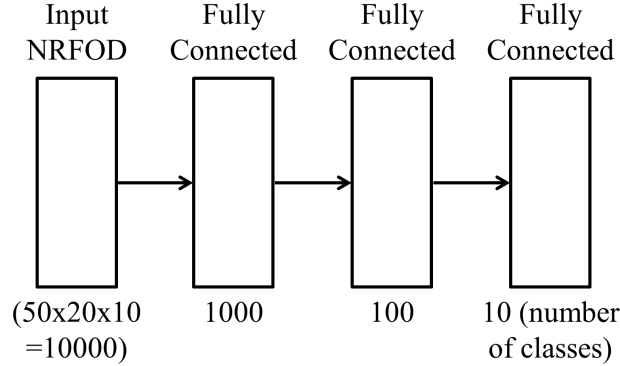


Figure 5.2: *The architecture of the classifiers in the ensemble.*

5.1.5 Testing

The test set consists of streamlines reconstructed from 5 subjects using the automatic ROIs. During the testing phase, we require unanimity from all 6 classifiers on the class assignment of an input streamline for that streamline to be assigned a label of a true fiber bundle. If there is no unanimity, the streamline is considered invalid.

5.2 Results and Discussion

The performance of the proposed method is quantitatively compared to the method in [7] which exemplifies a recent fiber-to-fiber distance based clustering method. Two quantitative measures, Bundle-based Minimum Distance (BMD) [90] and Cohen’s Kappa are used to assess the “closeness” of the bundles created by the automatic methods to the manually created bundles. Since manual bundles are regarded to be the closest approximation to the ground truth, which is unknown, they are used as “ground truth” for comparing automatic methods. For calculation of Cohen’s Kappa values, all bundles are converted to binary volume masks using nearest neighbors. The quantitative comparison results are given in Table 5.1. Visualization of the bundles extracted with the proposed method and the manual method are given in Figure 5.3 for qualitative comparison. In addition, separate visualizations of each bundle, the input set of streamlines and stream-

lines classified as invalid for one subject in the test set are visualized in Figure 5.4. Note that the difference between the input set and streamlines classified as invalid is hard to see in the visualization despite the fact that the input set contains 25000 streamlines and the invalid set contains 12433 streamlines. There are two main reasons for this. One is that small variations of individual streamlines from the true tract are very difficult to see because of the clutter caused by thousands of streamlines. The second reason is that some streamlines may be falsely classified as invalid because the proposed classifier is quite strict with the unanimity requirement from the ensemble. We made this choice because false negatives are not really a problem as long as enough streamlines are classified as valid to reconstruct the tracts with their true thickness. Even one false positive on the other hand, can significantly change the volume of the bundle and is also easily noticeable on the visualization.

Table 5.1: *Quantitative comparison of the proposed method and Ugurlu’s method [7]. Manually created bundles are used as “ground truth” and the mean \pm standard deviation of BMD and Cohen’s Kappa values over the test set between the bundles created by the automatic methods and the manual bundles are given for each positive bundle class. The best results for both measures are highlighted in bold. Note that BMD is a dissimilarity measure and Cohen’s Kappa is a similarity measure, i.e. higher values represent better accuracy for Cohen’s Kappa and lower accuracy for BMD.*

	Proposed_BMD	Ugurlu_BMD	Proposed_Kappa	Ugurlu_Kappa
CST_Left	1.49 \pm 0.28	3.12 \pm 3.62	0.81 \pm 0.03	0.62 \pm 0.22
CST_Right	1.26 \pm 0.22	1.07 \pm 0.23	0.84 \pm 0.01	0.80 \pm 0.02
ML_Left	1.80 \pm 0.58	1.40 \pm 0.47	0.77 \pm 0.02	0.68 \pm 0.11
ML_Right	2.92 \pm 1.76	4.62 \pm 7.37	0.72 \pm 0.13	0.62 \pm 0.14
SCP_Left	4.64 \pm 2.41	6.40 \pm 4.90	0.73 \pm 0.10	0.64 \pm 0.12
SCP_Right	4.43 \pm 1.72	6.67 \pm 5.70	0.71 \pm 0.08	0.63 \pm 0.17
ICP_Left	2.08 \pm 1.76	2.11 \pm 1.23	0.71 \pm 0.08	0.63 \pm 0.14
ICP_Right	1.92 \pm 0.90	1.46 \pm 0.77	0.68 \pm 0.09	0.70 \pm 0.05
MCP	5.46 \pm 2.05	6.19 \pm 1.70	0.74 \pm 0.05	0.73 \pm 0.05

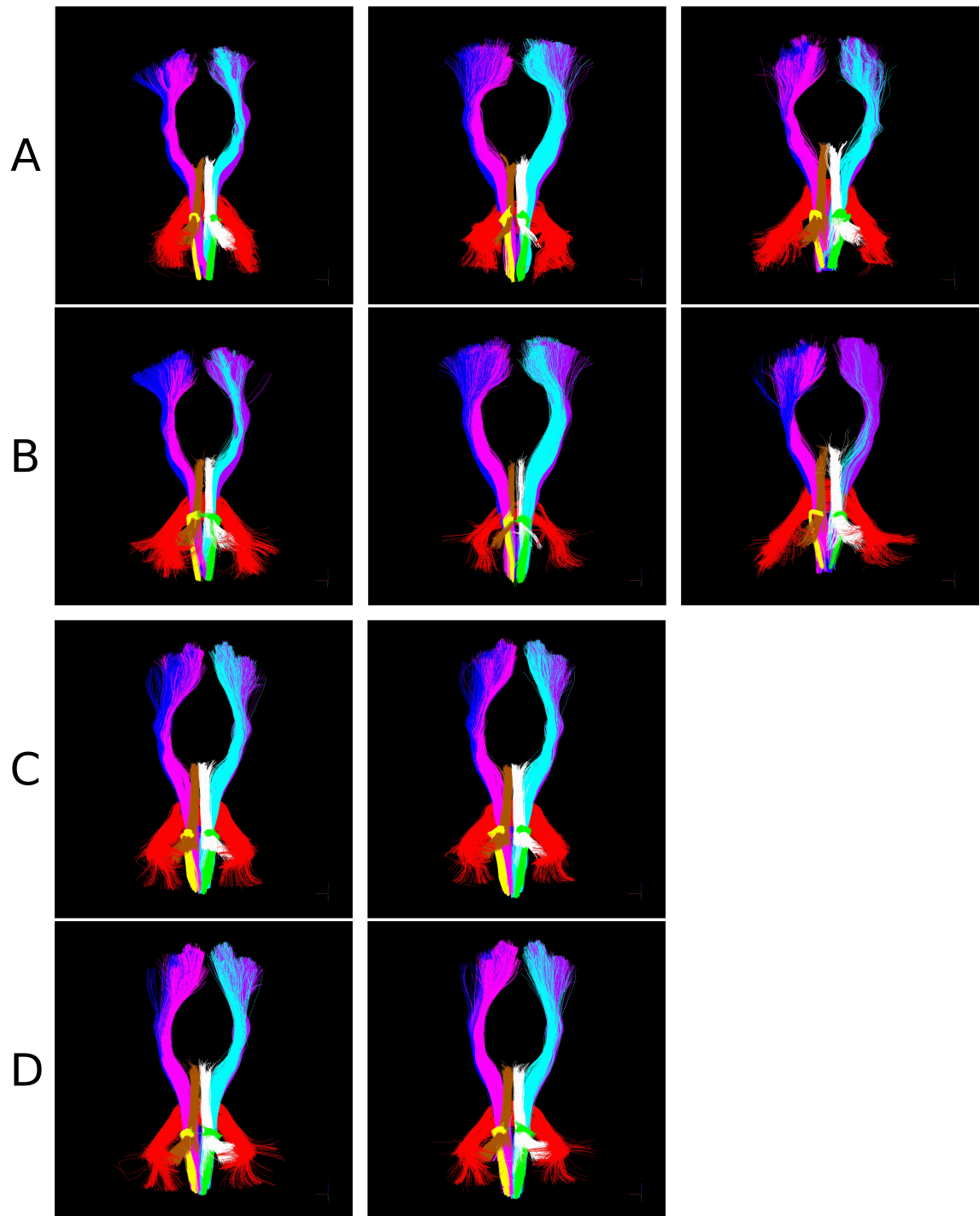


Figure 5.3: Visualization of bundles of interest extracted from the 5 test subjects. A: Manual method for subjects 1-3; B: Proposed method for subjects 1-3; C: Manual method for subjects 4-5; D: Proposed method for subjects 4-5. Tracts are colored according to their bundle label as follows: CST Left: blue; CST Right: purple; ML Left: pink; ML Right: teal; ICP Left: yellow; ICP Right: green; SCP Left: brown; SCP Right: white; MCP: red.

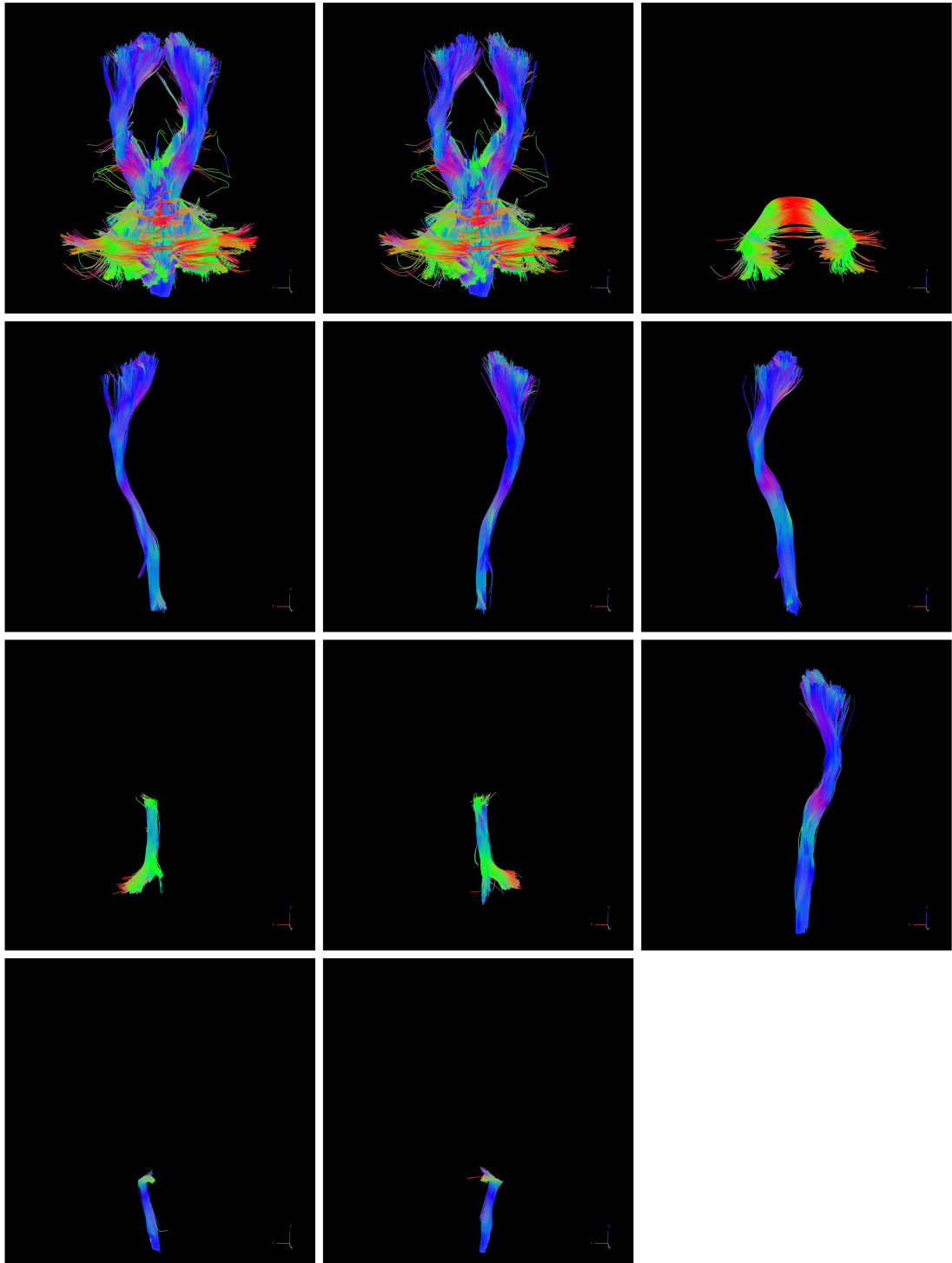


Figure 5.4: *Visualization of input streamlines and results of the proposed method on one subject in the test set. In top-bottom, left-right order: The input set of streamlines created with the automatic ROIs; invalid streamlines; MCP; left CST; right CST; left ML; left SCP; right SCP; right ML; left ICP; right ICP.*

Despite the simplicity of the proposed method, it generally outperforms a recent state-of-the-art fiber classification method based on clustering with respect to the quantitative measures. Moreover, visual comparison with manually created bundles indicate that the proposed method indeed usually produces anatomically meaningful classifications. Since the proposed method does not require pairwise fiber-to-fiber distances unlike most previous clustering approaches, it is faster on the online classification phase in comparison and scales better with increasing number of fibers in the input set. These results have two important implications: i) classical supervised classification approach is suitable for the fiber classification task and should be investigated further. ii) Representing a fiber based on the orientation distributions in its neighborhood is a powerful approach that allows robust comparison of fibers extracted from different subject spaces.

5.3 Conclusion

We presented a novel fiber classification method that applies the classical supervised classification approach, which maps an input vector to class probabilities, to the fiber classification task. The proposed method quantitatively outperformed a recent exemplary fiber clustering method, and was also shown to be visually satisfactory. The proposed training set creation method that includes labeling a wide variety of invalid streamlines, combined with the ensemble of networks that utilizes the created training sets; (i) works in disfavor of false positives; (ii) allows the usage of bundles constructed by a routine manual extraction without requiring any extra manual effort. This makes it easier to extend the training data to include more subjects and more bundle classes in the future. Future work involves comparing the proposed method to a greater variety of other methods in literature and for more classes of tracts. Furthermore, one direction our work will be extended is to train deeper networks that directly use the orientation information in the ODF volume, rather than use the NRFOD feature vector.

Chapter 6

Analysis of Structural Changes on Major White Matter Fiber Pathways Passing Through The Brainstem Between Pre-Operative and Post-Operative Diffusion MRI Images For Patients With Brainstem Lesions⁹

In this chapter, we present a clinical application of fiber tractography and classification. The CST and ML bundles of patients are extracted prior to and after a tumor resection operation and various measures that aim to quantify the structural change between the pre-op (pre-operative) and post-op (post-operative) bundles are computed. Statistical analysis is performed to see whether some of the proposed measures can predict the clinical outlook of the patient. Pre-op and post-op DMRI spaces are rigid registered to the MNI152

⁹The contents of this chapter were included in the project report of our TUBITAK Project No. 112E320.

standard space before the measures are computed.

6.1 Measures that are not Based on a Deformation Field

The measures introduced in this section do not require a deformation field to be estimated between the pre-op and post-op bundles. Some of these measures computed from 8 subjects in our dataset were published in [93].

6.1.1 Translation of Center of Mass (NDM1)

Let \mathbf{x} denote a point on a tract in standard space and Ω , the set of all points on all tracts belonging to a certain bundle. The center of mass is then given by

$$\mathbb{E}(\Omega) = \sum_{\mathbf{x} \in \Omega} \frac{1}{|\Omega|} \mathbf{x} \quad (6.1)$$

where $|\Omega|$ is the number of points in the bundle. The first non-deformation measure (NDM1) is simply the difference between the center of mass of two bundles (pre-op and post-op reconstruction of the same bundle):

$$\text{NDM1}(\Omega_1, \Omega_2) = \|\mathbb{E}(\Omega_1) - \mathbb{E}(\Omega_2)\|_2. \quad (6.2)$$

6.1.2 Change in Principal Direction (NDM2)

The principal direction of a bundle is extracted using principal component analysis. The covariance matrix \mathbf{C} of a bundle is computed as follows:

$$\mathbf{C} = \sum_{k=1}^{|\Omega|} (\mathbf{x}_k - \mathbb{E}(\Omega)) (\mathbf{x}_k - \mathbb{E}(\Omega))^T. \quad (6.3)$$

\mathbf{C} is a symmetric positive-definite matrix and can be diagonalized using singular value decomposition:

$$\mathbf{C} = \mathbf{U}\mathbf{\Lambda}\mathbf{U}^T \quad (6.4)$$

where \mathbf{U} is the eigenvector matrix and $\mathbf{\Lambda}$ is the diagonal eigenvalue matrix. The angular difference between the principal eigenvectors $\mathbf{u}_1, \mathbf{u}_2$ of two bundles is chosen as a measure:

$$\text{NDM2}(\mathbf{u}_1, \mathbf{u}_2) = 1 - \frac{\mathbf{u}_1 \cdot \mathbf{u}_2}{\|\mathbf{u}_1\| \|\mathbf{u}_2\|}. \quad (6.5)$$

6.1.2.1 Orientation Histograms in Spherical Coordinates (NDM3)

For all tracts, the local orientation of the tract on each point is calculated. The orientation is the difference between two consecutive points. The difference vector has x, y, z coordinates in Cartesian space. Since we are interested in orientation, not direction, the vectors for which the sign of z coordinate is negative are multiplied by -1 . After that, the vector is transformed to spherical coordinates. The length of the vectors are not important so each orientation vector can be represented with two parameters θ and ϕ where θ is the polar angle (colatitude) and ϕ is the azimuthal angle. In order to empirically determine the probability distribution of all orientations in a bundle, the range of θ , $([0, 2\pi])$, is divided into 36 bins of 10° and similarly, the range of ϕ , $([0, \pi])$, is divided into 9 bins of 20° . Then, the appropriate bin is incremented for each orientation to compute a histogram \mathcal{H} , which is a 36×9 matrix. The L_2 distance between two histograms gives the third measure:

$$\text{NDM3}(\Omega_1, \Omega_2) = \sqrt{\sum_{\theta, \phi} \mathcal{H}(\theta, \phi)_1 - \mathcal{H}(\theta, \phi)_2)^2} \quad (6.6)$$

6.1.3 Local Mean Orientation Maps (NDM4, NDM5)

Unlike orientation histograms that are a global representation of orientations, orientation probability maps are local representations. For each voxel, the mean of all local orientations on that voxel of all fibers passing through the voxel is computed and normalized so that it has length 1. Three maps of mean local orientations are created from the (x, y, z) components and smoothed with a Gaussian filter. Two measures are defined based on these maps. The first is computed by summing the cosine distances between mean orientation vector pairs in all voxels in the brainstem region (Ω_{BS}) where the cosine distance is defined as $((1 - \cos(\mathbf{v}_1, \mathbf{v}_2)))$ where \mathbf{v} is the mean orientation vector on voxel \mathbf{x} .

$$NDM4(\Omega_1, \Omega_2) = \sum_{\mathbf{x} \in \Omega_{BS}} \left(1 - \cos(\mathbf{v}_1(\mathbf{x}), \mathbf{v}_2(\mathbf{x})) \right) = \sum_{\mathbf{x} \in \Omega_{BS}} \left(1 - \frac{\mathbf{v}_1(\mathbf{x}) \cdot \mathbf{v}_2(\mathbf{x})}{\|\mathbf{v}_1(\mathbf{x})\| \cdot \|\mathbf{v}_2(\mathbf{x})\|} \right). \quad (6.7)$$

The second measure is computed by summing the correlation distances between mean orientation vector pairs in all voxels in the brainstem region (Ω_{BS}):

$$NDM5(\Omega_1, \Omega_2) = \sum_{\mathbf{x} \in \Omega_{BS}} \left(1 - \frac{(\mathbf{v}_1(\mathbf{x}) - \overline{\mathbf{v}_1(\mathbf{x})})(\mathbf{v}_2(\mathbf{x}) - \overline{\mathbf{v}_2(\mathbf{x})})'}{\sqrt{(\mathbf{v}_1(\mathbf{x}) - \overline{\mathbf{v}_1(\mathbf{x})})(\mathbf{v}_1(\mathbf{x}) - \overline{\mathbf{v}_1(\mathbf{x})})'} \sqrt{(\mathbf{v}_2(\mathbf{x}) - \overline{\mathbf{v}_2(\mathbf{x})})(\mathbf{v}_2(\mathbf{x}) - \overline{\mathbf{v}_2(\mathbf{x})})'}} \right) \quad (6.8)$$

where the prime denotes the transpose.

6.1.4 Measures Based on Symmetry Axis (NDM6, NDM7)

The ROSA curve-skeleton [94] is a 1D symmetry axis model that can be computed from a point cloud. In order to compute the skeletons of bundles, they are first converted to tract density maps where each voxel's intensity is determined by the number of points the bundle has on that voxel. The tract density map is then smoothed with a Gaussian filter and thresholded. The points on the surface are then pulled to the symmetry axis by iteratively using the Laplace operator.

The first measure derived from the symmetry axis is the Hausdorff distance between two bundles:

$$NDM6(A, B) = \max \left\{ \sup_{\mathbf{a} \in A} \inf_{\mathbf{b} \in B} d(\mathbf{a}, \mathbf{b}), \sup_{\mathbf{b} \in B} \inf_{\mathbf{a} \in A} d(\mathbf{a}, \mathbf{b}) \right\} \quad (6.9)$$

where A and B denote the set of points defining the symmetry axis for the two bundles and $d(\mathbf{a}, \mathbf{b})$ is the Euclidean distance between points \mathbf{a} and \mathbf{b} . Hausdorff distance is the largest of the smallest distances from each point on one set to all other points in another set so it is sensitive to local changes on the bundle's symmetry axis.

The second symmetry axis based measure is the distance between log-polar histograms that are derived from the symmetry axes. Shape Context ([95]) is a popular shape analysis method that creates log-polar histograms centered around sampled points from a shape. We create log-polar histograms $\mathcal{S}^i(\theta, \phi, \log(r))$ for all symmetry axis points \mathbf{x}_i . 15 bins

are used for θ , 15 bins for ϕ and 10 bins for $\log(r)$ for a total of 2250 bins. The measure NDM7 is defined as the sum of all L_2 distances between histograms:

$$NDM7(\mathcal{S}_1, \mathcal{S}_2) = \sum_{i=1}^N \|\mathcal{S}_1^i - \mathcal{S}_2^i\|_2 \quad (6.10)$$

where N is the number of points on the symmetry axis.

6.1.5 Dice Score (NDM8)

The dice score is a simple but popular measure of volumetric overlap between two volumes. The dice score between the volumes Ω_1 and Ω_2 corresponding to a pair of pre-op and post-op bundles is calculated as

$$Dice(\Omega_1, \Omega_2) = \frac{2|\Omega_1 \cap \Omega_2|}{|\Omega_1| + |\Omega_2|} \quad (6.11)$$

where $|\cdot|$ denotes the number of voxels in a volume.

6.1.5.1 Spectral Distance (NDM9)

Spectral distance (ShapeDNA) [96], is computed from the eigenvalues of the Laplace-Beltrami operator:

$$\Delta_\Omega = \sum_{i=1}^3 \frac{\partial^2}{\partial x_i^2} \quad (6.12)$$

where \mathbf{x} is a point in Ω and i is the dimension index. The eigenvalues and eigenvectors of the Laplace operator are the solutions of the Helmholtz equation with Dirichlet boundary condition:

$$\begin{aligned} \Delta f + \lambda f &= 0 \\ f(x)|_{x \in \partial\Omega} &= 0. \end{aligned} \quad (6.13)$$

where $\lambda \in \mathbb{R}$ are eigenvalues and an infinite number of eigenvalues can be computed. The ordered eigenvalue series $\lambda_1 < \lambda_2 < \lambda_3 < \dots$, is known as the Dirichlet spectrum of Δ_Ω . The spectrum contains information about the geometry of Ω . The Dirichlet spectrums of two different shapes can be used to derive a distance measure between the shapes. In our implementation, the Laplace operator is constructed using 6-neighborhood and the first

150 elements of the eigenvalue series are used. The L_2 distance between the two spectra gives the measure:

$$NDM9(\lambda^{\Omega_1}, \lambda^{\Omega_2}) = \left(\sum_{n=1}^N (\lambda_n^{\Omega_1} - \lambda_n^{\Omega_2})^2 \right)^{\frac{1}{2}} \quad (6.14)$$

6.1.6 Screened Poisson Hyperfields (NDM10)

Screened Poisson hyperfields [97] is a shape representation method that is based on the screened Poisson equation:

$$\begin{aligned} \Delta v^{\rho_i}(\mathbf{x}) - \frac{v^{\rho_i}(\mathbf{x})}{\rho_i^2} &= 0 \\ v^{\rho_i}(\mathbf{x})|_{\mathbf{x} \in \partial\Omega} &= 1. \end{aligned} \quad (6.15)$$

where ρ is a parameter that governs the nature of diffusion or random walk from the shape boundaries into the shape center via the Laplace operator. When ρ is small, the solution v field contains local shape information near the boundary, when ρ is large, it captures more global shape properties. Screened Poisson hyperfields are obtained by solving (6.15) for all $(\mathbf{x} \in \Omega)$ for various values of ρ^2 , in other words, the hyperfield $v_{i=1\dots N}^{\rho_i}$ is obtained by screening the ρ^2 space. The hyperfield can be represented by a 2-dimensional matrix $Y_{|\Omega| \times N}$ as follows:

$$Y_{|\Omega| \times N} = \begin{bmatrix} v^{\rho_1}(\mathbf{x}_1) & v^{\rho_2}(\mathbf{x}_1) & \dots & v^{\rho_N}(\mathbf{x}_1) \\ v^{\rho_1}(\mathbf{x}_2) & v^{\rho_2}(\mathbf{x}_2) & \dots & v^{\rho_N}(\mathbf{x}_2) \\ \vdots & \vdots & & \vdots \\ v^{\rho_1}(\mathbf{x}_{|\Omega|}) & v^{\rho_2}(\mathbf{x}_{|\Omega|}) & \dots & v^{\rho_N}(\mathbf{x}_{|\Omega|}) \end{bmatrix}. \quad (6.16)$$

In order to achieve a more compact representation, the Y matrix is projected onto a lower-dimensional space using Principal Component Analysis. The eigenvectors $\Phi_j, j = 1, \dots, d$ of the covariance matrix of Y are calculated by diagonalization as $Y^T Y = \Phi \Lambda \Phi$. Y is then projected onto the eigenvectors using $\mathcal{P}_j = Y \Phi_j$. We empirically chose to keep the first $d = 6$ eigenvectors as they seemed to contain most of the shape information. The resulting representation is insensitive to isometric deformations and global scale. In order to reduce the data size, the method proposed in [98] is used. A representative set of

points $\mathcal{C} = \{\mathbf{c}_1, \dots, \mathbf{c}_k\}$ where $\mathbf{c}_i \in \mathbb{R}^d$ and $k = 32$ are first chosen as cluster centers using k-means clustering. The projections of all points on the shape are then assigned to the nearest cluster center. Then, the difference vectors $\mathcal{P}(\mathbf{x}) - \mathbf{c}_i$ are summed to obtain a residual vector each cluster center:

$$\mathbf{R}_i = \sum_{\mathbf{x} \in \Omega: \mathcal{NN}_{(\mathbf{x})} = \mathbf{c}_i} \mathcal{P}(\mathbf{x}) - \mathbf{c}_i. \quad (6.17)$$

where $\mathcal{NN}_{(\mathbf{x})} = \mathbf{c}_i$ means the nearest cluster center to \mathbf{x} is \mathbf{c}_i . Finally, using these residual vectors, a shape distance measure between the pre-op and post-op bundle shapes is defined as the sum of L_1 distances between corresponding residual vectors:

$$NDM10(\mathbf{R}^1, \mathbf{R}^2) = \sum_i \|(\mathbf{R}_i^1 - \mathbf{R}_i^2)\|_1. \quad (6.18)$$

6.2 Fiber Bundle Registration

Before we can derive measures based on a deformation field that relates the pre-op and post-op bundles, the deformation field should first be estimated. This is the topic of this section. Our approach is to formulate the problem as a deformable volumetric registration of orientation fields derived from tractography results and solve the registration problem using a Markov Random Field (MRF) model. Since we want to quantify the deformation between the pre-op and post-op state of a bundle, the pre-op and post-op DMRI spaces are first affine registered. Then, two corresponding bundles are converted to binary volume masks and the orientation fields are defined on these masks. For each voxel in a mask, the principal direction of the diffusion tensor is assigned as the orientation of the fiber bundle.

6.2.1 Formulation of the Deformable Registration Problem

Let us make the following definitions:

- T is the set of coordinates on which the pre-op diffusion images are defined.
- $V = \{\mathbf{v}^1, \mathbf{v}^2, \dots, \mathbf{v}^m\} \subset T$, is the set of coordinates that are included in the binary mask for the pre-op bundle.

- $U = \{\mathbf{u}^1, \mathbf{u}^2, \dots, \mathbf{u}^n\} \subset T$, is the set of coordinates that are included in the binary mask for the corresponding post-op bundle.

Next, let us define the orientation fields for the bundles as: $I_{vec} : V \rightarrow W$, $J_{vec} : U \rightarrow W$ where $\mathbf{w} \in W \subset \mathbb{R}^3$ such that $\|\mathbf{w}\| = 1$. The vector \mathbf{w} represents the fiber orientation in a voxel. In Figure 6.1, V, U and an axial slice of I_{vec} and J_{vec} corresponding to the right ML are illustrated on one of the subjects.

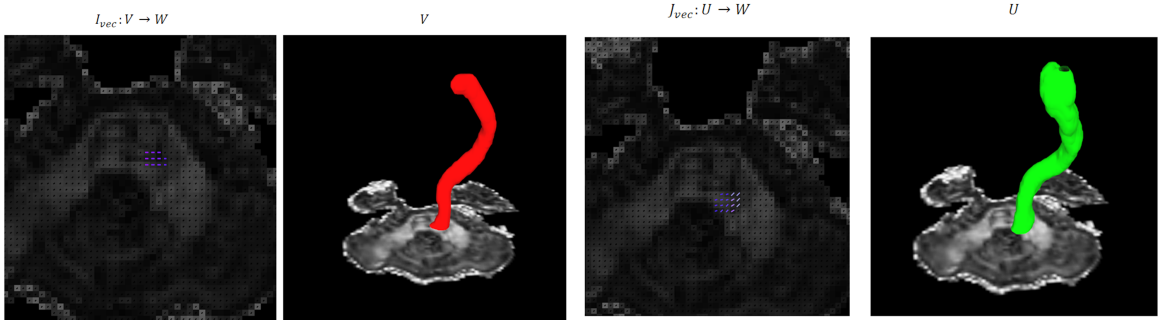


Figure 6.1: V (red), U (green) volumes depicting the binary mask of pre-op and post-op ML right bundle of a subject and an axial slice of corresponding orientation fields I_{vec} and J_{vec} . FA values are used as background intensity and the orientation field is shown as colored lines on voxels on which they are defined. On voxels where the orientation field is undefined, black lines are used.

In addition to the orientation fields, let us also define two scalar volumes as $I_{sca} : V \rightarrow C$ and $J_{sca} : U \rightarrow C$ where C is the interval $(0, 255]$. The I_{sca} and J_{sca} volumes are created such that they take high values near the center of a fiber bundle and low values near the border of a bundle. An example axial slice of these scalar volumes is shown in Figure 6.2.

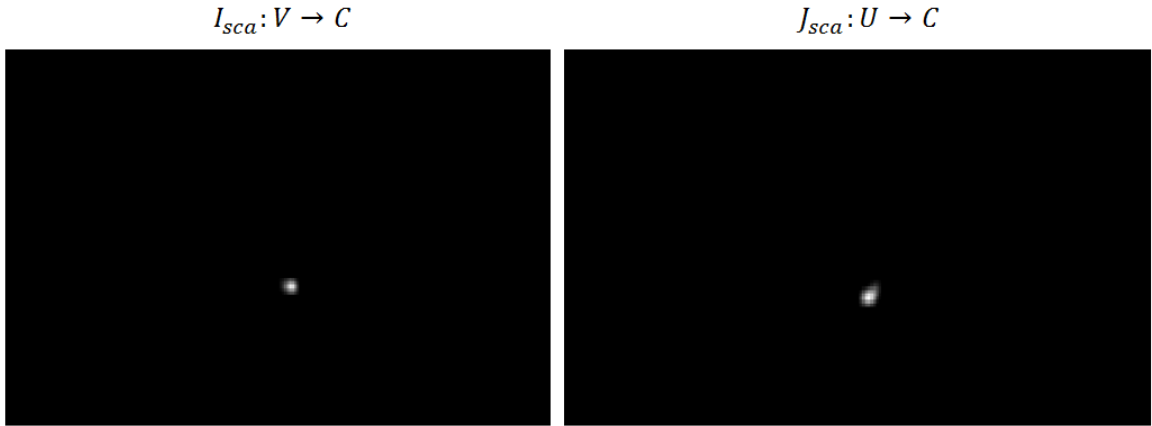


Figure 6.2: *An axial slice from the I_{sca} and J_{sca} volumes.*

In order to represent the deformation field in a Markov Random Field (MRF) framework, let $D = \{\mathbf{d}^1, \mathbf{d}^2, \dots, \mathbf{d}^i\}$ be the discrete deformation space and $L = \{l^1, l^2, \dots, l^i\}$ be a label set that has a one-to-one correspondence with D . Let us then define a function $f : V \rightarrow L$ that assigns a label to each possible \mathbf{v} . The deformation model with these definitions is illustrated in Figure 6.3.

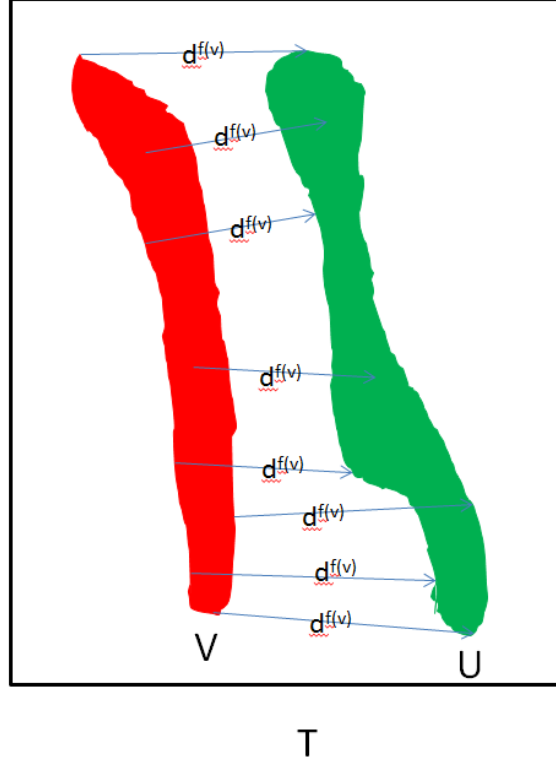


Figure 6.3: *Illustration of the deformation model. Red: pre-op bundle mask; Green: post-op bundle mask.*

Let us now define an undirected graph $G = (V, \mathcal{E})$ which represents the volume V and its neighborhood system. In the MRF framework, an energy function that we want to minimize is then defined as follows:

$$E(f) = \sum_{\mathbf{v} \in V} H_v(f(\mathbf{v})) + \sum_{\mathbf{v} \in V} \sum_{\mathbf{v}\mathbf{q} \in \mathcal{E}} H_{vq}(f(\mathbf{v}), f(\mathbf{q})) \quad (6.19)$$

The first term is a data-based term known as the unary potential and measures how well the labeling fits the data. The second term, which is known as a pairwise potential, is a regularization term that imposes a smoothness constraint on the deformation field.

We defined the unary potential as

$$H_v(f(\mathbf{v})) = \begin{cases} 510 & : \mathbf{v} + \mathbf{d}^{f(\mathbf{v})} \notin U \\ \|J_{sca}(\mathbf{v} + \mathbf{d}^{f(\mathbf{v})}) - I_{sca}(\mathbf{v})\| + 255(1 - J_{vec}(\mathbf{v} + \mathbf{d}^{f(\mathbf{v})}) \cdot I_{vec}(\mathbf{v})) & : \mathbf{v} + \mathbf{d}^{f(\mathbf{v})} \in U \end{cases} \quad (6.20)$$

This unary potential has the following meaning: When a point v is translated with $d^{f(v)}$, we want the destination it reaches to be an element of U , the difference between corresponding values on the scalar volume to be small and the angle between the corresponding orientation vectors to be small. The pairwise potential is chosen as

$$H_{vq}(f(\mathbf{v}), f(\mathbf{q})) = \lambda \frac{\|\mathbf{d}^{f(\mathbf{v})} - \mathbf{d}^{f(\mathbf{q})}\|^2}{\|\mathbf{v} - \mathbf{q}\|^2}. \quad (6.21)$$

and the neighborhood system in (6.19) is defined as

$$\mathcal{E} = \{(\mathbf{v}, \mathbf{q}) | \mathbf{v}, \mathbf{q} \in V, \|\mathbf{v} - \mathbf{q}\| \leq 6\text{mm}\}. \quad (6.22)$$

As can be inferred from (6.21 and 6.22), increasing λ can be seen as strengthening the bonds that hold the volume together. Hence, if fragmentation is observed on the volume, λ should be increased. Conversely, if the deformation is too small for the volume to fit the target volume, λ should be decreased.

6.2.2 Solution of the Deformation Model

Equation (6.19) is a general first order MRF model and the method proposed in [99] and [100] is used to solve it after integrating our own unary and pairwise potential definition. The total deformation field was calculated in three iterations. In the first iteration, the deformation space was defined in the ± 18 range with a step size of 3 voxels, in the second iteration, ± 6 voxel range with a step size of 1 voxel and in the final iteration, ± 1 voxel range with a step size of 0.2 voxels. The total deformation is given by the sum of deformations in the first 3 steps. $\lambda = 8$ was empirically chosen.

6.3 Measures based on the Deformation Field

In this section, measures derived from the estimated deformation field between corresponding pre-op and post-op bundles are presented. Here, $V = \{\mathbf{v}^1, \mathbf{v}^2, \dots, \mathbf{v}^m\}$ is the intersection of the bundle binary volume mask with the brainstem region and $D = \{\mathbf{d}^1, \mathbf{d}^2, \dots, \mathbf{d}^m\}$ are the corresponding deformation vectors at each coordinate of V .

6.3.0.1 Mean Deformation Magnitude (DM1)

This measure is simply the mean of the magnitudes of deformation vectors:

$$DM1(D) = \frac{\sum_{i=1}^m \|\mathbf{d}^i\|}{m}. \quad (6.23)$$

6.3.0.2 Mean of the Invariants of the Lagrange Strain Tensor (DM2, DM3, DM4)

Largrange strain tensor is used in mechanics as a measure of how different a deformation is compared to rigid transformation. It is defined as

$$\mathbf{E} = \frac{1}{2} [(\nabla_x \mathbf{d}^T) + \nabla_x \mathbf{d} + (\nabla_x \mathbf{d}^T) \cdot (\nabla_x \mathbf{d})], \quad (6.24)$$

or in index notation,

$$e_{ij} = \frac{1}{2} (d_{j,i} + d_{i,j} + d_{k,i}d_{k,j}) \quad (6.25)$$

where \mathbf{d} is the deformation field [101]. The invariants of a tensor, I_1, I_2, I_3 , are calculated as follows:

$$I_1(\mathbf{E}) = tr(\mathbf{E}) = E_{ii} \quad (6.26)$$

$$I_2(\mathbf{E}) = \frac{1}{2} [(\mathbf{E} \cdot \mathbf{I})^2 - (\mathbf{E} \cdot \mathbf{E}^T)] = \frac{1}{2} [(E_{ii}^2) - E_{ij}E_{ji}] \quad (6.27)$$

$$I_3(\mathbf{E}) = det(\mathbf{E}). \quad (6.28)$$

where $det()$ is the determinant operator and the index notation includes Einstein summation. Lagrange strain tensor invariant were used as a measure of brain deformation for tumor patients in [102], however were not used as fiber deformation measures before.

For every voxel on which the deformation field is defined, the Lagrange strain tensor \mathbf{E}^i and its invariants I_1^i, I_2^i, I_3^i are calculated and the mean of their absolute values are used as measures of deformation between pre-op and post-op bundles:

$$DM2 = \sum_{i=1}^m \frac{\|I_1^i\|}{m} \quad (6.29)$$

$$DM3 = \sum_{i=1}^m \frac{\|I_2^i\|}{m} \quad (6.30)$$

$$DM4 = \sum_{i=1}^m \frac{\|I_3^i\|}{m}. \quad (6.31)$$

6.4 Results and Discussion

6.4.1 Clinical Dataset

The clinical dataset consists of pre-op and post-op MRI and DMRI images and clinical evaluations of 30 subjects from Yeditepe University Hospital. 3D T1 TFE (Turbo field echo) and DTI data acquisition of were performed on a 3T MR scanner (Philips Ingenua, Netherlands) with 16 channel head coil. 3D T1 TFE was acquired on a sagittal plane using a TR/TE 99/4.5ms, FA 8, TI 1000ms, image matrix 300x768, slice thickness 0.8mm, gap 0mm, acquisition time 6 minutes. DTI was acquired on axial plane, using TR/TE 3440/93ms, EPI factor 45, image matrix 90x128, slice thickness 2.5mm, gap 0mm. 16 diffusion directions at $b = 800\text{s/mm}^2$ were acquired in addition to $b = 0$ images (B0), acquisition time 7 minutes. One set of images are taken before the tumor resection operation and another set of images are taken 2 months after the operation. The clinical evaluation data consists of tumor degrees and neurological performance scores. The performance scores are the Karnofsky performance scale (KPS) [103] and Zubrod performance scale [104]. KPS score takes a value between 0 (dead) and 100 (normal, healthy), and Zubrod score takes a value between 0 (normal, healthy) and 5 (dead). The tumor degree is the degree defined by the World Health Organization [105]. The degree changes from 1 to 4, where 4 indicates a very aggressive and malignant tumor. This study was approved by the Ethics Review Committee of Yeditepe University Hospital (YUH).

It should be noted that in the dataset, only one of the patients had worse performance scores after the operation compared to before. This is caused by the fact that the operation is only approved when there is a high likelihood that the patient's condition will improve as a result of the operation. The lack of data with patients whose condition worsen after the operation must be considered when performing statistical analysis.

6.4.2 The Values of Measures

All the measures described in Sections 6.1 and 6.3 are calculated for each patient's left and right CST and ML. These values are reported in Figures 6.4, 6.5, 6.6 and 6.7 and the

sum of the measures for the four bundles in consideration are reported in Figure 6.8.

Subject No.	DM1	DM2	DM3	DM4	NDM1	NDM2	NDM3	NDM4	NDM5	NDM6	NDM7	NDM8	NDM9	NDM10
1	3.3311333	0.1672086	0.0323391	0.0010234	0.6744535	0.0013973	0.1406984	0.3536704	0.3929317	2.6042031	0.1493335	0.2269933	0.9042091	0.5109579
2	1.7951141	0.1643075	0.0145233	0.000354	2.6147998	0.0017747	0.1939046	0.9673125	1.0857569	3.752908	0.4205325	0.6249955	0.1751146	0.6082367
3	6.2595013	0.5712244	0.2158392	0.0050828	6.5897154	0.0174265	0.2893106	1.692549	1.8734025	9.9452078	0.7780932	0.5460972	0.1502418	0.8839975
4	2.4970675	0.1265847	0.0142101	0.000287	1.2554254	9.744E-05	0.058108	0.33325	0.3740791	5.056253	0.2310396	0.2267434	0.1163423	3.2890868
5	3.5588033	0.2256046	0.03295	0.0006729	10.928245	0.0046447	0.1717636	1.3094968	1.3999733	18.144437	0.5975824	0.6536812	6.9652	4.0534446
6	3.3490268	0.2487313	0.0401446	0.0011228	1.4302506	0.0023506	0.1496657	0.7553033	0.8361299	3.4054257	0.3461499	0.5414401	1.3221536	3.7054507
7	5.1307911	0.4359975	0.1457593	0.004966	3.8194175	0.00334	0.208767	1.1965475	1.3201179	6.8981553	0.4719971	0.3004473	0.1469845	2.7663258
8	4.8197498	0.2150027	0.0505621	0.0028042	1.365441	0.0014791	0.1764375	0.3331464	0.3751378	2.8707617	0.2328348	0.3383167	0.5930744	2.5992389
9	4.8515121	0.475137	0.1289851	0.0054644	4.7583006	0.0016753	0.2353938	1.7655798	1.939489	6.6190829	0.7116119	0.7448761	2.1694639	2.7315336
10	4.2957774	0.308814	0.0490365	0.0008078	2.4075074	0.0071204	0.2242129	1.0067683	1.0580103	4.9014449	0.5230528	0.4822159	3.5643323	3.052323
11	2.6279742	0.165118	0.0173744	0.0005364	16.94026	0.0274027	0.1893436	2.6101922	2.6407928	41.645508	1.7760855	0.8123732	3.7657831	6.0256761
12	5.2224278	0.4586285	0.1076548	0.0051581	4.1287382	0.0015237	0.28592	1.6771679	1.6539095	8.6224652	0.3925549	0.6601434	0.4618273	4.602066
13	6.4975462	0.3896309	0.1116801	0.0055082	1.2392791	0.0051061	0.2983757	0.932376	1.0102733	6.8272058	0.4380693	0.7487273	1.6230126	5.418978
14	5.9085837	0.270623	0.0746167	0.0031813	0.6467542	0.0005192	0.2593508	0.5578701	6.241	15.757082	0.2386074	0.6013675	0.2486018	1.527841
15	3.6988047	0.2424243	0.0494751	0.0021859	8.9184275	0.0164974	0.1964057	0.7613296	0.8145756	7.1530271	0.7322332	0.4089484	0.1942791	7.1157568
16	3.0490545	0.1714574	0.0225455	0.0008479	4.8819707	0.0039895	0.1460235	1.4496743	1.5779432	5.9749605	0.7926487	0.8687931	0.1150734	4.1196356
17	2.7676029	0.2405294	0.0371863	0.0008219	4.592214	0.0076553	0.227105	1.4634677	1.5917441	6.4703022	0.5560411	0.7743349	2.2410494	4.1496348
18	5.1548887	0.23743	0.0346852	0.0001736	19.398233	0.0597272	0.3496076	3.0563069	3.0712217	28.601415	1.7837018	0.6381572	1.3181495	5.6231005
19	12.187782	0.3811677	0.2237039	0.0074598	2.6459741	0.0012005	0.1696027	0.5596746	0.646206	3.6884491	0.254985	0.4683348	0.1483119	2.5765241
20	9.5260591	0.8367805	0.3803419	0.0158159	7.0170078	0.0273448	0.3159425	1.3679953	1.4643182	12.042558	0.7520249	0.6793758	1.9478495	2.709678
21	5.0358585	0.4067644	0.1201604	0.0031886	2.7089559	0.0037394	0.1884371	0.9607243	1.0235611	5.6538372	0.4445346	0.4811733	0.3017263	2.1052816
22	2.8671002	0.1059663	0.0123471	0.0002855	0.4489534	0.061E-05	0.1701046	0.2552627	0.2851424	1.872808	0.1272734	0.3752859	0.3287005	2.3711334
23	3.0773393	0.1505443	0.0241914	0.0009646	3.3343182	0.0021389	0.1404329	1.0594047	1.2057044	5.1400711	0.5692245	0.6088338	1.4607751	2.9616366
24	2.6917999	0.1012331	0.0133338	0.0004907	0.9616087	0.000869	0.0952026	0.3176363	0.3657255	2.0187505	0.2463394	0.3763785	1.9701169	5.5355732
25	4.7540326	0.2601744	0.0507532	0.0017744	4.6083343	0.020616	0.3701734	0.8956291	0.9147801	5.5619365	0.8584177	0.2924743	0.2486324	2.7668712
26	1.695581	0.1425271	0.0163476	0.000389	1.3563341	0.0015568	0.1258263	0.442963	0.5024052	3.3000564	0.2479571	0.5019318	0.4662079	4.707713
27	0.4674345	0.0304647	0.0015227	1.993E-05	0.5479564	4.774E-05	0.0343367	0.0733195	0.0794593	1.1927256	0.1146858	0.0431034	0.2683199	0.5084987
28	5.1365	0.1711885	0.037576	0.0021657	3.0188166	0.0005607	0.1912119	0.7618405	0.8094576	4.1413114	0.4037289	0.5474801	0.5446876	0.2841601
29	4.9540156	0.2159493	0.0493319	0.0019018	1.6206063	0.0014646	0.1687442	0.5424486	0.5571311	4.459875	0.2955228	0.3175535	1.0078388	5.8262244
30	2.8299047	0.2696309	0.0447726	0.000972	5.5461674	0.0099124	0.1308256	1.7527986	1.8277338	7.2188838	0.9822566	0.3866219	1.0966611	4.3456881

Figure 6.4: All measures for the left CST of subjects. DM 1-4 are the measures based on a deformation field and NDM1-10 are the measures that do not require estimation of a deformation field.

Subject No.	DM1	DM2	DM3	DM4	NDM1	NDM2	NDM3	NDM4	NDM5	NDM6	NDM7	NDM8	NDM9	NDM10
1	1.4548011	0.0997062	0.0096138	0.0002493	0.9341163	0.000179	0.1159563	0.1468967	0.1558229	2.4082645	0.13228	0.1860822	0.6209754	4.3344299
2	1.8193792	0.1244641	0.0104153	3.955E-05	1.6163393	0.0006935	0.1464994	0.8588715	0.9516346	12.669291	0.3054285	0.4381484	0.2871092	3.88633
3	3.088303	0.2009657	0.0327186	0.0010287	3.3279415	0.0055485	0.237814	1.0477151	1.1144808	5.4570446	0.6093032	0.3783991	2.2176994	3.7088577
4	1.507072	0.127135	0.0094827	0.0002662	1.7809457	1.274E-05	0.1011526	0.665862	0.7102833	3.8997242	0.4657299	0.3931768	1.9253863	3.8211159
5	5.4315589	0.1628252	0.0417766	0.0015979	7.1008166	0.0065047	0.2234009	1.5440062	1.6059503	7.4750524	0.7752717	0.654874	1.927137	5.9831548
6	4.8835161	0.3344615	0.0757343	0.0020572	2.436048	0.0042691	0.1549635	0.7339461	0.8139291	4.0881232	0.4324924	0.4964047	1.2036039	4.1395432
7	4.5847158	0.4111428	0.1327324	0.0035088	4.9178465	0.001058	0.2478546	1.4377378	1.5296428	6.8220084	0.573337	0.301223	0.1249088	1.869322
8	1.3662319	0.0832987	0.0067219	0.0001385	0.6106242	0.0001052	0.1029515	0.1656798	0.176009	2.5541412	0.1361505	0.1086606	0.1086563	0.3305522
9	5.0407873	0.4885228	0.1492155	0.007937	7.0034684	0.000105	0.1902089	2.3045643	2.401848	12.574861	0.9676836	0.7880035	0.6871217	5.4785477
10	5.3562358	0.3949668	0.1067235	0.0032586	2.6101025	0.0181029	0.2414065	1.2522993	1.3615935	5.9512819	0.6411624	0.6904611	0.6190212	4.6025459
11	5.0702193	0.3974223	0.1011049	0.0059462	14.672748	0.0740588	0.2601002	2.8641076	3.0496208	22.009759	1.2396921	0.9908684	16.095883	5.2410162
12	11.685563	1.0312198	0.5301456	0.0030875	12.786268	0.0363352	0.4839702	2.8484108	2.9310787	28.423841	1.4419008	0.9887752	6.195607	4.9454277
13	3.9630078	0.2347184	0.0350606	0.0006909	12.082688	0.0001765	0.2946239	1.4265475	1.4851124	29.229405	1.353939	0.86967	2.5010596	4.2668237
14	1.9839848	0.1385861	0.0145541	0.0003186	2.2918037	0.0002307	0.1287599	0.363552	0.4119089	3.4584318	0.1593041	0.5987047	0.0882911	0.6907552
15	8.4541346	0.3108616	0.1331005	0.0073235	8.4996573	0.0195163	0.3068196	1.0355878	1.1277306	13.361635	0.7132587	0.3934426	0.1683103	7.4433693
16	4.5625201	0.2539615	0.059362	0.0018236	4.3491956	0.003449	0.1363993	1.3916331	1.4941316	4.8451708	0.5518791	0.7218412	0.2807768	5.4335857
17	8.3185751	0.3511088	0.1185673	0.0054708	6.9923224	0.0763716	0.4630709	2.5107484	2.6000322	21.262468	1.4471108	0.8825853	0.8540174	3.897304
18	7.7615226	0.4925338	0.1647012	0.0023662	19.863126	0.0136158	0.4406139	2.7698741	2.8186318	42.557766	1.6895716	0.6542308	5.578994	3.097097
19	2.3437806	0.1440733	0.0184919	0.0004104	0.2491366	0.0003086	0.1496564	0.2884068	0.3037168	4.3207089	0.1755207	0.2758588	0.5391704	1.7965324
20	7.0920139	0.7602774	0.3680835	0.013514	12.795434	0.0048322	0.2779207	2.4382487	2.4991231	28.274992	0.8992121	0.7160269	1.952098	3.2955053
21	5.5284151	0.2908796	0.0658959	0.0022991	3.1406818	0.0012207	0.2047154	1.1683255	1.2536305	4.3415023	0.6008871	0.5253005	0.7365445	3.6528655
22	1.3405557	0.0879712	0.0109074	0.0003127	5.9231654	0.0004024	0.2671126	0.8364802	0.8748572	12.550524	0.6290377	0.6598955	4.2494878	1.3905858
23	1.1962742	0.0794331	0.0055512	0.000105	2.3721168	0.0011901	0.1646511	0.8454777	0.9118162	11.166576	0.5749744	0.6454872	0.5066993	3.8278369
24	1.2257223	0.1021892	0.0068879	0.0001327	0.7113997	0.0018149	0.1763654	0.3389278	0.3780698	2.3906515	0.2434176	0.2667699	0.1396622	4.882566
25	5.8985617	0.474233	0.1680927	0.0044326	4.4925883	0.0187026	0.1922645	2.1299438	2.2057469	10.278249	0.690515	0.5699668	1.1524429	4.0423238
26	4.1366406	0.2287002	0.0353482	0.0009421	1.6030487	0.0030476	0.1539674	0.4913481	0.5438994	4.8785155	0.2879081	0.5670571	0.0946546	5.1488315
27	0.4448126	0.0403438	0.0021014	1.903E-05	0.4098614	0.0002309	0.0486319	0.0394419	0.0411188	3.1042729	0.1285733	0.0550468	0.2655892	0.4197371
28	8.4074495	0.7192987	0.3026284	0.0113595	2.9973522	0.0017039	0.1318624	0.9149353						

Subject No.	DM1	DM2	DM3	DM4	NDM1	NDM2	NDM3	NDM4	NDM5	NDM6	NDM7	NDM8	NDM9	NDM10
1	3.6481099	0.2686236	0.0869251	0.0038164	5.6401558	0.0158336	0.1751856	1.4610337	1.5668795	12.274577	0.5933435	0.6457639	0.2767665	3.5031072
2	1.995352	0.0985686	0.0073018	9.371E-05	3.2395766	0.0010731	0.1288787	1.3876088	1.457105	6.6946675	0.4428805	0.507605	0.1474245	0.4492871
3	4.7538138	0.4280282	0.1179171	0.0030354	3.3719302	0.0085517	0.1836926	1.4612248	1.6221163	8.693469	0.5955912	0.3655323	0.5079914	2.4591691
4	2.4061167	0.1535231	0.0232755	0.0006237	1.1101953	0.0015023	0.0984309	0.8993319	0.949689	11.55352	0.3267121	0.4034356	2.5097968	2.6135685
5	1.6492853	0.0927088	0.0070164	0.0002062	1.0743602	0.0006139	0.1667508	0.4947624	0.5232157	5.6671604	0.2556841	0.5121951	1.7286288	3.0605596
6	3.7389499	0.2525093	0.0481957	0.0012841	18.380865	0.0005123	0.2088347	1.4475366	1.5355829	38.065009	1.5459635	0.7630019	1.072361	4.3929907
7	1.6713062	0.1312723	0.0143782	0.0001907	15.458512	0.055163	0.1968656	1.7754999	1.8075078	30.464399	1.2405578	0.8029159	17.0434	1.342834
8	3.7227414	0.2326732	0.0522379	0.0017903	2.707333	0.0043225	0.1345134	0.6530604	0.7246289	6.5289523	0.3507576	0.4032827	1.5402792	3.9626845
9	8.6333598	0.7572732	0.3314037	0.0064479	6.4523981	0.0060258	0.1803499	2.1847	2.3704405	11.066737	0.756019	0.6613751	2.9471037	3.2593944
10	5.312951	0.3967227	0.0945718	0.0025471	2.9830799	0.0329042	0.1977411	2.3437711	2.3093814	14.785952	0.8451046	0.8739092	0.9584628	3.2885345
11	5.0626033	0.0406351	0.001498	1.189E-05	13.84147	0.2493738	0.2503295	2.9566053	2.9732255	37.1944	1.609252	0.8592911	6.1876749	5.6250645
12	20.609717	2.9363625	3.3470468	0.1381576	14.562312	0.0369786	0.3131555	2.5663574	2.6094448	18.294821	1.0495932	0.9528009	1.9280496	3.1464984
13	6.0287732	0.5636195	0.2369258	0.0062829	4.8271431	0.0217967	0.1734512	1.6739782	1.8112058	10.329443	0.8034725	0.8709982	5.7456049	6.9785979
14	4.6465187	0.2714623	0.0490823	0.0027528	0.7061565	0.0004912	0.2069488	0.8125115	0.8800299	2.6846138	0.2917828	0.4904845	2.9932485	4.7541143
15	7.9584834	0.6643968	0.3311054	0.0112685	9.6951032	0.019034	0.1766656	2.223743	2.2870764	19.489742	0.9756536	0.9157617	7.2141573	4.3820513
16	3.4090568	0.2176195	0.0377072	0.0009871	5.0280679	0.0021753	0.111567	1.5736683	1.7264938	14.605035	0.6270399	0.8359944	0.2808039	3.8960705
17	5.5951661	0.3551137	0.0829734	0.0043815	4.9092656	0.0119684	0.1810589	1.7134517	1.9087586	10.328553	0.6931782	0.5844896	1.4689155	2.7528957
18	5.3483788	0.2156685	0.0404503	0.0016303	3.3531019	0.0039133	0.2864012	1.6136581	1.6703078	7.4411078	0.7495812	0.1609721	2.8869082	7.6044545
19	4.678835	0.3093527	0.078867	0.0027239	2.9836689	0.0011591	0.1239531	1.0981316	1.2057976	11.285063	0.3452661	0.4014163	0.2230378	1.0608998
20	2.7755602	0.6030529	0.2163145	0.0056041	7.1429606	0.0123284	0.3129249	2.3533173	2.4839613	10.063289	1.0137729	0.9179749	9.7883947	3.1853394
21	7.1833145	0.388044	0.097652	0.0060427	16.412549	0.0719613	0.1924341	2.1310765	2.1274271	29.096698	1.2258504	0.9511677	2.5288243	5.2508516
22	2.4249312	0.2304959	0.0314632	0.0004732	2.3917133	0.0015395	0.138289	0.9875518	1.092777	5.2745198	0.3859346	0.5845314	7.2994558	1.8777443
23	3.3514803	0.2098693	0.0300741	0.0008763	1.9064059	0.0013885	0.107662	0.7737889	0.8780408	9.8175142	0.3157718	0.3899256	1.0462338	1.5904770
24	4.8518421	0.3818902	0.0881298	0.0028469	3.4121925	0.0198707	0.1932579	1.2572532	1.4191539	8.7717702	0.4731819	0.5234835	8.7725979	2.9853249
25	3.6424524	0.0458908	0.0009792	0.0000016	26.115619	0.1155409	0.2276586	2.2901549	2.291231	34.144094	2.9634336	0.6342813	5.971828	1.2350729
26	4.8930459	0.3667809	0.0920442	0.0049128	3.9336267	0.0057051	0.1502298	1.4598918	1.5616248	10.313807	0.5220832	0.6823314	0.9742374	6.5484314
27	0.7581224	0.0527103	0.0059329	0.0002023	0.7368304	0.0003221	0.0679973	0.2451722	0.2553534	2.275608	0.1586212	0.1478128	2.043649	0.7638648
28	4.1614663	0.1932607	0.0341261	0.0021158	2.3480793	0.0006842	0.159253	0.7893957	0.7874754	4.9175769	0.3416898	0.4735256	1.0462338	0.7374865
29	2.4680723	0.1395899	0.0155661	0.0002249	3.7531626	0.002343	0.1585046	0.7492474	0.7602149	31.483967	0.446201	0.1916915	0.5859905	2.8079105
30	5.9644488	0.563906	0.1559399	0.0048903	5.9112919	0.0097457	0.1335638	2.3968358	2.484266	14.531366	0.7680382	0.4233075	0.3369319	2.8921712

Figure 6.6: All measures for the left ML of subjects. DM 1-4 are the measures based on a deformation field and NDM1-10 are the measures that do not require estimation of a deformation field.

Subject No.	DM1	DM2	DM3	DM4	NDM1	NDM2	NDM3	NDM4	NDM5	NDM6	NDM7	NDM8	NDM9	NDM10
1	2.8930415	0.1705639	0.0314779	0.0009575	11.014375	0.0010097	0.1531737	1.237298	1.2705189	23.526893	0.8487487	0.5761589	9.9914817	1.6047249
2	3.0119553	0.0723786	0.010868	0.0002534	21.082818	0.060019	0.2777678	2.0281146	2.0959037	12.272812	0.7945691	0.6695921	0.3635815	8.6340272
3	2.4430762	0.1759377	0.0247932	0.0008498	2.5148998	0.0051158	0.1744249	0.7284663	0.7524621	4.2616171	0.6937334	0.2467067	1.2416894	3.3039171
4	2.85694	0.130644	0.018576	0.0005238	9.0075594	0.0080543	0.1889797	0.9784806	1.0130672	20.952566	0.7195206	0.5537127	5.0707725	2.6307795
5	3.0785742	0.198157	0.0215594	0.0006424	4.5768857	0.0133589	0.4104117	1.0220323	1.048994	5.415034	0.6566026	0.5094032	5.6856286	4.9786333
6	5.8925244	0.5663422	0.2571513	0.0080665	4.4530694	0.0133941	0.2180436	1.985717	2.0792326	11.121271	0.7216843	0.8001013	3.8587675	3.1509067
7	7.0937958	0.579317	0.2623212	0.0060263	8.4148432	0.0101476	0.1995147	2.093329	2.1803011	9.7036472	0.6339134	0.4137401	1.4552088	3.9768367
8	1.2825056	0.1103366	0.0104262	0.0002	1.3579334	5.7E-05	0.083851	0.3820582	0.3892328	5.6086593	0.2010721	0.2021949	0.5338428	4.7582148
9	5.289724	0.4457567	0.110678	0.0044511	12.580048	0.0367018	0.244619	2.2780902	2.3153798	14.963826	1.0416446	0.7973534	4.9112625	3.7407621
10	10.701913	0.7749527	0.3790577	0.0114286	8.6466949	0.0385485	0.2205933	2.1149459	2.2389387	14.111859	0.9116422	0.6201088	1.1453715	4.0976864
11	4.3643729	0.3579671	0.0915553	0.0043891	15.447003	0.0405595	0.1805885	2.7575831	2.9644794	21.185097	1.084343	0.8244171	2.0363585	6.0347838
12	15.271844	1.5391363	1.300898	0.0179648	14.297601	0.0573266	0.2461996	2.4445337	2.5716756	13.097068	0.7592796	0.8538326	0.4373177	5.706631
13	4.074869	0.3574677	0.0869955	0.0022069	3.3281424	0.0162538	0.2068468	1.3103865	1.3910483	6.7276924	0.6329133	0.8165096	0.3842302	0.8805549
14	3.5722931	0.1799931	0.0244758	0.0008296	2.0272418	0.0011689	0.2094016	0.9308526	0.9582575	3.1879363	0.4087845	0.6255987	0.4974948	2.7435834
15	7.7351901	0.7161243	0.4494342	0.0097217	8.5934015	0.0304164	0.2241642	1.8831922	2.0140536	15.684954	0.9259033	0.5164455	1.3938857	5.4357899
16	1.9760049	0.1743052	0.0205133	0.0006084	7.5307614	0.0120613	0.2066458	1.609249	1.6727283	11.221288	0.8910547	0.7577026	0.8831405	4.1768565
17	6.7167657	0.2942118	0.0626215	0.0043688	12.274505	0.3655637	0.3495094	2.9943388	3.0403904	24.26689	1.6496738	0.9825865	2.657554	3.4600667
18	3.7503871	0.2164426	0.0464665	0.0011	5.5464086	0.011526	0.3435644	1.5866231	1.6235806	14.578182	0.8320357	0.3963346	0.5993965	4.1729941
19	2.1046771	0.1344691	0.015368	0.0006793	5.5601526	0.0084478	0.1531182	0.7807634	0.8036173	10.550245	0.3855736	0.277425	0.5626954	4.3803712
20	8.6116366	0.8854668	0.4055976	0.0179009	12.869084	0.0167894	0.2777645	2.0382251	2.0968005	23.786302	1.0813293	0.7377461	6.7837552	3.5909708
21	4.4843888	0.2993315	0.0663112	0.0035471	7.8428803	0.0048077	0.1818278	1.7526063	1.8438541	14.830422	0.8999389	0.8827961	0.4246427	5.3564683
22	3.0437143	0.1719144	0.0272414	0.0011838	11.302211	0.016037	0.2444413	1.2440959	1.2818674	11.187963	0.8842575	0.8005817	10.103232	5.7278517
23	2.5709062	0.1588862	0.0187202	0.0004326	9.4311394	0.0213135	0.3177769	0.7139391	0.7246946	9.8846416	0.7327091	0.5128827	0.0900522	5.2554348
24	3.3600653	0.2230986	0.0427002	0.0010009	1.6963921	0.0009423	0.1125957	0.7641382	0.823657	5.3201751	0.4022937	0.5260836	6.2334809	3.8160749
25	3.9406602	0.3415629	0.1041145	0.0041175	10.849041	0.0043778	0.3115615	1.170738	1.2173232	10.082712	0.6432647	0.7824518	2.3989067	2.6589322
26	3.5148692	0.273165	0.0534739	0.0016634	1.4912671	0.0052735	0.1352464	0.7551568	0.813929	4.5080793	0.2188179	0.626625	3.0988249	2.6485557
27	0.4705691	0.0354433	0.0009298	1.29E-05	0.3005797	9.374E-05	0.0266628	0.083388	0.084677	3.6416642	0.1254083	0.0945511	0.1331186	3.9100388
28	3.6289223	0.2688898	0.0544733	0.0020714	6.1005602	0.0179864	0.1828022	1.3676895	1.4436445	10.931934	0.7876983	0.508		

Subject No.	DM1	DM2	DM3	DM4	NDM1	NDM2	NDM3	NDM4	NDM5	NDM6	NDM7	NDM8	NDM9	NDM10
1	11.327086	0.7061023	0.1603559	0.0060466	18.2631	0.0184195	0.585014	3.1988988	3.386153	40.813938	1.7237057	1.6349983	11.793253	9.9532199
2	8.6218405	0.4597188	0.0431084	0.0007406	28.553533	0.0635603	0.7470505	5.2419074	5.5904001	35.389678	1.9634106	2.2403409	0.9732298	13.580184
3	16.540222	1.3761756	0.3912681	0.0099966	15.804487	0.0366425	0.8852422	4.9299552	5.3624616	28.357338	2.6764509	1.5367352	4.0278921	8.382434
4	9.2671961	0.5378868	0.0655442	0.0017006	13.154126	0.0096668	0.4466712	2.8769244	3.0471186	41.462063	1.7450662	1.5770775	9.622298	12.354551
5	13.718222	0.6792955	0.1033024	0.0031194	23.680308	0.0251222	0.972327	4.3702977	4.5781333	36.701684	2.2831409	2.3301535	16.306594	18.075792
6	17.864017	1.4020444	0.4212259	0.0125306	26.700233	0.0205262	0.7315075	4.9225029	5.2648745	56.679828	3.0462902	2.600948	19.456886	15.388891
7	18.480609	1.5577296	0.5551911	0.0146918	32.610619	0.0697086	0.8530019	6.5031142	6.8375696	53.88821	2.9198052	1.8183263	18.770503	9.9553185
8	11.191229	0.6413112	0.119948	0.004933	6.0413315	0.0059638	0.4977534	1.5339448	1.6650085	17.562515	0.920815	1.0524549	2.7757616	11.65519
9	23.815377	2.1666897	0.7202824	0.0243004	30.794215	0.0445079	0.8505717	8.5329343	9.0271572	45.224506	3.4769591	2.9916081	10.714952	15.210238
10	25.666877	1.8754562	0.6293896	0.018042	16.647385	0.0966758	0.8839538	6.7177846	6.9679239	39.750537	2.920962	2.6666951	6.2871878	15.04109
11	17.12517	0.9611425	0.2115326	0.0108836	60.901481	0.3913947	0.8803618	11.188488	11.628119	122.03476	5.7093726	3.4869498	28.085699	22.926541
12	52.789551	5.965347	5.2857451	0.1643679	45.77492	0.1321641	1.3292452	9.5364697	9.7661086	68.438194	3.6433286	3.4555521	9.0228015	18.400623
13	20.564196	1.5454365	0.4706621	0.0146889	21.477252	0.0433331	0.9732976	5.3432882	5.6976397	53.113746	3.2283941	3.3059051	10.253907	17.467874
14	16.11138	0.8606646	0.1627288	0.0070823	5.7169562	0.00241	0.8044612	2.6647861	2.8742963	25.088064	1.0984788	2.3161554	3.8276362	9.7162939
15	27.846613	1.933807	0.9631151	0.0304996	35.706589	0.0854641	0.9040552	5.9038527	6.2434362	55.689358	3.3464488	2.2363983	8.9706324	24.376967
16	12.996636	0.8173436	0.1401279	0.004267	21.789996	0.0216751	0.6006356	6.0242248	6.471297	36.646454	2.8626224	3.1843313	1.5597946	17.626148
17	23.39811	1.2409638	0.3013484	0.015043	28.768307	0.461559	1.2207442	8.6820067	9.1409253	62.328213	4.346004	3.4943563	7.2216262	14.259901
18	22.375177	1.1620749	0.2863032	0.0052701	48.160869	0.0887823	1.420187	9.0264621	9.1837422	93.178472	5.0548903	2.2996947	8.3623535	20.49764
19	21.315074	0.9690629	0.3364308	0.0112735	11.438932	0.011116	0.5963305	2.7269764	2.9593377	29.844466	1.1613453	1.4230349	1.4732155	9.8143264
20	32.50527	3.0855776	1.3703375	0.0528348	39.824486	0.0612948	1.1845526	8.1977863	8.5442031	74.16714	3.7463392	3.0511236	20.472097	12.781494
21	22.231977	1.3850196	0.3500195	0.0150774	30.105067	0.0817291	0.7674144	6.0127326	6.2935177	53.92246	3.1712109	2.8404376	3.9917378	16.365467
22	9.6763014	0.5963479	0.0819591	0.0022553	20.066043	0.0180195	0.8199476	3.3233906	3.5346441	30.885815	2.0265031	2.4202945	21.980882	11.367315
23	10.196	0.5987329	0.078537	0.0023786	17.04398	0.026031	0.7305228	3.3926104	3.720256	36.008803	2.1926799	2.1571293	2.2311603	17.235615
24	12.09943	0.8084111	0.1510517	0.0044712	6.781593	0.023497	0.5774216	2.6779556	2.9866062	18.501347	1.3832326	1.6927155	8.7158578	17.219539
25	18.235707	1.1218611	0.3239396	0.0103261	46.065582	0.1592373	1.101658	6.4864658	6.6290812	60.066991	5.155631	2.2791741	9.6019319	10.6951
26	14.240137	1.0111733	0.1972139	0.0079073	8.3842767	0.0155831	0.5652699	3.1493597	3.4218583	23.000458	1.2767664	2.3779454	4.6339249	19.11659
27	2.1409385	0.1589622	0.0104869	0.0002549	1.995228	0.0006945	0.1776287	0.4413216	0.4606085	10.214271	0.5272886	0.3405141	2.7106767	5.6021394
28	21.334338	1.3526378	0.4288038	0.0177125	14.464808	0.0209353	0.6651294	3.833861	3.9832466	42.348166	2.526529	2.2269626	4.127536	11.4341
29	14.483251	0.8786468	0.1770214	0.0058581	8.1791672	0.0086696	0.6934991	2.7627878	2.9220195	47.012532	1.6094808	1.1116451	5.43619	15.771074
30	16.838346	1.5099167	0.3334745	0.0095087	18.917256	0.0610236	0.6235029	8.0223804	8.5167154	48.991126	3.0988981	1.7832177	2.9819668	17.515441

Figure 6.8: *The sum of the measures of all bundles. DM 1-4 are the measures based on a deformation field and NDM1-10 are the measures that do not require estimation of a deformation field.*

6.4.3 Statistical Tests

Tests of significance are performed to see whether a statistically meaningful relationship exists between the proposed measures and KPS, Zubrod scores and tumor grades. Since we do not have any parametric form assumptions on the probability densities of measures, non-parametric tests are used.

Since the number of subjects is low and the number of patients that got worse is only 1 for KPS and 3 for Zubrod, the dependent variables were reduced to binary categories. The neurological scores were separated into categories “patient got better” and “patient did not get better”. The tumor grades were grouped into 2 groups where grade 1-2 tumors make one group and grade 3-4 tumors make the other group. 3 of the subjects were removed from the statistical analysis because some of their tracts had significant problems with the tractography and fiber classification steps which could not be resolved even with manual intervention. Hence, statistical tests were performed on 27 subjects.

The Mann-Whitney U test (also known as Wilcoxon rank-sum test) [106] was performed for each of the 14 measures derived from the change in each of the four bundles (left CST, right CST, left ML, right ML) and their sum for KPS score, Zubrod score and tumor grade. Hence, in total, $14 \times 5 \times 3 = 210$ significance tests were performed. In the Mann-Whitney U test, the null hypothesis is that the two samples are drawn from the same population and the alternative hypothesis is that they are drawn from populations with different distributions. For example, the null hypothesis of one of the 210 tests will be that the sample of DM1 measures for CST left for which the patient showed improvement after the operation and the sample of DM1 measures for CST left for which the patient did not show improvement, are drawn from the same population. If there is enough evidence to reject the null hypothesis, that would mean that the probability distribution of DM1 measures for CST left is different for patients that got better and that did not get better. The p-values for all the tests are given in Figure 6.9.

	KPS	Zubrod	TumorGrade		KPS	Zubrod	TumorGrade
DM1	0.215932294	0.54190318	0.933857503	DM1	0.030818058	0.05392947	0.489185943
DM2	0.018596673	0.102126085	0.524596652	DM2	0.00242228	0.0067665	0.361285931
DM3	0.084946657	0.341349314	0.889986861	DM3	0.010845951	0.026407049	0.361285931
DM4	0.068799988	0.17964055	0.760894901	DM4	0.012451017	0.029902636	0.213173105
NDM1	0.068799988	0.25151283	0.028854464	NDM1	0.039173309	0.060298087	0.072149939
NDM2	0.024041439	0.213399254	0.091504527	NDM2	0.104029174	0.317166521	0.175244245
NDM3	0.008176926	0.124282874	0.306036451	NDM3	0.166666239	0.25151283	0.193527004
NDM4	0.002841734	0.010414995	0.038003915	NDM4	0.004528633	0.01571998	0.025039194
NDM5	0.00206022	0.009040133	0.038003915	NDM5	0.005266669	0.013733951	0.028854464
NDM6	0.012451017	0.038099036	0.081361129	NDM6	0.021166992	0.020462223	0.158282211
NDM7	0.009427504	0.102126085	0.016093751	NDM7	0.024041439	0.042868119	0.033159987
NDM8	0.004528633	0.001175052	0.638147245	NDM8	0.012451017	0.005020543	0.14259358
NDM9	0.789550875	0.195987681	0.489185943	NDM9	0.061726242	0.213399254	0.013812197
NDM10	0.48166366	0.195987681	0.889986861	NDM10	0.544131679	0.393153438	0.14259358

(a)

(b)

	KPS	Zubrod	TumorGrade		KPS	Zubrod	TumorGrade		KPS	Zubrod	TumorGrade
DM1	0.061726242	0.048132396	0.889986861	DM1	0.152280758	0.07490957	1	DM1	0.049378436	0.07490957	0.977930004
DM2	0.423315987	0.294135512	0.599152836	DM2	0.094100638	0.092292339	0.678169354	DM2	0.044026799	0.083233931	0.803378185
DM3	0.51240135	0.341349314	0.524596652	DM3	0.138860481	0.16432928	0.678169354	DM3	0.076526653	0.150022328	0.889986861
DM4	0.51240135	0.272253581	0.361285931	DM4	0.126370087	0.124282874	0.719120729	DM4	0.094100638	0.124282874	0.933857503
NDM1	0.024041439	0.07490957	0.561275836	NDM1	0.182050081	0.150022328	0.306036451	NDM1	0.034781948	0.07490957	0.114828316
NDM2	0.51240135	0.980535541	0.489185943	NDM2	0.152280758	0.048132396	0.846450597	NDM2	0.068799988	0.213399254	0.193527004
NDM3	0.039173309	0.16432928	0.489185943	NDM3	0.152280758	0.231900487	0.391119358	NDM3	0.018596673	0.11277615	0.158282211
NDM4	0.024041439	0.067277961	0.256697732	NDM4	0.024041439	0.004310358	0.599152836	NDM4	0.008176926	0.01571998	0.102640343
NDM5	0.014262983	0.038099036	0.213173105	NDM5	0.024041439	0.004310358	0.599152836	NDM5	0.010845951	0.020462223	0.102640343
NDM6	0.182050081	0.25151283	0.977930004	NDM6	0.344015943	0.11277615	0.889986861	NDM6	0.012451017	0.013733951	0.524596652
NDM7	0.021166992	0.092292339	0.455104305	NDM7	0.152280758	0.102126085	0.391119358	NDM7	0.006111694	0.029902636	0.063810845
NDM8	0.274904063	0.102126085	0.561275836	NDM8	0.012451017	0.005834903	0.719120729	NDM8	0.016303709	0.004310358	0.561275836
NDM9	0.610384514	0.642968368	0.422402092	NDM9	0.51240135	0.510067528	0.158282211	NDM9	0.865134745	0.78841259	0.102640343
NDM10	0.75244276	0.25151283	0.391119358	NDM10	0.610384514	0.678319412	0.846450597	NDM10	0.544131679	0.124282874	0.846450597

(c)

(d)

(e)

Figure 6.9: p -values for all significance tests. (a): Left CST; (b): Right CST; (c): Left ML; (d): Right ML; (e): Sum of all 4 bundles. p -values between $[0.10 \ 0.05]$ are highlighted in red and p -values less than 0.05 are highlighted in green.

6.4.4 Discussion

We have described several measures that quantify different characteristics of the structural change between pre-op and post-op images. NDM4 and NDM5 consistently achieved p -values below 0.10 for all bundles and their sum for both KPS and Zubrod scores. It is worthy of noting that both of these measures are based on local orientation differences. On the other hand, deformation measures and measures based on global properties gave inconsistent results. The inconsistency in deformation measures may be caused by problems with the fiber registration algorithm. Measures that are not sensitive to isometric deformations did not give significant results. Interestingly, while some of the measures gave significant results for tumor grades on CST, none of them gave significant results for

ML. It is unclear whether this means that tumor aggressiveness is related to the structural change in CST after an operation but not to the change in ML or whether this result is caused by other factors such as the tractography algorithm and limitations of DTI.

While significant relationships with some of the measures and the clinical scores or tumor grades have been found, some inconsistencies like the same measure being significant for left CST but not right CST indicate that caution must be exercised before drawing strong conclusions. There are several problems that may limit the validity of statistical tests. The tests make the assumption that the sampled values of measures are a random sample drawn from some population. This assumption may not be valid due to biases in the imaging or tractography methods or the human interaction which is usually necessary for pathological data. Further, due to the low number of available subjects (27), we had to use binary categories for the change in patients' conditions. It is especially hard to find data for which the subject gets worse after the surgery because neurosurgeons only approve surgeries with a high likelihood of improving the patient's condition. It is thus unknown whether the measures can differentiate between the patient getting better or worse. Another limitation of the dataset was that there was no classification of patient's symptoms with respect to their associated fiber bundle. For example, if the patient has trouble moving his right hand, it can be hypothesized that this is caused by damage to the left CST. However, the available clinical scores in this study, KPS and Zubrod scores, are both general assessments of the patient's neurological condition. This can lead to e.g. the following problem: Let us assume that the patient only had pathology on his left CST and it healed after the surgery. This would improve the patient's general condition and hence this patient would be in the "the patient got better" category for all the statistical tests. Hence, for tests involving bundles other than the left CST, we have a sample for which the bundle has little or no change but the patient's condition has improved. This may be the reason that the tests for the sum of all bundles have in general achieved lower p-values compared to tests with individual bundles.

One of the most serious problems in white matter analysis is the difficulty of assessing the accuracy of tractography, that is, how well the digital tracts represent the trajectories of real fibers. There are a large variety of possible sources of error like limitations of the

diffusion model, partial volume effects, motion artifacts, eddy current artifacts, low angular resolution, errors in the tractography algorithm, errors in the clustering/classification method and so on. In order to make a meaningful analysis, the variance caused by those effects should be minimized by following the same analysis protocol for all the data. One should be aware that the conclusions reached using a certain analysis protocol may be invalid for a different protocol.

Despite the discussed problems, the fact that statistical significance was found for many of the tests suggests that it might be possible to predict the change in a patient's condition by using measures derived from the change in tractography and fiber classification results. This is an important conclusion that supports the claim that tractography and fiber classification are useful tools for studying human white matter.

Chapter 7

Conclusion and Future Directions

Diffusion MRI, fiber tractography and fiber classification following tractography provide valuable information about white matter fibers *in vivo* and enable unique ways of their study and analysis. In this thesis, we have presented three novel methods that aim to automate the fiber classification step in order to reduce the human bias and error associated with manual classification and to relieve the experts of this tedious task which can take up to hours for a single patient.

The first proposed method combines ROI-based and similarity-based approaches to fiber classification. ROIs are used to impose loose anatomical constraints on the created fiber tracts which are then clustered according to a fiber distance-based similarity approach. The clusters are then classified by comparison to bundle models. This method was designed for DTI and fibers passing through the brainstem and includes certain heuristics based on that, however, the general framework can be applied to other bundles or diffusion models.

The second method has a similar structure to the first one but introduces a novel fiber representation called NRFOD that is based on the orientation distribution of fibers in the neighborhood of a fiber. Since a fiber is represented by fiber orientations in its neighborhood, this representation is translation-invariant and suitable for comparing fibers from different spaces in case of translation error in the image registration. The method is also more general compared to the first one and may be applied to any diffusion or fiber orientation model. It achieved better performance compared to several other automatic methods

on brainstem fibers on the dataset we used for for experiments. While experiments were only performed on brainstem fibers, the method can be applied to any fiber bundle in the brain.

The third method is a supervised classification method and fundamentally different from the first two. Whereas the first two methods first perform unsupervised clustering by using a fiber-to-fiber distance measure and then classify the clusters by comparison to a bundle model, the third method directly maps a single fiber to class probabilities. This has the advantage of not requiring computation of fiber-to-fiber distances and hence scales better as the number of tracts in the set increases. The downside is the requirement of a labeled training set of tracts. Since the training set of fibers must all be in the same space, the translation-invariant NRFOD representation proposed for the second method is utilized here as it offers robustness to registration errors. The offline training of the classifier can be longer compared to the other methods but on the online test phase, this method is much faster and is also generally more accurate than the second method on our experiments.

Finally, we presented a clinical application of fiber tractography and classification. Fiber bundles were created using tractography and classification methods based on DTI data taken before and after a brainstem tumor resection operation. The change in corresponding fiber bundles were quantified using various measures and statistically significant relationships were found between some of the proposed measures and the patient’s neurological functionality. This important result is another evidence that tractography and fiber classification are useful tools for studying human white matter.

Future directions include creating more varied and larger training and validation sets for fiber classification methods. More sophisticated classifier architectures should be investigated. The supervised classification approach still remains largely unexplored and our initial results show great potential. Considering the recent popularity of deep learning methods in the computer vision community, significant advances in supervised fiber classification can be expected in the near future. Based on the novel techniques presented in this thesis, undertaking the classification of all brain white matter fibers for extraction of major brain white matter pathways would be a natural extension inspired by this thesis.

After more reliable tractography and automatic classification methods are developed, clinical analyses similar to the one presented in Chapter 6 may facilitate different ways of diagnoses, assessment of success of surgical operations and treatment, prediction of the progression of a disease or post-operational monitoring of a patient's condition. Further, those methods may lead to a better scientific understanding of how the brain communicates and functions.

Bibliography

- [1] M. T. Banich and R. J. Compton, *Cognitive Neuroscience*. Cambridge University Press, 2018.
- [2] R. W. Brown, Y.-C. N. Cheng, E. M. Haacke, M. R. Thompson, and R. Venkatesan, *Magnetic Resonance Imaging: Physical Principles and Sequence Design*. Wiley-Blackwell, 2014.
- [3] S. Mori, *Introduction to Diffusion Tensor Imaging*. Elsevier, 2007.
- [4] L. J. O’Donnell and C. F. Westin, “Automatic tractography segmentation using a high-dimensional white matter atlas,” *IEEE Transactions on Medical Imaging*, vol. 26, no. 11, pp. 1562–1575, Nov 2007.
- [5] L. J. O’Donnell, W. Wells, A. J. Golby, and C.-F. Westin, “Unbiased groupwise registration of white matter tractography,” *Med Image Comput Comput Assist Interv*, vol. 15, no. 0 3, pp. 123–130, 2012.
- [6] D. Wassermann, L. Bloy, E. Kanterakis, R. Verma, and R. Deriche, “Unsupervised white matter fiber clustering and tract probability map generation: Applications of a gaussian process framework for white matter fibers,” *NeuroImage*, vol. 51, no. 1, pp. 228 – 241, 2010.
- [7] D. Ugurlu, Z. Firat, U. Türe, and G. Unal, “Neighborhood resolved fiber orientation distributions (nrfod) in automatic labeling of white matter fiber pathways,” *Medical Image Analysis*, vol. 46, pp. 130 – 145, 2018.

- [8] B. Stieltjes, W. E. Kaufmann, P. C. van Zijl, K. Fredericksen, G. D. Pearlson, M. Solaiyappan, and S. Mori, "Diffusion tensor imaging and axonal tracking in the human brainstem," *NeuroImage*, vol. 14, no. 3, pp. 723 – 735, 2001.
- [9] K. Oishi, A. Faria, P. van Zijl, and S. Mori, *MRI Atlas of Human White Matter*. Elsevier Science, 2010.
- [10] B. C. Flores, A. R. Whittemore, D. S. Samson, and S. L. Barnett, "The utility of preoperative diffusion tensor imaging in the surgical management of brainstem cavernous malformations," *Journal of Neurosurgery*, vol. 122, no. 3, pp. 653–662, 2015.
- [11] A. C. Guyton and J. E. Hall, *Textbook of Medical Physiology: With STUDENT CONSULT Online Access, 11e (Guyton Physiology)*. Saunders, 2005, p. 687.
- [12] P. Conn, *Neuroscience in medicine*. Totowa, NJ: Humana Press, 2008, pp. 256–257.
- [13] P. S. Bhuiyan, L. Rajgopal, and K. Shyamkishore, Eds., *Inderbir Singh's Textbook of Human Neuroanatomy: Fundamental and Clinical*, 9th ed. Jaypee Brothers Medical Pub, 10 2014.
- [14] D. S. Yang, J. H. Hong, W. M. Byun, S. Y. Kwak, S. H. Ahn, H. Lee, C. H. Hwang, and S. H. Jang, "Identification of the medial lemniscus in the human brain: combined study of functional MRI and diffusion tensor tractography," *Neurosci. Lett.*, vol. 459, no. 1, pp. 19–24, Jul 2009.
- [15] S. H. Jang, Y. H. Kwon, M. Y. Lee, D. Y. Lee, and J. H. Hong, "Termination differences in the primary sensorimotor cortex between the medial lemniscus and spinothalamic pathways in the human brain," *Neurosci. Lett.*, vol. 516, no. 1, pp. 50–53, May 2012.
- [16] S. H. Jang and J. P. Seo, "Differences of the medial lemniscus and spinothalamic tract according to the cortical termination areas: A diffusion tensor tractography study," *Somatosens Mot Res*, vol. 32, no. 2, pp. 67–71, 2015.

- [17] Y. Leitner, K. Travis, M. Ben-Shachar, K. Yeom, and H. Feldman, “Tract profiles of the cerebellar white matter pathways in children and adolescents,” *The Cerebellum*, pp. 1–11, 2015.
- [18] S. Wang, G. G. Fan, K. Xu, and C. Wang, “Altered microstructural connectivity of the superior and middle cerebellar peduncles are related to motor dysfunction in children with diffuse periventricular leucomalacia born preterm: A DTI tractography study,” *European Journal of Radiology*, vol. 83, no. 6, pp. 997 – 1004, 2014.
- [19] T. Naidich, *Duvernoy’s atlas of the human brain stem and cerebellum high-field MRI : surface anatomy, internal structure, vascularization and 3D sectional anatomy*. Wien New York: Springer, 2009.
- [20] M. Levitt, *Spin Dynamics: Basics of Nuclear Magnetic Resonance*. Wiley, 2008.
- [21] A. Einstein, “Investigations on the theory of the brownian movement,” *Ann. der Physik*, 1905.
- [22] E. O. Stejskal and J. E. Tanner, “Spin diffusion measurements: Spin echoes in the presence of a time-dependent field gradient,” *The Journal of Chemical Physics*, vol. 42, no. 1, pp. 288–292, 1965.
- [23] P. J. Basser, J. Mattiello, and D. LeBihan, “Mr diffusion tensor spectroscopy and imaging.” *Biophys J*, vol. 66, no. 1, pp. 259–267, Jan 1994.
- [24] B. Jeurissen, A. Leemans, J.-D. Tournier, D. K. Jones, and J. Sijbers, “Investigating the prevalence of complex fiber configurations in white matter tissue with diffusion magnetic resonance imaging,” *Human Brain Mapping*, vol. 34, no. 11, pp. 2747–2766, 2012.
- [25] P. T. Callaghan, C. D. Eccles, and Y. Xia, “Nmr microscopy of dynamic displacements: k-space and q-space imaging,” *Journal of Physics E: Scientific Instruments*, vol. 21, no. 8, p. 820, 1988.
- [26] D. S. Tuch, “Diffusion mri of complex tissue structure,” Ph.D. dissertation, Massachusetts Institute of Technology, 2002.

- [27] V. J. Wedeen, P. Hagmann, W.-Y. I. Tseng, T. G. Reese, and R. M. Weisskoff, “Mapping complex tissue architecture with diffusion spectrum magnetic resonance imaging,” *Magn. Reson. Med.*, vol. 54, pp. 1377–1386, 01 2005.
- [28] D. S. Tuch, T. G. Reese, M. R. Wiegell, N. Makris, J. W. Belliveau, and V. J. Wedeen, “High angular resolution diffusion imaging reveals intravoxel white matter fiber heterogeneity,” *Magn. Reson. Med.*, vol. 48, pp. 577–582, 01 2002.
- [29] E. Özarslan and T. H. Mareci, “Generalized diffusion tensor imaging and analytical relationships between diffusion tensor imaging and high angular resolution diffusion imaging,” *Magn. Reson. Med.*, vol. 50, pp. 955–965, 2003.
- [30] D. S. Tuch, “Q-ball imaging,” *Magn. Reson. Med.*, vol. 52, pp. 1358–1372, 01 2004.
- [31] F. C. Yeh, V. J. Wedeen, and W. Y. I. Tseng, “Generalized q -sampling imaging,” *IEEE Transactions on Medical Imaging*, vol. 29, no. 9, pp. 1626–1635, Sept 2010.
- [32] W. Zhan and Y. Yang, “How accurately can the diffusion profiles indicate multiple fiber orientations? a study on general fiber crossings in diffusion mri,” *Journal of Magnetic Resonance*, vol. 183, no. 2, pp. 193 – 202, 2006.
- [33] J.-D. Tournier, F. Calamante, D. G. Gadian, and A. Connelly, “Direct estimation of the fiber orientation density function from diffusion-weighted mri data using spherical deconvolution,” *NeuroImage*, vol. 23, no. 3, pp. 1176 – 1185, 2004.
- [34] J.-D. Tournier, F. Calamante, and A. Connelly, “Robust determination of the fibre orientation distribution in diffusion mri: Non-negativity constrained super-resolved spherical deconvolution,” *NeuroImage*, vol. 35, no. 4, pp. 1459 – 1472, 2007.
- [35] J. Cheng, R. Deriche, T. Jiang, D. Shen, and P.-T. Yap, “Non-negative spherical deconvolution (nnsd) for estimation of fiber orientation distribution function in single-/multi-shell diffusion mri,” *NeuroImage*, vol. 101, pp. 750 – 764, 2014.
- [36] P. Basser, S. Pajevic, C. Pierpaoli, J. Duda, and A. Aldroubi, “In vivo fiber tractography using DT-MRI data,” *Magn Reson Med.*, vol. 44(4), pp. 625–632, 2000.

- [37] S. Mori and P. van Zijl, “Fiber tracking: principles and strategies - a technical review,” *NMR Biomed.*, vol. 15, pp. 468–480, 2002.
- [38] M. Lazar, D. M. Weinstein, J. S. Tsuruda, K. M. Hasan, K. Arfanakis, M. E. Meyerand, B. Badie, H. A. Rowley, V. Haughton, A. Field, and A. L. Alexander, “White matter tractography using diffusion tensor deflection,” *Hum Brain Mapp*, vol. 18, no. 4, pp. 306–321, Apr 2003.
- [39] T. J-Donald, C. Fernando, and C. Alan, “Mrtrix: Diffusion tractography in crossing fiber regions,” *International Journal of Imaging Systems and Technology*, vol. 22, no. 1, pp. 53–66, 2012.
- [40] O. Friman, G. Farneback, and C. F. Westin, “A bayesian approach for stochastic white matter tractography,” *IEEE Transactions on Medical Imaging*, vol. 25, no. 8, pp. 965–978, Aug 2006.
- [41] T. Behrens, H. J. Berg, S. Jbabdi, M. Rushworth, and M. Woolrich, “Probabilistic diffusion tractography with multiple fibre orientations: What can we gain?” *NeuroImage*, vol. 34, no. 1, pp. 144 – 155, 2007.
- [42] M. Descoteaux, R. Deriche, T. R. Knosche, and A. Anwander, “Deterministic and probabilistic tractography based on complex fibre orientation distributions,” *IEEE Transactions on Medical Imaging*, vol. 28, no. 2, pp. 269–286, Feb 2009.
- [43] K. H. Maier-Hein, P. F. Neher, J.-C. Houde, M.-A. Côté, E. Garyfallidis, J. Zhong, M. Chamberland, F.-C. Yeh, Y.-C. Lin, Q. Ji, W. E. Reddick, J. O. Glass, D. Q. Chen, Y. Feng, C. Gao, Y. Wu, J. Ma, H. Renjie, Q. Li, C.-F. Westin, S. Deslauriers-Gauthier, J. O. O. González, M. Paquette, S. St-Jean, G. Girard, F. Rheault, J. Sidhu, C. M. W. Tax, F. Guo, H. Y. Mesri, S. Dávid, M. Froeling, A. M. Heemskerk, A. Leemans, A. Boré, B. Pinsard, C. Bedetti, M. Desrosiers, S. Brambati, J. Doyon, A. Sarica, R. Vasta, A. Cerasa, A. Quattrone, J. Yeatman, A. R. Khan, W. Hodges, S. Alexander, D. Romascano, M. Barakovic, A. Auría, O. Esteban, A. Lemkaddem, J.-P. Thiran, H. E. Cetingul, B. L. Odry, B. Mailhe, M. S.

- Nadar, F. Pizzagalli, G. Prasad, J. E. Villalon-Reina, J. Galvis, P. M. Thompson, F. D. S. Requejo, P. L. Laguna, L. M. Lacerda, R. Barrett, F. Dell’Acqua, M. Catani, L. Petit, E. Caruyer, A. Daducci, T. B. Dyrby, T. Holland-Letz, C. C. Hilgetag, B. Stieltjes, and M. Descoteaux, “The challenge of mapping the human connectome based on diffusion tractography,” *Nature Communications*, vol. 8, no. 1, p. 1349, 2017.
- [44] U. Ture, M. G. Yasargil, A. H. Friedman, and O. Al-Mefty, “Fiber dissection technique: lateral aspect of the brain,” *Neurosurgery*, vol. 47, no. 2, pp. 417–426, Aug 2000.
- [45] S. Mori, W. E. Kaufmann, C. Davatzikos, B. Stieltjes, L. Amodei, K. Fredericksen, G. D. Pearlson, E. R. Melhem, M. Solaiyappan, G. V. Raymond, H. W. Moser, and P. C. van Zijl, “Imaging cortical association tracts in the human brain using diffusion-tensor-based axonal tracking,” *Magnetic Resonance in Medicine*, vol. 47, no. 2, pp. 215–223, 2002.
- [46] M. Catani, R. J. Howard, S. Pajevic, and D. K. Jones, “Virtual in vivo interactive dissection of white matter fasciculi in the human brain,” *NeuroImage*, vol. 17, no. 1, pp. 77 – 94, 2002.
- [47] P. Hagmann, J.-P. Thiran, L. Jonasson, P. Vandergheynst, S. Clarke, P. Maeder, and R. Meuli, “Dti mapping of human brain connectivity: statistical fibre tracking and virtual dissection,” *NeuroImage*, vol. 19, no. 3, pp. 545 – 554, 2003.
- [48] C. Habas and E. A. Cabanis, “Anatomical parcellation of the brainstem and cerebellar white matter: a preliminary probabilistic tractography study at 3 t,” *Neuroradiology*, vol. 49, no. 10, pp. 849–863, Oct 2007.
- [49] S. Wakana, A. Caprihan, M. M. Panzenboeck, J. H. Fallon, M. Perry, R. L. Gollub, K. Hua, J. Zhang, H. Jiang, P. Dubey, A. Blitz, P. van Zijl, and S. Mori, “Reproducibility of quantitative tractography methods applied to cerebral white matter,” *NeuroImage*, vol. 36, no. 3, pp. 630 – 644, 2007.

- [50] C. Granziera, J. D. Schmahmann, N. Hadjikhani, H. Meyer, R. Meuli, V. Wedeen, and G. Krueger, “Diffusion spectrum imaging shows the structural basis of functional cerebellar circuits in the human cerebellum in vivo,” *PLOS ONE*, vol. 4, no. 4, pp. 1–6, 04 2009.
- [51] N. Buchmann, J. Gempt, M. Stoffel, A. Foerschler, B. Meyer, and F. Ringel, “Utility of diffusion tensor-imaged (dti) motor fiber tracking for the resection of intracranial tumors near the corticospinal tract,” *Acta Neurochirurgica*, vol. 153, no. 1, pp. 68–74, Jan 2011.
- [52] M. Jenabi, K. K. Peck, R. J. Young, N. Brennan, and A. I. Holodny, “Identification of the corticobulbar tracts of the tongue and face using deterministic and probabilistic dti fiber tracking in patients with brain tumor,” *AJNR Am J Neuroradiol*, vol. 36, no. 11, pp. 2036–2041, Nov 2015.
- [53] X. Yao, T. Yu, B. Liang, T. Xia, Q. Huang, and S. Zhuang, “Effect of increasing diffusion gradient direction number on diffusion tensor imaging fiber tracking in the human brain,” *Korean J Radiol*, vol. 16, no. 2, pp. 410–418, Feb 2015.
- [54] K. Oishi, K. Zilles, K. Amunts, A. Faria, H. Jiang, X. Li, K. Akhter, K. Hua, R. Woods, A. W. Toga, G. B. Pike, P. Rosa-Neto, A. Evans, J. Zhang, H. Huang, M. I. Miller, P. C. van Zijl, J. Mazziotta, and S. Mori, “Human brain white matter atlas: Identification and assignment of common anatomical structures in superficial white matter,” *NeuroImage*, vol. 43, no. 3, pp. 447 – 457, 2008.
- [55] W. Zhang, A. Olivi, S. J. Hertig, P. van Zijl, and S. Mori, “Automated fiber tracking of human brain white matter using diffusion tensor imaging,” *NeuroImage*, vol. 42, no. 2, pp. 771 – 777, 2008.
- [56] Y. Zhang, J. Zhang, K. Oishi, A. V. Faria, H. Jiang, X. Li, K. Akhter, P. Rosa-Neto, G. B. Pike, A. Evans, A. W. Toga, R. Woods, J. C. Mazziotta, M. I. Miller, P. C. van Zijl, and S. Mori, “Atlas-guided tract reconstruction for automated and comprehensive examination of the white matter anatomy,” *NeuroImage*, vol. 52, no. 4, pp. 1289 – 1301, 2010.

- [57] R. O. Suarez, O. Commowick, S. P. Prabhu, and S. K. Warfield, “Automated delineation of white matter fiber tracts with a multiple region-of-interest approach,” *NeuroImage*, vol. 59, no. 4, pp. 3690 – 3700, 2012.
- [58] G. Prasad, S. H. Joshi, N. Jahanshad, J. Villalon-Reina, I. Aganj, C. Lenglet, G. Sapiro, K. L. McMahon, G. I. de Zubicaray, N. G. Martin, M. J. Wright, A. W. Toga, and P. M. Thompson, “Automatic clustering and population analysis of white matter tracts using maximum density paths,” *NeuroImage*, vol. 97, pp. 284 – 295, 2014.
- [59] Q. Wang, P.-T. Yap, G. Wu, and D. Shen, “Application of neuroanatomical features to tractography clustering,” *Human Brain Mapping*, vol. 34, no. 9, pp. 2089–2102, 2013.
- [60] D. Wassermann, N. Makris, Y. Rathi, M. Shenton, R. Kikinis, M. Kubicki, and C.-F. Westin, “On describing human white matter anatomy: The white matter query language,” *Med Image Comput Comput Assist Interv*, vol. 16, no. 0 1, pp. 647–654, 2013.
- [61] Z. Ding, J. C. Gore, and A. W. Anderson, “Classification and quantification of neuronal fiber pathways using diffusion tensor mri,” *Magnetic Resonance in Medicine*, vol. 49, no. 4, pp. 716–721, 2003.
- [62] A. Brun, H.-J. Park, H. Knutsson, and C.-F. Westin, “Coloring of dt-mri fiber traces using laplacian eigenmaps,” in *Computer Aided Systems Theory - EUROCAST 2003*, R. Moreno-Díaz and F. Pichler, Eds. Berlin, Heidelberg: Springer Berlin Heidelberg, 2003, pp. 518–529.
- [63] I. Corouge, S. Gouttard, and G. Gerig, “Towards a shape model of white matter fiber bundles using diffusion tensor mri,” in *2004 2nd IEEE International Symposium on Biomedical Imaging: Nano to Macro (IEEE Cat No. 04EX821)*, April 2004, pp. 344–347 Vol. 1.

- [64] B. Moberts, A. Vilanova, and J. J. van Wijk, “Evaluation of fiber clustering methods for diffusion tensor imaging,” in *VIS 05. IEEE Visualization, 2005.*, Oct 2005, pp. 65–72.
- [65] L. J. O’Donnell, M. Kubicki, M. E. Shenton, M. H. Dreusicke, W. E. L. Grimson, and C. F. Westin, “A method for clustering white matter fiber tracts,” *AJNR Am J Neuroradiol*, vol. 27, no. 5, pp. 1032–1036, May 2006.
- [66] J. Shao, K. Hahn, Q. Yang, C. Bohm, A. Wohlschlager, N. Myers, and C. Plant, “Combining time series similarity with density-based clustering to identify fiber bundles in the human brain,” in *2010 IEEE International Conference on Data Mining Workshops*, Dec 2010, pp. 747–754.
- [67] C. Böhm, J. Feng, X. He, S. T. Mai, C. Plant, and J. Shao, “A novel similarity measure for fiber clustering using longest common subsequence,” in *Proceedings of the 2011 Workshop on Data Mining for Medicine and Healthcare*, ser. DMMH ’11. New York, NY, USA: ACM, 2011, pp. 1–9.
- [68] M. Liu, B. C. Vemuri, and R. Deriche, “Unsupervised automatic white matter fiber clustering using a gaussian mixture model,” in *2012 9th IEEE International Symposium on Biomedical Imaging (ISBI)*, May 2012, pp. 522–525.
- [69] V. Siless, K. Chang, B. Fischl, and A. Yendiki, “Anatomiccuts: Hierarchical clustering of tractography streamlines based on anatomical similarity,” *NeuroImage*, vol. 166, pp. 32 – 45, 2018.
- [70] M. Maddah, A. Mewes, S. Haker, W. Grimson, and S. Warfield, “Automated Atlas-Based Clustering of White Matter Fiber Tracts from DTMRI,” in *MICCAI LNCS 3749*, J. Duncan and G. Gerig, Eds. Springer, 2005, pp. 188–195.
- [71] M. Maddah, L. Zollei, W. E. L. Grimson, and W. M. Wells, “Modeling of anatomical information in clustering of white matter fiber trajectories using dirichlet distribution,” in *2008 IEEE Computer Society Conference on Computer Vision and Pattern Recognition Workshops*, June 2008, pp. 1–7.

- [72] E. Garyfallidis, M.-A. Côté, F. Rheault, J. Sidhu, J. Hau, L. Petit, D. Fortin, S. Cunnane, and M. Descoteaux, “Recognition of white matter bundles using local and global streamline-based registration and clustering,” *NeuroImage*, vol. 170, pp. 283 – 295, 2018.
- [73] E. Garyfallidis, M. Brett, M. M. Correia, G. B. Williams, and I. Nimmo-Smith, “Quickbundles, a method for tractography simplification,” *Front Neurosci*, vol. 6, p. 175, 2012.
- [74] Y. Xia, U. Turken, S. L. Whitfield-Gabrieli, and J. D. Gabrieli, “Knowledge-based classification of neuronal fibers in entire brain,” *Med Image Comput Comput Assist Interv*, vol. 8, no. Pt 1, pp. 205–212, 2005.
- [75] H. Li, Z. Xue, L. Guo, T. Liu, J. Hunter, and S. T. Wong, “A hybrid approach to automatic clustering of white matter fibers,” *NeuroImage*, vol. 49, no. 2, pp. 1249 – 1258, 2010.
- [76] P. Guevara, D. Duclap, C. Poupon, L. Marrakchi-Kacem, P. Fillard, D. L. Bihan, M. Leboyer, J. Houenou, and J.-F. Mangin, “Automatic fiber bundle segmentation in massive tractography datasets using a multi-subject bundle atlas,” *NeuroImage*, vol. 61, no. 4, pp. 1083 – 1099, 2012.
- [77] Y. Jin, Y. Shi, L. Zhan, B. A. Gutman, G. I. de Zubicaray, K. L. McMahon, M. J. Wright, A. W. Toga, and P. M. Thompson, “Automatic clustering of white matter fibers in brain diffusion mri with an application to genetics,” *NeuroImage*, vol. 100, pp. 75 – 90, 2014.
- [78] B. Tunç, W. A. Parker, M. Ingalhalikar, and R. Verma, “Automated tract extraction via atlas based adaptive clustering,” *NeuroImage*, vol. 102, pp. 596 – 607, 2014.
- [79] M. Heker, R. Amer, G. Alexandroni, and H. Greenspan, “Automated supervised segmentation of anatomical fiber tracts using an adaboost framework,” in *2016 IEEE International Conference on the Science of Electrical Engineering (ICSEE)*, 2016, pp. 1–5.

- [80] V. Gupta, S. I. Thomopoulos, F. M. Rashid, and P. M. Thompson, “Fibernet: An ensemble deep learning framework for clustering white matter fibers,” in *Medical Image Computing and Computer Assisted Intervention - MICCAI 2017*, M. Descoteaux, L. Maier-Hein, A. Franz, P. Jannin, D. L. Collins, and S. Duchesne, Eds. Cham: Springer International Publishing, 2017, pp. 548–555.
- [81] V. Gupta, S. I. Thomopoulos, C. K. Corbin, F. Rashid, and P. M. Thompson, “Fibernet 2.0: An automatic neural network based tool for clustering white matter fibers in the brain,” in *2018 IEEE 15th International Symposium on Biomedical Imaging (ISBI 2018)*, April 2018, pp. 708–711.
- [82] J. Wasserthal, P. F. Neher, and K. H. Maier-Hein, “Tractseg - fast and accurate white matter tract segmentation,” *CoRR*, vol. abs/1805.07103, 2018. [Online]. Available: <http://arxiv.org/abs/1805.07103>
- [83] J. Wasserthal, P. F. Neher, and K. H. Maier-Hein, “Tract orientation mapping for bundle-specific tractography,” *ArXiv e-prints*, Jun. 2018.
- [84] J. Mazziotta, A. Toga, A. Evans, P. Fox, J. Lancaster, K. Zilles, R. Woods, T. Paus, G. Simpson, B. Pike, C. Holmes, L. Collins, P. Thompson, D. MacDonald, M. Iacoboni, T. Schormann, K. Amunts, N. Palomero-Gallagher, S. Geyer, L. Parsons, K. Narr, N. Kabani, G. Le Goualher, D. Boomsma, T. Cannon, R. Kawashima, and B. Mazoyer, “A probabilistic atlas and reference system for the human brain: International consortium for brain mapping (icbm).” *Philos Trans R Soc Lond B Biol Sci*, vol. 356, no. 1412, pp. 1293–1322, Aug 2001.
- [85] J. Mazziotta, A. Toga, A. Evans, P. Fox, J. Lancaster, K. Zilles, R. Woods, T. Paus, G. Simpson, B. Pike, C. Holmes, L. Collins, P. Thompson, D. MacDonald, M. Iacoboni, T. Schormann, K. Amunts, N. Palomero-Gallagher, S. Geyer, L. Parsons, K. Narr, N. Kabani, G. Le Goualher, J. Feidler, K. Smith, D. Boomsma, H. H. Pol, T. Cannon, R. Kawashima, and B. Mazoyer, “A four-dimensional probabilistic atlas of the human brain,” *J Am Med Inform Assoc*, vol. 8, no. 5, pp. 401–430, Jan 2001.

- [86] M. Ankerst, M. M. Breunig, H.-P. Kriegel, and J. Sander, “Optics: Ordering points to identify the clustering structure,” *SIGMOD Rec.*, vol. 28, no. 2, pp. 49–60, Jun. 1999.
- [87] F.-C. Yeh and W.-Y. I. Tseng, “Sparse solution of fiber orientation distribution function by diffusion decomposition,” *PLOS ONE*, vol. 8, no. 10, pp. 1–12, 10 2013.
- [88] R. H. Hardin, N. J. A. Sloane, and W. D. Smith, “Spherical coverings,” <http://neilsloane.com/coverings/>, 2015, accessed: 2017-12-08.
- [89] O. Pele and M. Werman, “The quadratic-chi histogram distance family,” in *Computer Vision – ECCV 2010*, K. Daniilidis, P. Maragos, and N. Paragios, Eds. Berlin, Heidelberg: Springer Berlin Heidelberg, 2010, pp. 749–762.
- [90] E. Garyfallidis, O. Ocegueda, D. Wassermann, and M. Descoteaux, “Robust and efficient linear registration of white-matter fascicles in the space of streamlines,” *NeuroImage*, vol. 117, pp. 124 – 140, 2015.
- [91] W. J. Scheirer, A. de Rezende Rocha, A. Sapkota, and T. E. Boult, “Toward open set recognition,” *IEEE Transactions on Pattern Analysis and Machine Intelligence*, vol. 35, no. 7, pp. 1757–1772, 2013.
- [92] V. Gupta, S. I. Thomopoulos, C. K. Corbin, F. Rashid, and P. M. Thompson, “Fibernet 2.0: An automatic neural network based tool for clustering white matter fibers in the brain,” in *2018 IEEE 15th International Symposium on Biomedical Imaging (ISBI 2018)*, April 2018, pp. 708–711.
- [93] R. A. Guler, D. Ugurlu, Z. Fırat, U. Türe, and G. Unal, “Shape deformation measures for white matter fibers,” in *2016 24th Signal Processing and Communication Application Conference (SIU)*, May 2016, pp. 1277–1280.
- [94] A. Tagliasacchi, H. Zhang, and D. Cohen-Or, “Curve skeleton extraction from incomplete point cloud,” in *ACM Transactions on Graphics (TOG)*, vol. 28, no. 3. ACM, 2009, p. 71.

- [95] S. Belongie, J. Malik, and J. Puzicha, “Shape matching and object recognition using shape contexts,” *Pattern Analysis and Machine Intelligence, IEEE Transactions on*, vol. 24, no. 4, pp. 509–522, 2002.
- [96] M. Reuter, F.-E. Wolter, and N. Peinecke, “Laplace–beltrami spectra as shape-dna of surfaces and solids,” *Computer-Aided Design*, vol. 38, no. 4, pp. 342–366, 2006.
- [97] R. Guler, S. Tari, and G. Unal, “Screened poisson hyperfields for shape coding,” *SIAM Journal on Imaging Sciences*, vol. 7, no. 4, pp. 2558–2590, 2014.
- [98] H. Jégou, M. Douze, C. Schmid, and P. Pérez, “Aggregating local descriptors into a compact image representation,” in *IEEE Conference on Computer Vision & Pattern Recognition*, jun 2010, pp. 3304–3311.
- [99] N. Komodakis and G. Tziritas, “Approximate labeling via graph cuts based on linear programming,” *Pattern Analysis and Machine Intelligence, IEEE Transactions on*, vol. 29, no. 8, pp. 1436–1453, Aug 2007.
- [100] N. Komodakis, G. Tziritas, and N. Paragios, “Performance vs computational efficiency for optimizing single and dynamic mrfs: Setting the state of the art with primal-dual strategies,” *Comput. Vis. Image Underst.*, vol. 112, no. 1, pp. 14–29, Oct. 2008.
- [101] J. Lubliner, *Plasticity Theory (Dover Books on Engineering)*. Dover Publications, 2008.
- [102] A. Hamamci, “Image analysis methods for brain tumor treatment follow-up,” Ph.D. dissertation, Sabanci University, 2013.
- [103] D. A. Karnofsky and J. H. Burchenal, *Evaluation of chemotherapeutic agents*. New York: Columbia University Press, 1949, ch. The clinical evaluation of chemotherapeutic agents in cancer, p. 191–205.
- [104] M. M. Oken, R. H. Creech, D. C. Tormey, J. Horton, T. E. Davis, E. T. McFadden, and P. P. Carbone, “Toxicity and response criteria of the Eastern Cooperative Oncology Group,” *Am. J. Clin. Oncol.*, vol. 5, no. 6, pp. 649–655, Dec 1982.

- [105] D. N. Louis, A. Perry, G. Reifenberger, A. von Deimling, D. Figarella-Branger, W. K. Cavenee, H. Ohgaki, O. D. Wiestler, P. Kleihues, and D. W. Ellison, “The 2016 world health organization classification of tumors of the central nervous system: a summary,” *Acta Neuropathologica*, vol. 131, no. 6, pp. 803–820, 2016.
- [106] D. R. W. H. B. Mann, “On a test of whether one of two random variables is stochastically larger than the other,” *The Annals of Mathematical Statistics*, vol. 18, no. 1, pp. 50–60, 1947.